1-1-2016

Environmental and Growth Rate Effects on Trace Element Incorporation to Calcite and Aragonite: An Experimental Study

Jeremy M. Weremeichik

Environmental and growth rate effects on trace element incorporation to calcite and aragonite: An experimental study

By

Jeremy M. Weremeichik

A Dissertation
Submitted to the Faculty of
Mississippi State University
in Partial Fulfillment of the Requirements
for the Degree of Doctor of Philosophy
in Earth and Atmospheric Sciences
in the Department of Geosciences

Mississippi State, Mississippi

May 2016

Environmental and growth rate effects on trace element incorporation to calcite and aragonite: An experimental study

By

Jeremy M. Weremeichik

Approved:

_____
Rinat I. Gabitov
(Director of Dissertation)

_____
Adam Skarke
(Committee Member)

_____
Padmanava Dash
(Committee Member)

_____
Aleksey Sadekov
(Committee Member)

_____
Michael E. Brown
(Graduate Coordinator)

_____
Rick Travis
Interim Dean
College of Arts & Sciences

Name: Jeremy M. Weremeichik

Date of Degree: May 7, 2016

Institution: Mississippi State University

Major Field: Earth and Atmospheric Sciences

Director of Dissertation: Rinat I. Gabitov

Title of Study: Environmental and growth rate effects on trace element incorporation to calcite and aragonite: An experimental study

Pages in Study 112

Candidate for Degree of Doctor of Philosophy

The subsumed work of this dissertation is comprised of three independent but interrelated studies which seek to further the understanding of processes which govern the coprecipitation of trace elements with calcite and aragonite minerals. These studies investigate the effects of: 1) pressure on crystal morphology and trace element incorporation to aragonite; 2) growth rate on uranium partitioning between calcite and fluid; 3) aqueous Mg/Ca on the magnesium partitioning to low-magnesium calcite. The importance of this work is to determine how the environment of formation and growth rate influences the geochemistry of $CaCO_3$ in order to improve existing paleoproxies and develop new ones.

In the first study a series of experiments were conducted at 1, 25, 75, 100, and 345 bars of nitrogen – this range covers pressures at the oceanic floor. Aragonite precipitation was induced by the one-time addition of a Na_2CO_3 solution to an artificial seawater. Results suggest that oceanic floor pressures could affect the crystallization of $CaCO_3$ by altering mineralogical composition and aragonite crystal size.

In the second study calcite crystallized from NH_4Cl-$CaCl_2$-U solution by diffusion of CO_2. The calcite growth rate was monitored by sequential spiking of the calcite-precipitating fluids with REE dopants. The resulting crystals were analyzed using Secondary Ion Mass Spectrometry (SIMS). Results showed that the partitioning of uranium increases with increasing growth rate. Growth entrapment model (GEM) and unified uptake kinetics model (UUKM) explain the obtained data.

In the third study $CaCO_3$ precipitated in NaCl solution by continuous addition of $CaCl_2$, $MgCl_2$, and either Na_2CO_3 or $NaHCO_3$. The Mg/Ca of the fluid was adjusted in an attempt to produce calcite where Mg/Ca would match Mg/Ca in foraminifera shells. It was observed that multiple $CaCO_3$ polymorphs precipitated from fluids at high pH (Na_2CO_3 doping experiments). This result underscores the potential control of pH and/or supersaturation state on $CaCO_3$ polymorph precipitated from low Mg/Ca solutions. Calcite was the only mineral crystallized at low pH ($NaHCO_3$ doping experiments). It was determined that Mg partition coefficient between calcite and fluid (K^{Mg}) negatively correlates with $Mg/Ca_{(Fluid)}$ when it exceeds 0.5 mol/mol; no systematic correlation was observed when $0.05 < Mg/Ca_{(Fluid)} < 0.5$ mol/mol.

ACKNOWLEDGEMENTS

I would like to acknowledge and thank the following individuals and organizations for their contributions as this work would have never come to fruition without their support: Kristen Stives and my two Labradors for their love, support, and understanding throughout the duration of this project; Axel Schmitt, Kevin McKeegan, and Mark Harrison for their help and support with the ion microprobe measurements; Bruce Watson for providing the code used to model growth entrapment; experiments and SIMS analyses were supported by NSF, EAR, Instrumentation and Facilities Program. We are grateful to Walter Geibert, Mervyn Greaves, Sambuddha Misra, Harry Elderfield for support of elemental measurements at the University of Edinburgh and the University of Cambridge; Anita Leinweber for measuring DIC; these analyses were covered by ETH grant no. 4 443869-AL-20600; elemental measurements of the fluids were also covered by ERC grant NEWLOG 267931 to H. Elderfield; Neil Sturchio for sharing the LAS-20 calcite; Chiara Borrelli for conducting ICP-MS analysis and help with performing experiment at 345 bars; Ben Hartenbower and Dr. Todd French for troubleshooting/fabrication and use of the high-pressure vessel at MSU, respectively; Aleksandra Novak for preforming AAS analyses and Hadi Khani for training and assistance with AAS; Jared Singer for electron micro-probe analysis; Salavat Khasanov and Irina Zverkova from the Institute of Solid State Physics at the Russian Academy of Sciences for conducting powered X-ray diffraction of some of the samples from this

study; Brittany Garner for her instruction and assistance with alkalinity titrations; Mimi Katz, Karyn Rogers, Jay Thomas, the department staff, and all my colleagues, friends, and family.

TABLE OF CONTENTS

LIST OF TABLES

LIST OF FIGURES

CHAPTER I

INTRODUCTION

The intent of the work presented, is to expand upon the body of knowledge which exists for carbonate geochemistry. Each chapter of this dissertation will be formally introduced on an individual basis. However, this chapter serves as a general overview of the currently accepted facts, theories, and concepts – in the field of carbonate geochemistry and related disciplines – which are important to understanding the purpose of the laboratory experiments and theoretical modeling conducted as part of this project. The preceding chapters seek to evaluate the geochemical response of $CaCO_3$ (minerals which are common in marine and terrestrial settings) on growth processes and environmental influences. The final chapter will serve as a brief yet comprehensive summary of the main points of this dissertation and will highlight the importance of future researcb. A brief summary highlighting the purpose of the work conducted in the each of the preceding chapters can be found below.

The second chapter of this dissertation seeks to evaluate the effects of oceanic pressures on the partitioning of various trace and minor elements between aragonite and fluid. Many marine organisms/micro-organisms who build their shells, skeletons, or tests from calcium carbonate minerals (usually calcite and/or aragonite) live in deep water environments where hydrostatic pressure may exceed 100 bars. Examples of such organisms include, but are not limited to, deep sea corals, sponges, mollusks, and benthic

foraminifera. These and other calcifying marine organisms can be utilized as geochemical archives as they are capable of preserving chemical variations in seawater over long periods of time (on the scale of 10^5 to 10^7 years) in the geologic past (e.g. Beck et al. 1992; Gaetani and Cohen, 2006). Benthic foraminifera could be identified and separated from planktonic species in the oceanic sediments thus avoiding the contamination with surface water environmental signal. The interaction of oceanic floor with subsurface gaseous-aqueous fluids (e.g. methane and hydrothermal vents) are capable of altering the chemical composition of bottom seawater and porewaters and therefore, has a strong potential to be recorded by benthic calcifying organisms (e.g. Hill et al., 2004).

It has been suggested by Hanor (2003) that approximately 20% (by volume) of the sediments and sedimentary rocks which make up the earth's crust is actually porewater. This porewater is directly derived from fluids which infiltrates the subsurface where dissolved solids can be in-part derived from the dewatering of porewaters within sediments during the burial and lithification process (Garrels and Mackenzie, 1971). The amount of dissolved solids present in porewaters is dependent upon the differential movement of water and solutes by ionic and molecular diffusion (Garrels and Mackenzie, 1971). The concentration of total dissolve solids (TDS) in porewaters varies greatly with regards to different sedimentary units (Hanor, 2003). The knowledge on partition coefficients of multiple elements helps to evaluate the benthic environment and geological events affecting it in the past.

The goal of the project described in chapter two is to determine if a correction for pressure is needed to more accurately evaluate element to calcium ratio (X/Ca) in water

using partition coefficients and aragonite X/Ca. It was shown by Shen et al. (2001) that the distribution coefficient of Sr in benthic foraminiferal calcite can be influenced by hydrostatic pressure. A similar effect may also exist for other elements which incorporate other polymorphs of calcium carbonate (e.g. aragonite). In addition, partitioning of multivalence elements – which are potentially important in the determining the timing of oceanic oxygenation events and determining the susceptibility of calcareous marine organism to industrial contaminate plumes – were determined.

The third chapter of this dissertation seeks to evaluate the dependence of uranium partitioning on crystal growth rate of individual calcite crystals. The application of this knowledge is similar in scope to that which is addressed in chapter two. A brief overview of the application of uranium incorporation to calcite includes its utilization as a geochronological tool in U-series age dating (e.g. Lundberg and Ford, 1994; Ku et al., 1998). Additionally, the U/Ca ratio is being used to track geologic events, climatic variations, and the ocean uranium budget though preservation of its signature in calcite (e.g. Russell et al., 1994; Min et al., 1995; Dunk et al., 2002).

The fourth chapter seeks to determine the relationship between $Mg/Ca_{(Fluid)}$ and the Mg partition coefficient for the range of Mg/Ca values reported for planktonic foraminifera. In nature, planktonic foraminifera produce low-magnesium calcite with distinct Mg/Ca that is typically found to be within the range of ~1.6 to ~10.2 mmol/mol based on data from Nürnberg et al. (1996); Lea et al. (1999); Kısakürek et al. (2008); Dueñas-Bohórquez et al. (2011); Hönisch et al. (2013). This Mg/Ca_{foram} range does not correspond to Mg/Ca_{foram} expected for crystallization from high Mg/Ca seawater (~5200 mmol/mol). Therefore, calcites in the present study were precipitated from fluids of low

Mg/Ca (30-3400 mmol/mol) in order to cover Mg/Ca range observed in foraminifera. This Mg/Ca is different from other experimental works where fluid Mg/Ca varied from 500 to 20,000 mmol/mol (e.g. Mucci and Morse, 1983; Mavromatis et al., 2013).

Each chapter is focused on a specific topic which collectively sought to investigate the role of environment and growth rate on the geochemistry of $CaCO_3$ in order to develop new paleoproxies and improve existing paleoproxies. The topics associated with this work are: determining the effect which the Mg/Ca ratio in fluid has on the Mg partition coefficient (K^{Mg}) between synthetically precipitated low-magnesium calcite and solution; modeling of the natural formation of inorganic aragonite in a simulated oceanic environment via the replication of pressures, temperatures, and concentration of dissolved ions in an artificial seawater solution; and the effect of growth rate on uranium partitioning between calcite and fluid.

1.1 Calcium Carbonate Minerals and Element Partitioning

Since the carbonates produced in this study vary in their morphological and chemical characteristics, it is important to address what makes each of them unique. Two polymorphs of $CaCO_3$ – calcite and aragonite – are found in sediments as well as incorporated into the skeletal framework and structures of organisms and micro-organisms (Mackenzie, 2003). Aragonite has a rhombohedral unit cell whereas calcite has a hexagonal unit cell (Figure 1.1). In regards to types of calcium carbonate (e.g. calcite or aragonite), there is variability in magnesium. An example of this variability can be observed in calcite where low-Mg calcite is defined as containing less than approximately 4 mol % $MgCO_3$, and calcites which contain >4 to ≤50 mole % $MgCO_3$ are defined as high-Mg calcite (Tucker and Wright, 1990; Mackenzie, 2003; Morse et al.,

2007). In contrast, Mg incorporation into aragonite is not as extensive as incorporation into calcite (e.g. Burton and Walter, 1987). In response to changing ocean chemistry, the abundance of Ca^{2+} and Mg^{2+} ions and Mg/Ca ratio fluctuates and leads to variation of the predominant polymorph of $CaCO_3$, which is precipitated by marine biota (e.g. foraminifera, calcareous algae, sponges, bryozoans, mollusks, ect.) (Stanley and Hardie, 1999). Inorganic experiments confirmed the observed effect of fluid Mg/Ca on mineralogy of calcium carbonate. Data of Morse et al. (1997) showed that elevated Mg/Ca (up to 5 mol/mol) and T°C (up to ~35 °C) favor aragonite precipitation.

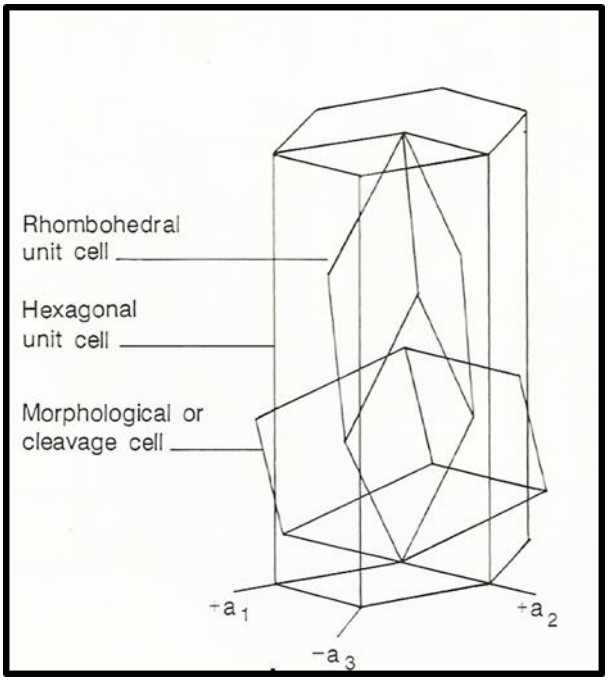

Figure 1.1 Rhombohedral unit cell of aragonite, hexagonal unit cell of calcite in addition to the morphological Iceland spar cleavage cell

From Tucker and Wright (1990).

Recent work indicates the importance of examining certain trace and minor elements which can be incorporated into the crystal lattice of calcium carbonate minerals

as they are becoming more useful as proxies for interpreting paleoenvironment conditions (e.g. Gaetani and Cohen, 2006; Fairchild and Treble, 2009; Raitzsch et al., 2011). Examples of the application of specific paleoproxies include: Li/Mg in aragonitic corals as a temperature proxy (Montagna et al., 2014); Mg/Ca in foraminifera as a temperature proxy (e.g. Nürnberg et al., 1996; Elderfield and Ganssen, 2000; Anand et al., 2003); Sr/Ca in biogenic aragonite as a temperature proxy (e.g. Gaetani and Cohen, 2006); Ba/Ca as a proxy for alkalinity (McManus et al., 1999; Rubin et al., 2003), and in corals as a temperature proxy (Allison and Finch, 2007), and to determine seawater composition (Lea and Boyle, 1991; Lea and Spero, 1992; Lea and Spero, 1994); Li/Ca in corals as a temperature proxy and potentially a salinity proxy (Marriot et al., 2004a; Marriot et al., 2004b); Mn/Ca and Fe/Ca abundances in foraminiferal tests could be used as a proxy for determining oxygen depletion (Glock et al., 2012); and Zn/Ca in benthic foraminifera has been shown to correlate with CO_3^{2-} in the overlying water column (Marchitto et al., 2000; Marchitto et al., 2002).

The extent of uptake has been shown to be influenced by environmental conditions such as temperature (e.g. Huang and Fairchild, 2001), salinity (e.g. Hönisch et al., 2013), pH (e.g. Hartly and Mucci, 1996), and biological activity (e.g. Lea et al., 1999). It is because the uptake of various trace elementals can be influenced by changes in environmental conditions that marine carbonates have the potential to preserve information pertaining to paleoenvironment conditions. The main problem of geochemical paleoproxies is that multiple parameters can affect geochemistry of $CaCO_3$ and it is hard or impossible to separate them without accurate values of partition coefficients determined in a laboratory setting where variables can be controlled.

Elemental abundancies in calcium carbonates can be determined through the use of analytical tools such as atomic adsorption spectroscopy, electron microprobe, and different mass spectrometry techniques. The information obtained using such instruments can then be used to determine element partitioning between fluids (e.g. seawater) and calcium carbonate minerals.

CHAPTER II

GEOCHEMICAL RESPONSE OF ARAGONITE UNDER THE INFLUENCE OF SUBAQUEOUS PRESSURES

2.1 Abstract

The intent of this work is to model the natural formation of inorganic calcium carbonate (e.g. aragonite) in a simulated oceanic environment via the replication of pressures and temperatures in an artificial seawater solution. The goals of this study are to better understand the effects of pressure at different temperatures on crystal morphology, crystal size, and the incorporation of minor and trace elements with aragonite. In order to achieve these goals, several laboratory experiments were conducted by the one-time addition of Na_2CO_3 to artificial sea water. Once ready, the experimental solutions were immediately placed in stainless-steel pressure vessels connected to a high-purity N_2 tank. We tested pressures from 25 to 345 bars. We also conducted experiments at low pressure (1 atm). In this case, the experiments were placed in either a refrigerated water-bath to control the temperature at 7.8 °C or conducted at room temperature (22 °C). Throughout the duration of the experiments, fluid sub-samples were collected at regular intervals to monitor pH. At the end of each experiment, we collected the crystals precipitated under our experimental conditions. Raman spectroscopy and X-ray diffraction confirms that the precipitated carbonate phase is aragonite in experiments conducted at high pressure (100, 345 bars) and low temperature (7.8 °C). Optical

microscopy analysis of the experimental crystals suggests that the addition of Na_2CO_3 leads to the nucleation of spherulites (hemispherical bundles of crystalline needles).

2.2 Introduction

Paleoenvironment studies commonly utilize calcareous producing organisms which incorporate different elements into their crystalline structure in varying abundancies. The level of enrichment of such elements (e.g. strontium, magnesium, uranium, barium, lithium, etc.) that are incorporated into the aragonite crystal lattice is linked to varying oceanic environmental factors. For example, Sr^{2+}, Ba^{2+}, and Mg^{2+} incorporation into aragonite has been demonstrated to be dependent upon temperature (Bath et al., 2000; Dietzel et al., 2004; Martin et al., 2004; Gaetani and Cohen, 2006; Gabitov et al., 2008). However, the effect of pressure on elemental incorporation had previously not been investigated, and therefore, this study is focused on evaluating the effect of pressure on the geochemistry of inorganically precipitated aragonite.

Limited studies have focused on evaluation of pressure effect on the growth of calcium carbonate (i.e. control over the precipitated crystal morphology) (references herein). There are even fewer studies which focus specifically on aragonite (e.g. Elderfield et al., 1996). The effect of pressure on the geochemistry of foraminiferal $CaCO_3$ are restricted to a few species of calcitic (e.g. *C. wuellerstorfi* and *Uvigerina* spp.) and aragonitic (e.g. *Hoeglundina elegans*) benthic foraminifera, where Sr/Ca and Mg/Ca decrease with increasing water depth and increasing pressure (Elderfield et al., 1996; Rosenthal et al., 1997; Shen et al., 2001). Pressure effect on carbonate geochemistry is unlikely direct at conditions similar to those found on the ocean floor. Mineral dissolution/precipitation rate (Dong et al., 2016), chemical speciation in the fluid (e.g.

Zeebe and Wolf-Gladrow, 2001; Zeebe, 2011), and metabolism of foraminifera could be affected by pressure and would likely control the carbonate geochemistry (e.g. Turley et al., 1993).

The primary purpose of the studies derived from literature was to create a new method, which would be an improvement over the established industrial carbonation process, for the production of calcite crystals with morphological control. The section which follows provides a condensed summary of the available literature – pertaining to laboratory experiments and biotic samples – which investigate the precipitation of calcium carbonate at low temperatures (i.e. ≥0 °C and ≤ 100 °C) and pressures which exist in the oceanic realm.

The current study consists of several experiments which were conducted at various oceanic pressures and temperatures of either 7.8 °C or 22 °C. Those experiments which were performed at atmospheric pressure are referred to as low-pressure (LP) whereas those which were performed at pressures ranging from 25 to 345 bar are referred to as high-pressure (HP). These experiments were conducted in order to understand the effects of pressure on the incorporation of minor elements to aragonite and the nucleation of aragonite under simulated oceanic conditions.

2.2.1 Background

The works on $CaCO_3$ crystallization at high pressure are restricted to a few studies, with scopes far from the present study. Domingo et al. (2004) investigated the controls which govern the synthetic precipitation of certain crystal morphologies of calcite using the $Ca(OH)_2$–H_2O–CO_2 system whereby $Ca(OH)_2$ was compressed using atmospheric, gaseous, liquid, and supercritical CO_2. The four experiments described in

the paper were carried out under pressures of either 1, 50, or 200 bar and temperatures of either 25 or 45 °C (Domingo et al., 2004, 2005). The findings of this work showed promise for alternate, more efficient and economic, means to mass produce rhombohedral calcite with a low degree of agglomeration for industrial manufacturing purposes (Domingo et al., 2004, 2005). Another paper, Montes-Hernandez et al. (2007), describes a series of experiments, conducted using the same method as Domingo et al. (2004) but does so under different experimental conditions (i.e. temperature and pressure). The experimental conditions reported in Montes-Hernandez et al. (2007) were 90 bar at 90 °C and 55 bar at 30 °C. The findings of this work suggest that the carbonation of calcium hydroxide in the presence of supercritical of gaseous CO_2 could be a technique utilized for the production of fine calcite particles at an industrial scale (Montes-Hernandez et al., 2007). Ibrahim et al. (2012) sought to improve on the methods of Domingo et al. (2004), through the addition of Solid Ionic Liquids (SILs). SILs were used in Ibrahim et al. (2012) to increase the reaction rate and provide morphological control of calcite produced using supercritical CO_2 and adjusting the ratio between dissolved Ca^{2+} and produced CO_3^{2-} species to stoichiometric conditions (i.e. $\frac{Ca^{2+}}{CO_3^{2-}} = 1$). The finding of this work suggest that coupling solid ionic liquid with CO_2 could be an effective way for enhancing traditional gas-solid reactions. It is important to note that the temperatures reported for abovementioned studies are all initial temperature readings and not a temperature sustained throughout the entirety of the experiment. The cause for variability of temperature in the experiments carried out in the four aforementioned studies is due to an exothermic reaction which occurs in response to the carbonation process. According to

Montes-Hernandez et al. (2007), the exothermic reaction takes place as result of simultaneous $Ca(OH)_2$ dissolution

$$Ca(OH)_{2(S)} \xrightarrow{water} Ca^{2+} + 2(OH)^{-} \quad (2.1)$$

and the dissociation of aqueous CO_2,

$$CO_{2(aq)} + H_2O \rightarrow HCO_3^{-} + H^{+} \quad (2.2)$$

There have also been a few works which have noted the effect of pressure on the geochemistry of foraminiferal $CaCO_3$ (e.g. Elderfield et al., 1996; Rosenthal et al., 1997; Shen et al., 2001). Elderfield et al. (1996) reported a strong depth relationship for Sr/Ca, in foraminiferal calcite and aragonite which shows Sr/Ca decreases with increasing depth. Rosenthal et al. (1997) found that Mg/Ca ratios in calcitic species of foraminifera decreases by a factor of 3–4 with increasing calcification depth, demonstrating a strong covariance with water temperature (i.e. the relationship of temperature decreasing with increasing depth causes Mg/Ca ratios to decrease). Shen et al. (2001) confirmed the results of Elderfield et al. (1996) and was able to demonstrate that at water depths greater than 1500 m, Sr/Ca in foraminifera decreases at a rate of 0.75% per 100 m. Foraminiferal tests were collected from core tops, box cores, gravity cores or by scuba divers at known depths, the tests were then cleaned and analyzed for trace/minor element concentrations using mass spectrometry and atomic absorption spectroscopy (Elderfield et al. 1996; Rosenthal et al. 1997; Shen et al.2001) . The works described above assisted in development of the current study by demonstrating a need for additional research to investigate the geochemical response of aragonite to pressure.

2.3 Materials and Methods

2.3.1 Experimental Design

A series of experiments were conducted using a high-pressure vessel at various pressures (25, 75, 100, 345 bars) and temperatures (7.8 and 22 °C) (see Table 2.1). The experimental set-up of those experiments can be seen in Figure 2.1. A related series of experiments were conducted at low pressure (1 atm.) in polypropylene containers (see Table 2.1). In this case, the experiments were either placed in a refrigerated water-bath to control the temperature at 7.8 °C or carried out at room temperature (22 °C). The experimental set-up of the low-pressure experiments is shown in Figure 2.2. The chemical concentration of the solutions used in our experiments is similar to those reported in Pytkowicz (1965). The concentrations of the solutions used in each experiment have been summarized in Table 2.2.

Table 2.1 Parameters of HP and LP experiments

Experiment	$pH_{Initial}$	Sub-sample $pH_{Initial}$	pH_{Final}	Pressure (bar)	Duration (hours)	Temperature (°C)
LP-02'	8.26	10.05	8.68	1	268	7.8
LP-03'	9.7	8.31	7.69	1	191	22
HP-01	10	9.24	7.79	100	111	22
HP-02	9.99	8.73	8.36	100	184	22
HP-25	9.81	9.67	6.94	25	158	22
HP-75	9.7	8.31	7.69	75	175	22
HP-RPI-2	9.59	9.25	8.64	345	281	7.8

All HP experiments were pressurized using high purity N_2 gas.

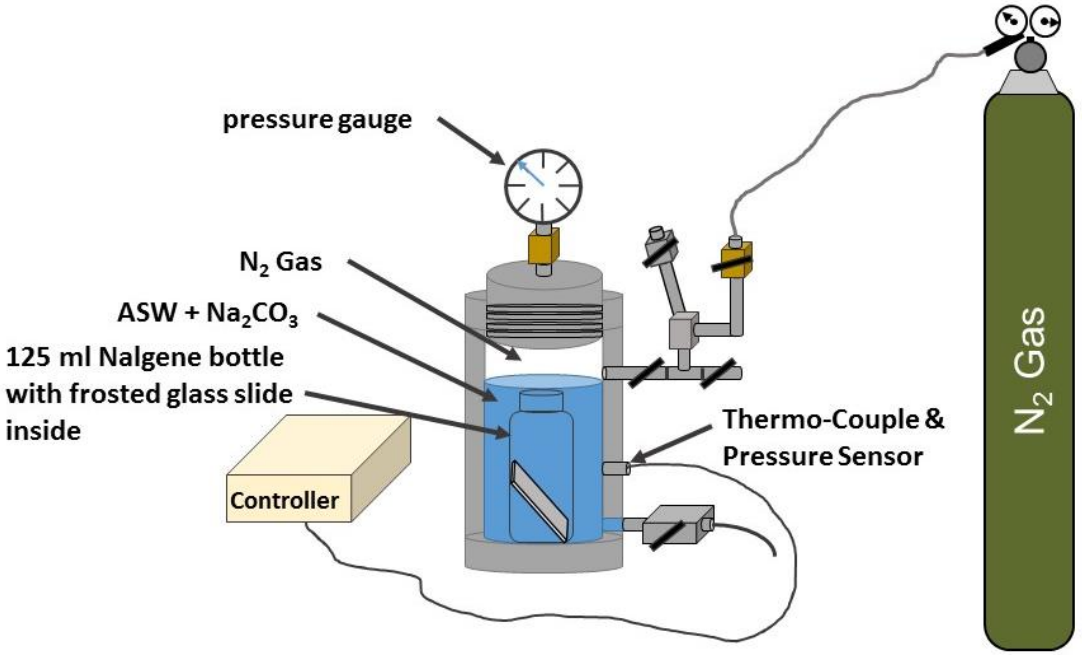

Figure 2.1 Experimental design for high-pressure experiments.

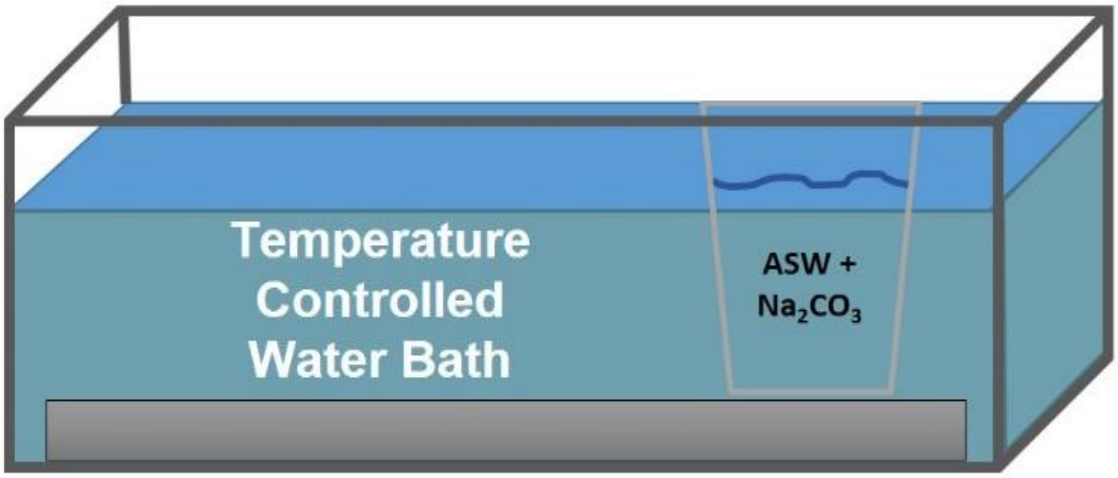

Figure 2.2 Experimental design for low-pressure experiments.

Table 2.2 Concentrations of solutions and additives

Experiment	ASW concentration synthetic sea salt : RO H_2O (g/L)	Prepared volume of ASW (ml)	Concentration of $NaH_2PO_4 \cdot H_2O$ (g/L)	Volume of 0.1 M Na_2CO_3 added to ASW (ml)	Final fluid volume (ml)
LP-02'	31.586	300	3.86E-04	24	244
LP-03'	31.586	300	3.86E-04	24	260
HP-01	31.586	300	3.86E-04	24	165
HP-02	31.586	300	3.86E-04	24	110
HP-25 bar	30	300	—	24	174
HP-75 bar	30	300	—	24	170
HP-RPI-2	31.586	835	—	67	750

Note that the reason for the prepared fluid volume being greater than the final fluid volume is that the pressure vessels could not hold the total prepared volume and that sub-samples were collected throughout the duration of some experiments.

A commercially available synthetic sea salt, Instant Ocean, was used for all experiments associated with the work described in this chapter. Artificial seawater (ASW) was prepared by mixing the synthetic sea salt with reverse osmosis (RO) H_2O. The concentration of ASW used in the experiments was either 31.586 g synthetic sea salt in 1 liter (L) of RO H_2O or 30 g synthetic sea salt in 1 L of RO H_2O. A one-time addition of Na_2CO_3 or $NaHCO_3$ to the ASW was conducted upon completion of preparation, this was done for all experiments (i.e. HP and LP). The solutions were mixed by pumping a 0.1M Na_2CO_3 solution into the ASW using a peristaltic pump. The proportion of Na_2CO_3 solution and ASW (25:1) was maintained near-constant in all experiments. Experiments HP-02, LP-02′, and LP-03′ were stirred at 300 RPM during pumping using a magnetic stir bar and stir plate to mix the solutions in an attempt to preclude precipitation. Once mixed, the solution was then either placed into the pressure vessel or into a polyethylene container, depending on the nature of the experiment. Upon visual inspection no

precipitates were observed in the solution. Pytkowicz (1965) demonstrated that the passage of a few hours is needed prior to the onset of aragonite crystallization using similar proportions of Na_2CO_3 and ASW. For HP experiments, a frosted glass slide was placed inside a 125 ml Nalgene bottle. The bottle had a hole in the bottom and the side in order to allow for circulation of the solution during sub-sampling. Once the bottle containing the glass slide was added to the pressure vessel, the solution was then added and the lid tightened down on the vessel. High purity nitrogen gas was then bubbled through the solution and out of the pressure vessel to remove as much free O_2 as possible from within vessel and from the solution. Finally, all release valves were closed and the N_2 pressure was adjusted to the desired level. Some experiments were doped with trace amounts of $NaH_2PO_4 \cdot H_2O$ (see Table 2.2) in order to elevate the phosphate concentration of the ASW which would in-turn promote growth of individual crystals by inhibiting nucleation (Mucci and Morse, 1983; Burton and Walter, 1990; Plant and House, 2002).

Sub-samples from certain experiments (i.e. HP-01, HP-02, HP-RPI-2, LP-02', and LP-03') were collected, measured for pH, and preserved for further salinity and chemical analyses. The design of the apparatus used in the HP experiments did not allow the author to monitor changes in pH *in-situ* (see Figure 2.3). The HP-RPI-2 experiment was conducted at Rensselaer Polytechnic Institute (RPI) by Rinat Gabitov and Chiara Borrelli using equipment and lab space provided by Bruce Watson, Mimi Katz, Karyn Rogers, and Jay Thomas. All pH measurements were conducted using a Denver Instrument UB-10 UltraBASIC benchtop meter equipped with a Sartorius PY-P11 pH Combination Electrode. Sub-samples and final fluids from experiments were initially preserved by

freezing of the fluid at -20 °C in Nalgene bottles. Later, small volumes were acidified using 2% trace metal grade HNO_3. This procedure was necessary to prevent post-experimental $CaCO_3$ crystallization prior chemical analyses with ICP-MS.

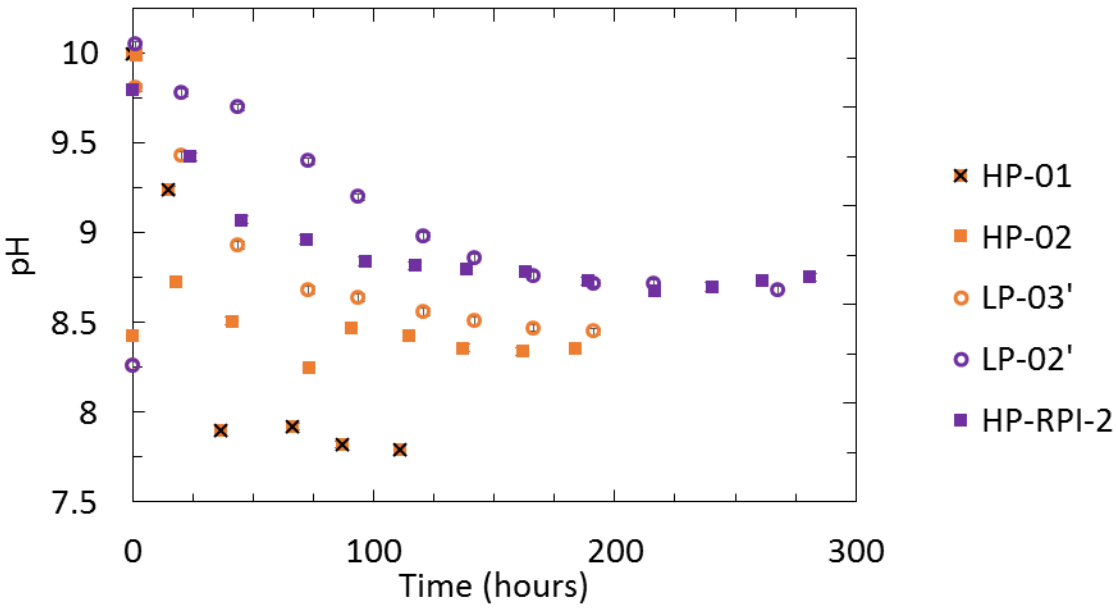

Figure 2.3 Graphical representation of pH evolution over the duration of experiments where fluids were sub-sampled.

Open circles indicate that the experiment was conducted at 1 atmosphere of pressure and closed shapes indicate the experiment was conducted at elevated pressure. Symbols colored orange indicate the experiment was conducted at 22 °C while symbols colored purple indicate the experiments was conducted at 7.8 °C. Analytical uncertainty is ± 0.02 and is included in symbol size.

2.4 Procedure for Cleaning Pressure Vessel

Between subsequent experiments, preformed using the high-pressure vessel, the vessel was cleaned by one of two methods. Using the first method, the vessel was filled with water and pressurized with CO_2 for approximately 24 hours. After 24 hours, pressure was released, water was drained from the vessel, and the inside of the pressure vessel was wiped out using laboratory paper towels. This method was used to clean the

vessel at the end of experiments HP-01 and HP-02. The second method was conducted by pressurizing highly diluted (2.5 to 0.8% by volume) acetic acid with N_2 gas in the vessel for 12 to 24 hours. The pressure was then released allowing the fluid to drain from the vessel. Finally, the vessel was filled with RO H_2O, then pressurized and drained again to remove any residual acid. The second method described was used to clean the pressure vessel prior to the beginning of experiments HP-75 bar and HP-25 bar.

2.5 Analytical Techniques

2.5.1 ICP-MS

2.5.1.1 Container Preparation

Solid and fluid samples from all HP and LP experiments, conducted as part of this work, were sent to the University of Rochester, New York for Inductively Coupled Plasma–Mass Spectrometry (ICP-MS) analysis using a Thermo Electron X7 ICP-MS. Samples were sent in 15 ml polypropylene centrifuge tubes which were cleaned by the following means: 1) rinsing three times with 2-3 ml of 10% ACS grade HNO_3, 2) rinsing three times with 2-3 ml of 2% trace metal grade HNO_3, and 3) filling the tubes completely with Nano-pure H_2O, replacing the cap, vigorously shaking to remove any residual acid, and finally emptying the tubes and shook dry.

2.5.1.2 Solid Sample Preparation

Upon completion of container preparation, some of the centrifuge tubes were set aside to be used for solid samples while the others were to be used for fluid samples. Approximately 1 mg of sample per experiment was placed into a single centrifuge tube. The mass of each sample was determined using a Sartorius M2P microbalance with an

accuracy of ±0.001 mg. Finally, 10 ml of 2% trace metal grade HNO_3 was added to each tube.

2.5.1.3 Fluid Sample Preparation

The fluid samples were prepared via dilution whereby either 100 µl of sample was added to the centrifuge tubes and then diluted to 10 ml with 2% trace metal grade HNO_3 (i.e. 9.9 ml of acid to 0.1 ml of sample) or 400 µl of sample was added to the centrifuge tubes and then diluted to 10 ml with 2% trace metal grade HNO_3 (i.e. 9.6 ml of acid to 0.4 ml of sample). The reason for two different dilution methods was due to the fact that some of the fluid samples had already been acidified with 2% trace metal grade HNO_3 for preservation purposes with a ratio of 3 ml of acid to 1 ml of sample. The tops of the centrifuge tubes were then replaced and wrapped with parafilm and the centrifuge tubes were placed in a fridge pending transport.

2.5.2 Raman Spectroscopy and Powdered X-ray Diffraction Analyses

Raman spectroscopy at Rensselaer Polytechnic Institute (RPI) was performed by analysis of standards of calcite and aragonite from the RPI mineral collection and then comparing the peaks of the standards to those of HP-RPI-02 to determine the phase of precipitated $CaCO_3$. Measurements were performed using a Bruker SENTERRA dispersive Raman microscope with an AlGaAs diode laser at 785 nm excitation, 50x1000 µm slit, and an air cooled CCD.

Powdered X-ray diffraction (XRD) analyses were conducted for solid samples collected from experiments HP-RPI-2 and LP-02′ to determine mineral composition. Analyses were performed using a Siemens D-500 X-ray diffractometer with PSD

detector. All data interpretations were conducted using MDI Jade 2010 software package, at Mississippi State University Institute for Imaging and Analytical Technology (I2AT). The XRD pattern for each sample was obtained using CuKα radiation with a wavelength of 1.54059 Å.

2.5.3 EMPA: Sample Preparation and Analytical Parameters

A Cameca SX-100 Electron Mirco-Probe Analyzer (EMPA) at RPI was used to determine the composition of aragonite samples from the following experiments: LP-02', LP-03', HP-01, HP-02, HP-RPI-2, and to assess elemental distribution within the samples. To accomplish this, samples were mounted in EpoxiCure epoxy resin and hardener, supplied by Buehler, which was mixed by mass with a 4:1 ratio, respectively. Once hardened, the mount was then polished to the epoxy-crystal surface interface using 240 grit (particle size of 53 μm), 400 (22 μm), 600 (15 μm), 800 (12.6 μm), and 1200 (8.4 μm) silicon carbide grinding paper. The epoxy mounts were then polished a final time using 1 μm alumina powder and a South Bay Technology Model 920 lapping and polishing machine. The analysis was conducted using wavelength dispersive X-ray spectroscopy (WDS) and backscattered electron (BSE) imaging. The EMPA was conducted using five-minute acquisition at 15 keV, 20 nA, and a 20 μm beam. The following elemental standards were used to calibrate the EMPA: Na (albite), Mg (synthetic forsterite), K (organic standard), Ca (calcite), Fe (iron), Mn (tephroite), Cl (sodalite), Sr (strontianite), S (pyrite), and P (apatite) [information in parentheses denotes source of element used in standard].

2.5.4 Optical Microscopy

Optical analysis of precipitated crystals from all experiments were conducted using a Huvitz HRM-300 Upright Microscope with Reflected and Transmitted Light Illumination. Crystals produced from the experiments were examined to determine if those which were precipitated at different pressures displayed different morphologies (see Figures 2.4 and 2.5).

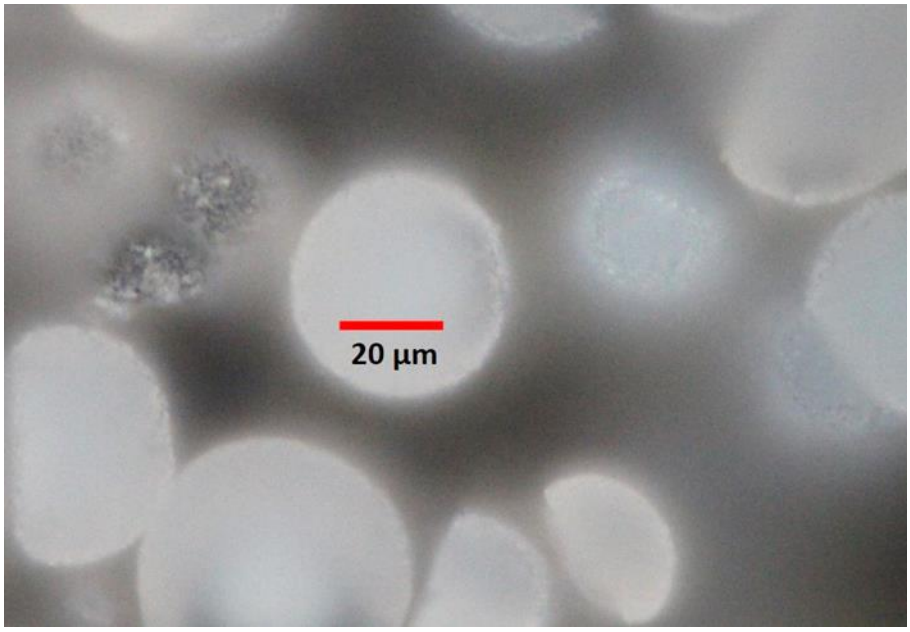

Figure 2.4 Optical microscopy image taken of crystals produced from the LP experiments using reflected light

Scale is 20 µm.

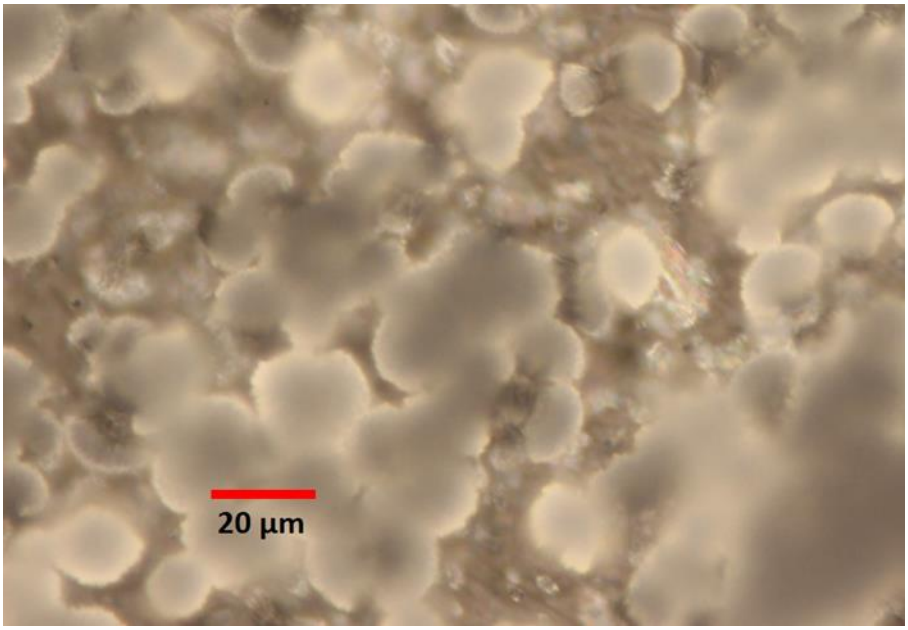

Figure 2.5 Optical microscopy image taken of crystals produced from the HP experiments using reflected light

Scale is 20 µm.

2.6 Results

2.6.1 Results of Raman Spectroscopy and X-ray Diffraction Analyses

For aragonite, there are three main peaks which differentiate its signature from calcite. Those peaks occur at a Raman Shift (cm^{-1}) of approximately 150, 200, and 1350 to 1400 (Figure 2.6). To corroborate the results of the Raman spectroscopy powdered X-ray diffraction was conducted on samples collected from experiments HP-RPI-2 (7.8 °C, 345 bars) and LP-02′ (7.8 °C, 1 bar) (see Figure 2.7). Aragonite was the only mineral precipitated in HP-RPI-2 but monohydrocalcite was present in addition to aragonite in LP-02′.

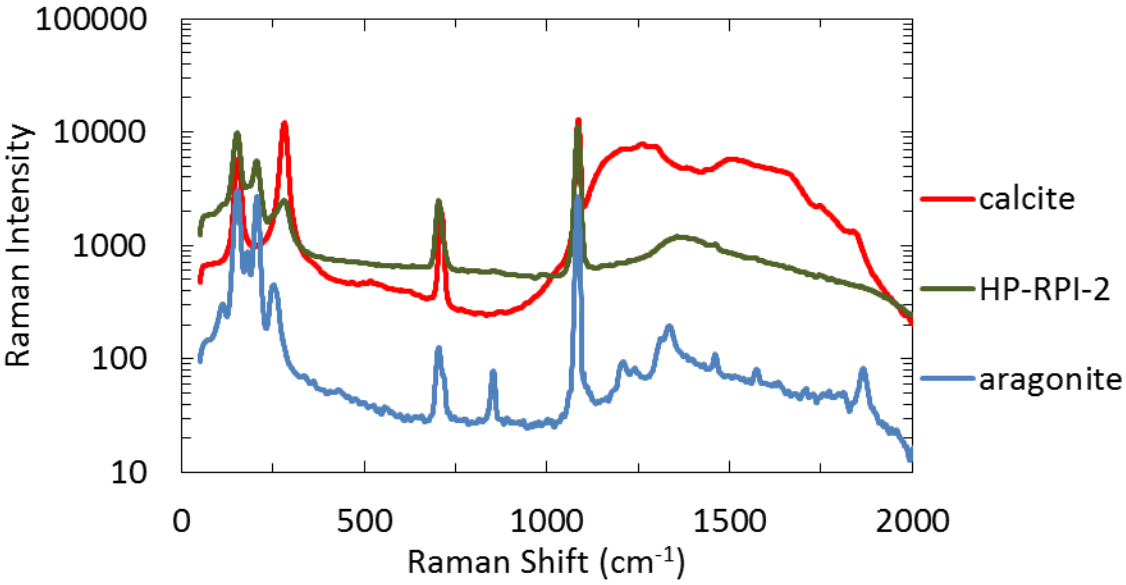

Figure 2.6 Results from Raman spectroscopy analysis

Raman intensity was plotted against Raman shift (cm^{-1}) for aragonite and calcite standards and samples from experiment HP-RPI-2.

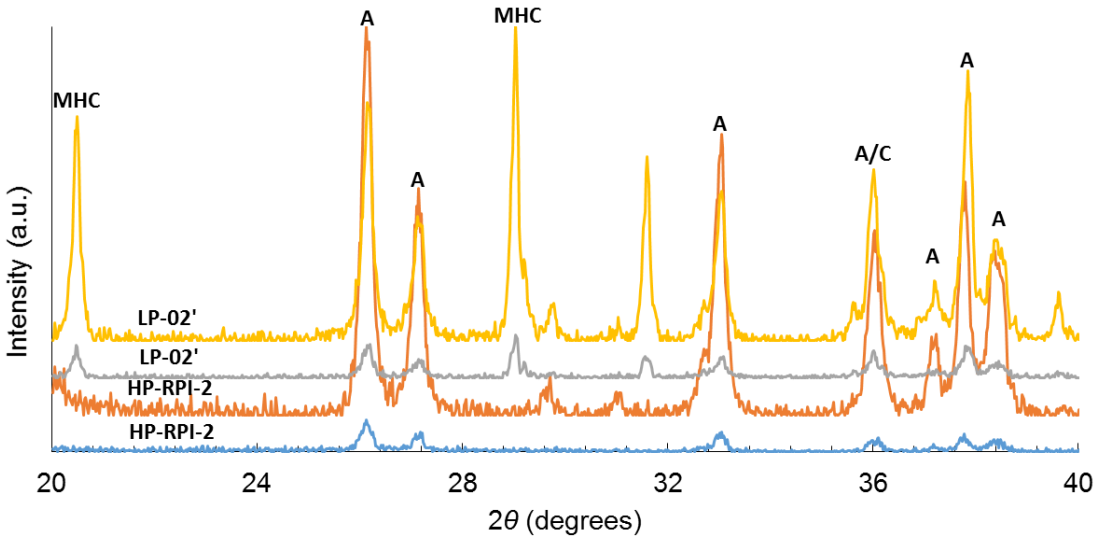

Figure 2.7 Powdered X-ray diffraction scans with Cu-Kα radiation of different calcium carbonate polymorphs.

A = aragonite, MHC = monohydrocalcite, A/C indicates the position of the peak that is representative of both calcite and aragonite. The experiment which corresponds with the diffraction pattern is noted near the y-axis of the plot.

2.6.2 Results of ICP-MS and EMPA Analyses

The data collected on precipitated aragonite using ICP-MS and EMPA are presented in Table 2.3. The few samples which were measured using EMPA yielded high heterogeneity up to 0.14 % within individual experiment, which was on average an order of magnitude greater than s.e. of ICP-MS data (0.005 %). Therefore, EMPA data were not used for any additional analyses mentioned herein. The data on aqueous samples using ICP-MS can be found in Table 2.4. The information found in Table 2.3 was redefined in terms of total moles of each element in solid samples using the following expression:

$$m_i^{Aragonite} = x_i \cdot 10^{-6} \cdot M_{calcite} / M_i \cdot m_{(Ca)}^{Aragonite} \quad (2.3)$$

where $m_i^{Aragonite}$ is the total moles of the element of interest present in aragonite, x_i is the concentration of this element in ppm, M is the molar mass of calcite or element of interest in g/mol, and $m_{(Ca)}^{Aragonite}$ is the moles of calcium in aragonite (see Table 2.5). The moles of calcium in aragonite was calculated by considering the following:

$$m_{(Ca)}^{Aragonite} = m_{(Ca)}^{ASW} - m_{(Ca)}^{Fluid} \quad (2.4)$$

where $m_{(Ca)}^{ASW}$ is the moles of calcium present in the initial solution of artificial seawater and $m_{(Ca)}^{Fluid}$ is the total moles of calcium present in the final fluid. Calculations were performed to determine total moles of each element remained in final fluid at the end of experiment (Table 2.4):

$$m_i^{Fluid} = x_i / 1000 \cdot \dot{V} / 1000 / M_i \quad (2.5)$$

where m_i^{Fluid} is the total moles of the element of interest present in the aqueous sample, x_i is the concentration of this element in ppm, $\dot{V}$ is the final fluid volume in ml, and M_i is the molar mass of element in g/mol (see Table 2.6).

Table 2.3 Elemental concentrations in solid samples determined using ICP-MS and EMPA

Experiment	Dilution factor (ppm)	Elemental concentration*					
		Li	B	Na	Mg	S	Ca
LP-02'	10132.58	1.47 ± 0.02	78.92 ± 0.46	3535.46 ± 11.65	22702.3 ± 162.30	4113.89 ± 387.09	345249.30 ± 3173.70
LP-03'	9975.66	1.20 ± 0.02	35.57 ± 0.86	4404.34 ± 15.96	1779.60 ± 2.44	2984.56 ± 436.25	399650.79 ± 2854.31
LP-03' (EMPA)	—	—	—	4672.54 ± 143.26	2222.99 ± 158.83	1032.46 ± 65.84	355784.68 ± 13442.73
HP-01	10492.15	1.36 ± 0.02	31.66 ± 0.34	4327.93 ± 35.74	9166.97 ± 98.79	2631.86 ± 478.71	374019.68 ± 4486.50
HP-01 (EMPA)	—	—	—	4208.13 ± 127.65	2179.99 ± 85.35	805.30 ± 20.30	371858.88 ± 1184.25
HP-02	9159.05	1.55 ± 0.01	30.11 ± 0.31	6043.98 ± 23.21	6030.74 ± 27.17	2352.45 ± 324.95	370650.59 ± 2962.68
HP-02 (EMPA)	—	—	—	5258.35 ± 130.05	2566.70 ± 357.88	1162.16 ± 30.26	363604.66 ± 2102.38
HP-25	8139.84	1.12 ± 0.01	31.21 ± 0.27	4311.33 ± 58.56	6238.14 ± 41.10	2777.62 ± 405.41	351692.57 ± 4739.43
HP-75	4278.63	0.77 ± 0.01	30.30 ± 0.26	4121.10 ± 30.13	2667.71 ± 22.73	2219.90 ± 382.81	256029.13 ± 2381.90
HP-RPI-2	6377.07	4.10 ± 0.05	58.97 ± 0.57	5167.47 ± 817.37	128867 ± 26063.7	2274.84 ± 92.92	403181.50 ± 87784.74

Table 2.3 (continued)

V	Mn	Fe	Cu	Zn	Sr	Ba
1.08 ± 0.01	15.87 ± 0.02	481.83 ± 4.41	9.00 ± 0.05	411.58 ± 1.16	8355.51 ± 96.45	31.23 ± 0.25
0.75 ± 0.01	18.38 ± 0.18	8.26 ± 0.04	5.44 ± 0.06	76.09 ± 0.39	9945.47 ± 51.39	32.49 ± 0.17
—	—	87.52 ± 47.34	—	—	9729.70 ± 150.29	—
0.11 ± 0.01	113.82 ± 1.10	29.71 ± 0.58	5.02 ± 0.07	14.00 ± 0.14	8969.32 ± 46.05	31.12 ± 0.07
—	—	—	—	—	9156.37 ± 100.88	—
0.13 ± 0.00	219.12 ± 1.20	183.00 ± 0.83	14.10 ± 0.10	52.27 ± 0.43	9076.61 ± 52.30	31.72 ± 0.29
—	—	—	—	—	9246.74 ± 111.97	—
0.06 ± 0.00	109.19 ± 1.24	34.29 ± 0.40	346.64 ± 2.33	568.71 ± 4.47	8600.36 ± 142.56	29.07 ± 0.27
1.62 ± 0.03	474.44 ± 3.61	15956.74 ± 66.77	807.49 ± 0.75	8715.44 ± 43.89	6511.06 ± 51.56	29.02 ± 0.20
0.01 ± 0.00	56.60 ± 11.84	157.61 ± 35.64	53.28 ± 10.36	5.43 ± 1.26	9471.34 ± 1887.39	37.78 ± 7.18

*All units for elemental concentrations are expressed in ppm.
(EMPA) indicates samples from experiments which were analyzed using electron micro-probe in addition to ICP-MS.

Table 2.4 Elemental concentrations in aqueous samples

Experiment	Dilution factor (ppm)	Elemental concentration*					
		Li	B	Na	Mg	S	Ca
LP-02'	10132.58	0.18 ± 0.00	2.89 ± 0.05	5988.13 ± 71.65	685.81 ± 7.18	484.27 ± 2.40	56.15 ± 0.85
LP-03'	9975.66	0.25 ± 0.01	4.10 ± 0.14	8023.03 ± 41.42	1039.39 ± 8.06	755.09 ± 13.84	69.68 ± 1.66
HP-01	10492.15	0.27 ± 0.01	3.72 ± 0.06	9189.46 ± 71.03	1103.86 ± 9.32	801.69 ± 6.51	141.86 ± 3.51
HP-02	9159.05	0.29 ± 0.00	4.73 ± 0.09	9595.59 ± 87.34	1227.93 ± 10.56	849.66 ± 11.28	113.88 ± 2.44
HP-25	8139.84	0.22 ± 0.00	3.56 ± 0.05	6682.65 ± 74.87	792.50 ± 5.48	731.16 ± 13.62	79.99 ± 4.08
HP-75	4278.63	0.27 ± 0.00	4.35 ± 0.08	7690.78 ± 49.06	933.45 ± 1.66	732.03 ± 10.01	121.53 ± 1.83
HP-RPI-2	6377.07	0.29 ± 0.00	4.84 ± 0.11	9285.38 ± 34.20	1197.05 ± 6.90	817.19 ± 6.11	99.57 ± 0.49

Table 2.4 (continued)

V	Mn	Fe	Cu	Zn	Sr	Ba
BADL	BADL	BADL	BADL	BADL	2.05 ± 0.02	BADL
BADL	BADL	BADL	BADL	BADL	1.72 ± 0.01	BADL
BADL	5.28 ± 0.01	0.12 ± 0.00	0.01 ± 0.00	BADL	2.09 ± 0.02	BADL
BADL	0.18 ± 0.00	0.01 ± 0.00	BADL	BADL	1.90 ± 0.00	BADL
BADL	0.05 ± 0.00	0.16 ± 0.00	0.28 ± 0.00	BADL	1.63 ± 0.01	BADL
BADL	0.27 ± 0.00	0.51 ± 0.00	0.82 ± 0.00	BADL	2.60 ± 0.01	0.01 ± 0.00
BADL	BADL	BADL	BADL	BADL	1.87 ± 0.00	BADL

*All units for elemental concentrations are expressed in ppm.
BADL = Below Analytical Detection Limit

Table 2.5 Total moles of element in fluid

Experiment	Li	B	Na	Mg	S	Ca
LP-02'	5.92E-06	5.99E-05	5.83E-02	6.32E-03	3.38E-03	3.14E-04
LP-03'	8.05E-06	8.50E-05	7.82E-02	9.58E-03	5.28E-03	3.89E-04
HP-01	8.85E-06	7.71E-05	8.95E-02	1.02E-02	5.60E-03	7.93E-04
HP-02	9.36E-06	9.79E-05	9.35E-02	1.13E-02	5.94E-03	6.37E-04
HP-25	5.37E-06	5.67E-05	5.00E-02	5.61E-03	3.92E-03	3.43E-04
HP-75	6.61E-06	6.91E-05	5.75E-02	6.61E-03	3.93E-03	5.22E-04
HP-RPI-2	3.13E-05	3.36E-04	3.03E-01	3.69E-02	1.91E-02	1.86E-03

Table 2.5 (continued)

V	Mn	Fe	Cu	Sr	Ba
6.68E-10	2.96E-09	1.41E-08	0.00E+00	5.25E-06	5.42E-09
8.65E-10	1.15E-08	1.13E-08	0.00E+00	4.4E-06	5.97E-09
9.30E-10	2.15E-05	4.69E-07	4.97E-08	5.34E-06	4.33E-09
9.98E-10	7.53E-07	4.25E-08	9.07E-09	4.86E-06	4.65E-09
7.96E-10	1.64E-07	4.94E-07	7.59E-07	3.2E-06	6.07E-09
7.98E-10	8.30E-07	1.57E-06	2.22E-06	5.11E-06	1.08E-08
3.03E-09	4.86E-08	4.15E-08	1.57E-08	1.6E-05	2.28E-08

Table 2.6 Total moles of element in aragonite

Experiment	Li	B	Na	Mg	S	Ca
LP-02'	4.38E-08	1.51E-06	3.17E-05	1.93E-04	2.65E-05	2.06E-03
LP-03'	3.44E-08	6.54E-07	3.81E-05	1.46E-05	1.85E-05	1.99E-03
HP-01	3.11E-08	4.64E-07	2.98E-05	5.98E-05	1.30E-05	1.58E-03
HP-02	3.89E-08	4.85E-07	4.58E-05	4.32E-05	1.28E-05	1.74E-03
HP-25	3.29E-08	5.87E-07	3.81E-05	5.22E-05	1.76E-05	2.03E-03
HP-75	2.07E-08	5.20E-07	3.33E-05	2.04E-05	1.29E-05	1.85E-03
HP-RPI-2	4.37E-07	2.91E-06	1.20E-04	2.83E-03	3.79E-05	5.33E-03

Table 2.6 (continued)

V	Mn	Fe	Cu	Sr	Ba
4.39E-09	5.96E-08	1.78E-06	2.92E-08	1.97E-05	4.69E-08
2.92E-09	6.65E-08	2.94E-08	1.70E-08	2.26E-05	4.7E-08
3.43E-10	3.28E-07	8.43E-08	1.25E-08	1.62E-05	3.59E-08
4.41E-10	6.94E-07	5.7E-07	3.86E-08	1.8E-05	4.02E-08
2.58E-10	4.04E-07	1.25E-07	1.11E-06	2E-05	4.31E-08
5.90E-09	1.60E-06	5.3E-05	2.36E-06	1.38E-05	3.92E-08
7.09E-11	5.50E-07	1.51E-06	4.47E-07	5.77E-05	1.47E-07

Using the values presented in Tables 2.5 and 2.6 it was possible to determine the partitioning (K^i) of various elements to aragonite. The common way to determine partition coefficient using the non-thermodynamic relationship would be expressed as:

$$K^{Mg} = \frac{(Mg/Ca)_{Solid}}{(Mg/Ca)_{Fluid}} \tag{2.6}$$

however, this method was not used because element to calcium ratio in fluid was continuously changing during experiments due to different consumption rates of Ca and other elements from fluid during crystallization of $CaCO_3$. Therefore, the Doerner-Hoskins partition coefficient (designed for closed finite reservoirs) was used to determine K_d for our data instead of the non-thermodynamic relationship because fluids and solids in the precipitation vessels were allowed to evolve over the course of the experiments. To determine K_d, the Doerner-Hoskins relationship was utilized which can be described as:

$$\log\left(1 + \frac{m_i^{Aragonite}}{m_i^{Fluid}}\right) = K_d^{i/Ca} \log\left(1 + \frac{m_{Ca}^{Aragonite}}{m_{Ca}^{Fluid}}\right) \tag{2.7}$$

where $m_i^{Aragonite}$ is the total number of moles of element (i) in the final solid, and m_i^{Fluid} is the total number of moles of element (i) in the final fluid (Doerner and Hoskins, 1925).

Partitioning values for Li, Mg, S, V, Mn, Fe, Cu, Sr, and Ba were determined for each experiment and are shown in Table 2.7.

Table 2.7 Partitioning data

Experiment	Pressure (bar)	K^{Li}	err.	K^{Mg}	err.	K^{S}	err.	K^{V}	err.
LP-02'	1	0.004	4.53E-05	0.015	5.73E-04	0.004	2.03E-04	1.000	5.54E-02
LP-03'	1	0.002	2.91E-05	0.001	3.18E-05	0.002	1.01E-04	0.816	3.17E-02
HP-01	100	0.003	6.53E-05	0.005	3.35E-04	0.002	1.83E-04	0.286	9.46E-03
HP-02	100	0.003	5.70E-05	0.003	1.61E-04	0.002	1.25E-04	0.278	8.35E-03
HP-25	25	0.003	4.09E-05	0.005	1.90E-04	0.002	1.27E-04	0.145	2.97E-03
HP-75	75	0.002	4.78E-05	0.002	1.44E-04	0.002	2.11E-04	1.403	1.55E-01
HP-RPI-2	345	0.010	1.68E-04	0.001	5.56E-05	0.001	1.01E-04	0.017	3.88E-04

Table 2.7 (continued)

K^{Mn}	err.	K^{Fe}	err.	K^{Cu}	err.	K^{Sr}	err.	K^{Ba}	err.
1.507	1.15E-01	2.393	0.688	—	—	0.769	0.024	1.120	0.063
1.060	3.70E-02	0.710	0.016	—	—	1.003	0.036	1.207	0.064
0.014	2.65E-04	0.151	0.003	0.205	0.004	1.271	0.059	2.031	0.184
0.496	1.18E-02	2.026	0.164	1.260	0.053	1.177	0.053	1.720	0.141
0.643	1.54E-02	0.116	0.002	0.466	0.009	1.023	0.043	1.081	0.057
0.709	2.75E-02	2.342	0.461	0.477	0.015	0.863	0.043	1.013	0.066
1.858	1.27E-01	2.678	0.389	2.504	0.311	1.129	0.045	1.485	0.093

All HP experiments were pressurized using high purity N_2 gas.

Optical microscopy revealed that all precipitated solids are comprised of hemispherical bundles of needles called spherulites. The average spherulite diameter was different for each of the experiments: LP-02′ (30), LP-03′ (40), HP-25 (3), HP-75 (10), HP-01 (15), HP-02 (17.5), HP-RPI-2 (7.5), values in parentheses are in μm. No systematic relationship of spherulite size with pressure was established, but the smallest crystals were produced at the highest pressure of 345 bar. The results of the experiments in this study suggest that the influence of pressure on elemental incorporation to aragonite is negligible compared to the heterogeneity within spherules and between identical experiments.

2.7 Discussion

It can be presumed that the precipitation of aragonite in the experiments conducted at room temperature is due to the temperature dependence of calcium carbonate polymorphs where precipitation of aragonite is favorable at higher temperatures (Morse et al., 1997). It is known that at surface temperatures and pressures, monohydrocalcite is thermodynamically unstable relative to anhydrous calcite and aragonite (Rodriguez-Blanco et al., 2014). Even minor concentration of Mg in the fluid will lead monohydrocalcite to transform to aragonite at ambient temperatures (Brooks et al., 1950; Kamiya et al., 1977; Dahl and Buchardt, 2006; Munemoto and Fukushi, 2008; Fukushi et al., 2011). In the laboratory, monohydrocalcite easily precipitated from artificial seawater as a precursor of aragonite (Kinsman and Holland, 1969). The fact that monohydrocalcite acts as a precursor to aragonite may serve to explain why its presence did not appreciably effect the calculation K_d or may also be due to the fact that aragonite was far more abundant in samples from low temperature experiments.

The absence of monohydrocalcite in the experiment HP-RPI-2 (7.8°C and 345 bars) is intriguing and suggests that high pressure favors aragonite precipitation over other $CaCO_3$ polymorphs at 7.8°C and 345 bars, which are far below T and P reported for aragonite stability field (Jamieson, 1953). The smallest size of aragonite crystals in this low T and high P experiment (HP-RPI-2) underscores the significance of ocean floor pressure on crystallization of $CaCO_3$. This provided an opportunity to compare the values for elemental partitioning in this study to those in the existing literature (see Figures 2.8 through 2.11). The information presented in Table 2.8 is the partitioning data for multiple elements with respect to aragonite. Note that for experiment HP-RPI-2 the lithium partitioning value (0.0102) has been excluded from Figure 2.8 as it is an order of magnitude larger than the values from the other experiments in this study. One explanation for this could be that the pressure vessel was contaminated with lithium prior to the start of the experiment.

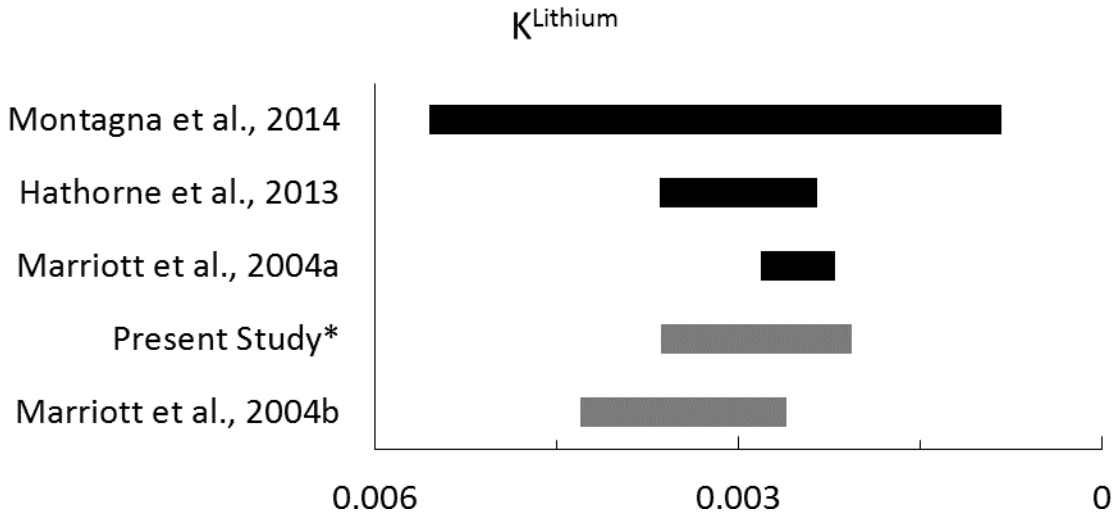

Figure 2.8 Partitioning of lithium to aragonite

(note the reverse axis).
* indicates that the lithium partitioning value for experiment HP-RPI-2 (0.0102) was not included in the values reported here as it is believed that the reaction vessel may have been contaminated with lithium. Black indicates sampled aragonite has a biogenic origin (Corals: Marriott et al., 2004a; Hathorne et al., 2013; Montagna et al., 2014) while gray indicates sampled aragonite was precipitated inorganically. Values reported were for aragonite which precipitated between 5 to 25 °C and 1 to 345 bar.

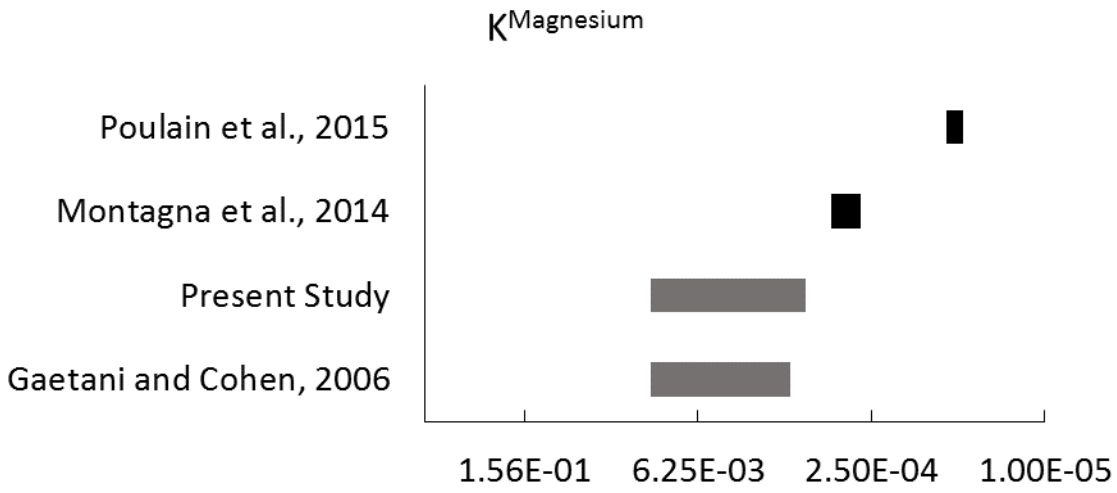

Figure 2.9 Partitioning of magnesium to aragonite.

Black indicates sampled aragonite has a biogenic origin (Bivalves: Poulain et al., 2015; Corals: Montagna et al., 2014) while gray indicates sampled aragonite was precipitated inorganically. Values reported were for aragonite which precipitated between 5 to 25 °C and 1 to 345 bar.

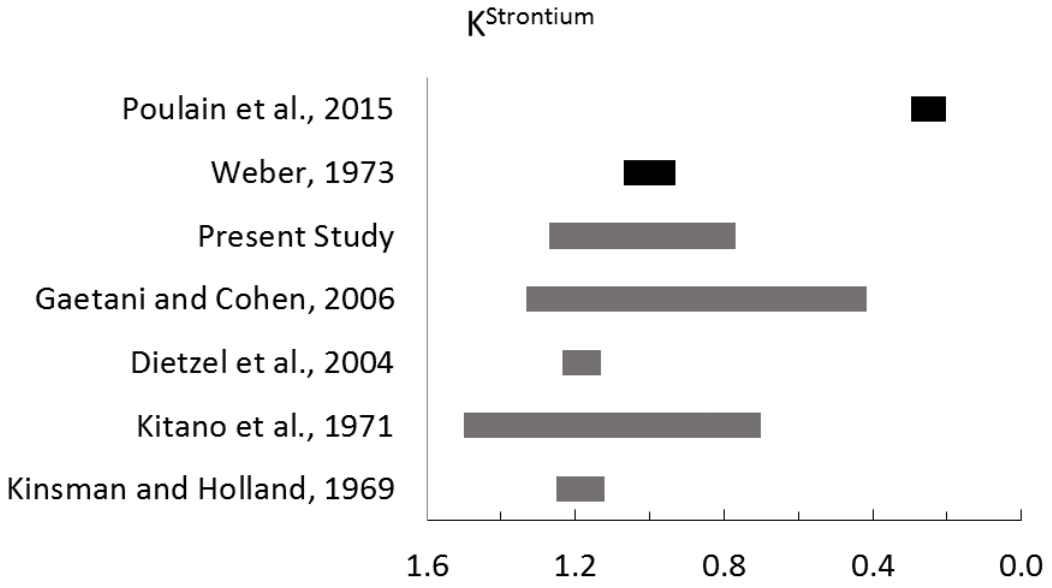

Figure 2.10 Partitioning of strontium to aragonite.

Black indicates sampled aragonite has a biogenic origin (Bivalves: Poulain et al., 2015; Corals: Weber, 1973) while gray indicates sampled aragonite was precipitated inorganically. Values reported were for aragonite which precipitated between 5 to 25 °C and 1 to 345 bar.

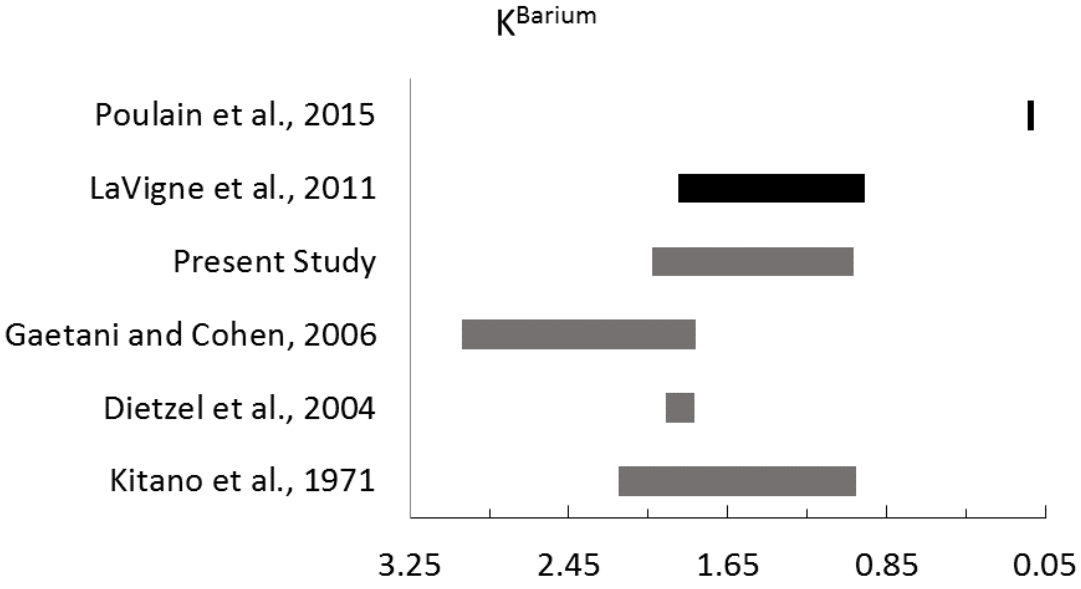

Figure 2.11 Partitioning of barium to aragonite.

Black indicates sampled aragonite has a biogenic origin (Bivalves: Poulain et al., 2015; Corals: LaVigne et al., 2011) while gray indicates sampled aragonite was precipitated inorganically.

Table 2.8 Partitioning of minor elements to aragonite

$K_d^{i/Ca}$	Minimum K value	Maximum K value	Study	Sample
Li/Ca	2.60E-03	4.30E-03	Marriott et al., 2004b	Inorganic
	2.06E-03	3.64E-03	Present Study*	Inorganic
	2.20E-03	2.82E-03	Marriott et al., 2004a	Biogenic
	2.35E-03	3.65E-03	Hathorne et al., 2013	Biogenic
	8.27E-04	5.55E-03	Montagna et al., 2014	Biogenic
Mg/Ca	1.13E-03	1.49E-02	Gaetani and Cohen, 2006	Inorganic
	8.40E-04	1.48E-02	Present Study	Inorganic
	3.03E-04	5.22E-04	Montagna et al., 2014	Inorganic
	4.60E-05	6.20E-05	Poulain et al., 2015	Biogenic
S/Ca	1.46E-03	3.85E-03	Present Study	Inorganic
V/Ca	1.71E-02	1.40E+00	Present Study	Inorganic
Mn/Ca	1.38E-02	1.86E+00	Present Study	Inorganic
Fe/Ca	1.16E-01	2.68E+00	Present Study	Inorganic
Cu/Ca	2.80E+00	9.90E+00	Kitano et al., 1971	Inorganic
	2.05E-01	2.50E+00	Present Study	Inorganic
Sr/Ca	1.12E+00	1.25E+00	Kinsman and Holland, 1969	Inorganic
	7.00E-01	1.50E+00	Kitano et al., 1971	Inorganic
	1.13E+00	1.23E+00	Dietzel et al., 2004	Inorganic
	4.17E-01	1.33E+00	Gaetani and Cohen, 2006	Inorganic
	7.69E-01	1.27E+00	Present Study	Inorganic
	9.30E-01	1.07E+00	Weber, 1973	Biogenic
	2.02E-01	2.98E-01	Poulain et al., 2015	Biogenic
Ba/Ca	1.00E+00	2.20E+00	Kitano et al., 1971	Inorganic
	1.82E+00	1.96E+00	Dietzel et al., 2004	Inorganic
	1.81E+00	2.99E+00	Gaetani and Cohen, 2006	Inorganic
	1.01E+00	2.03E+00	Present Study	Inorganic
	9.60E-01	1.90E+00	LaVigne et al., 2011	Biogenic
	1.07E-01	1.37E-01	Poulain et al., 2015	Biogenic

Values reported for inorganic aragonite precipitated between 5 to 25 °C and 1 to 345 bar.

Our K values were compared with those calculated from elemental concentrations in natural samples of bivalves (Poulain et al., 2015) and corals (Marriott et al., 2004a and Hathorn et al., 2013; Montagna et a., 2014). We found that aragonitic bivalves possess noticeably lower concentrations of K(Mg, Sr, Ba) than coralline aragonites and inorganic

aragonites (see Table 2.8). This may be the result of the active physiological control of chemical composition of calcifying fluid (where biomineralization occurs). In contrast coral K(Mg, Sr, Ba, Li) values (Weber, 1973; Marriott et al., 2004a; LaVigne et al., 2011; Hathorne et al., 2013; Montagna et a., 2014), overlap or are more similar with those evaluated for inorganically precipitated aragonite, underscoring a significant difference in controlling of calcifying fluid chemistry by corals than by bivalves.

This study has shown that it is possible to collect partitioning data for sulfur from inorganic samples and it may also be possible collect it from fossilized biogenic aragonite to determine the timing of major volcanic events. Manganese and iron abundancies in foraminiferal calcite have been used as a proxy for determining oxygen depletion (Glock et al., 2012), and may also be applicable for biogenic aragonite; it is also possible that copper may be used for this purpose as it is a multivalence metal. Vanadium abundances in aragonite could be utilized to derive information regarding changes in the areal extent of reducing sediments over glacial-interglacial time scales (Hastings et al., 1996).

2.8 Conclusions

This study provides evidence that oceanic floor pressure could affect the crystallization of $CaCO_3$ by altering mineralogical composition and aragonite crystal size. Partition coefficients of vanadium, manganese, and iron between synthetic aragonite and fluid were determined for the first time. Additional research is needed to assess the aforementioned relationships and further explore variability among precipitated crystals.

CHAPTER III

EFFECT OF GROWTH RATE ON URANIUM PARTITIONING BETWEEN CALCITE AND FLUID

3.1 Abstract

Elemental to calcium ratios in calcium carbonate minerals are being used to study environmental conditions at which crystallization occurred. In particular, U/Ca has been proposed as proxy for determining aspects of the paleoclimate such as the seawater carbonate ion concentration (CO_3^{2-}) and seawater pH. However, the kinetic effect of U/Ca incorporation into calcite is not well understood. This work is focused on the evaluation of growth rate and its effect on element partitioning between calcite and fluid. The calcite crystals produced during this study were crystallized isothermally from NH_4Cl-$CaCl_2$ doped with uranium by diffusion of CO_2. Calcite growth rate (i.e. crystal extension rate, V) was monitored by sequentially spiking calcite-precipitating fluids with rare earth element (REE) dopants. The REE were analyzed with SIMS at spots matching those where U/Ca was determined. Partition coefficients $K^U=(U/Ca)_{calcite}/(U/Ca)_{fluid}$ increases with increasing of growth (crystal extension) rate (V). K^U increases by a factor of two when V increases from 0.01 to 0.14 nm/s and remained near constant at faster rates. Numerical simulations using the growth entrapment model (GEM) and unified uptake kinetics model (UUKM) were undertaking in order to explain K^U-V relationship in the recent data on calcite.

3.2 Introduction

Uranium is a trace element commonly present in calcium carbonate minerals found in marine and terrestrial environments (e.g. Reeder et al., 2001; Dunk et al., 2002). Presence of uranium in calcite is of value to the geological community as it is utilized in U-series age-dating as a geochronological tool (e.g. Lundberg and Ford, 1994; Ku et al., 1998). The U/Ca ratio is being used to track geologic events, climatic variations, and the ocean uranium budget though preservation of its signature in calcite (e.g. Russell et al., 1994; Min et al., 1995; Dunk et al., 2002). It is known from the work of Russell et al. (2004) and supported by the findings of Keul et al. (2013) that U/Ca ratios in foraminiferal calcite decreases by 25 ± 7% per 100 μmol kg^{-1} as [CO_3^{-2}] in seawater increases from 110 to 470 μmol kg^{-1}. This is because uranium easily reacts with aqueous carbonate species, therefore speciation is dependent on available [CO_3^{2-}] in seawater (Keul et al., 2013). Moreover, as the abundance of the carbonate ion increases the diversity of uranium-carbonate complexes increases (e.g. [$UO_2(CO_3)_{(aq)}$], [$UO_2(CO_3)_3^{4-}$], and [$UO_2(CO_3)_2^{2-}$]) (Keul et al., 2013). As the sum of the different carbonate complexes increases the percentage of free forms [UO_2^{+2}] and [$UO_2(CO_3)_2^{2-}$] decreases (Keul et al., 2013). In addition, uranium has been proposed for determining paleo-pH, using coral skeletons and polyps, respectively (Min et al., 1995; Inoue et al., 2011); and ocean redox chemistry proxies using foraminiferal coatings (Boiteau et al., 2012). Foraminiferal coatings are produced by authigenic uranium within pore waters accumulating on the foraminiferal shell creating a non-lattice bound layer of calcite with elevated concentrations of uranium. It was shown by Inoue et al. (2011) that as pH increases, the U/Ca ratio decreases in skeletal coral polyps by -1.5 ± 0.2% change per 0.1 pH unit.

Moreover, it was demonstrated by Boiteau et al. (2012) that a recurring pattern of higher U/Ca (70-320 nmol/mol), on foraminiferal coatings, exists during glacial rather than inter-glacial periods. In Figure 2a of Boiteau et al. (2012) a very convincing relationship is shown correlating Marine Isotope Stage 8, 10, 12, and 14 to elevated U/Ca signatures in foraminiferal coatings. During the glacial periods mentioned above, the U/Ca ratios increased by nearly 50 to 250 nmol/mol for foraminiferal species *G. bulloides*, *G. inflate*, and *Uvigerinai* spp. (Boiteau et al., 2012). It may also be possible to use U/Ca in foraminiferal coatings as a proxy for determining sedimentary redox changes (Boiteau et al. 2012).

Uranium found in fluids are present mainly as aqueous species of uranium with respect to natural pH and oxygen potential (Eh) for environments where natural calcite occurs. The uranium oxidation state varies in geological environments. For example, dissolved U(VI) can be drawn into suboxic sediments which is then reduced to form insoluble U(IV) that is precipitated from pore waters (Klinkhammer and Palmer, 1991; Boiteau et al., 2012). Uranium concentrations in natural calcite are typically less than 10 ppm (Reeder et al., 2001); though it was noted by Reeder et al. (2001), that such low concentrations in the natural solid state may reflect low uranium concentrations in the natural fluids from which they formed. In some unique cases, uranium concentrations in natural calcite (e.g. tufa, speleothems, foraminifera) have been reported to exceed 300 ppm (Spötl et al., 2002; Cole et al., 2004; Sano et al., 2005; Valle-Fuentes et al., 2007). Therefore, it is not surprising that Reeder et al. (2001) reported it is possible to produce synthetic uranium co-precipitated with calcite up to 1900 ppm in laboratory settings.

It was shown that U/Ca is heterogeneous in calcite grown at near-constant temperature, pH, Eh, and fluid composition (e.g. Reeder et al., 2001; Raitzsch et al., 2011). In Sturchio et al., (1998), it was demonstrated that the distribution of uranium in calcite is heterogeneous by conduction of X-ray fluorescence mapping. Therefore, it is important to evaluate the kinetic effect on partitioning of uranium between calcite and fluid, which is the focus of the present study.

The strong influence of growth rate on partitioning of divalent cations between calcite in fluid has been reported by several authors (e.g. Lorens, 1981; Tesoriero and Pankow, 1996; Gabitov and Watson, 2006; Lakshtanov and Stipp, 2007; Tang et al., 2008a; Saulnier et al., 2012; Mavromatis et al., 2013; Gabitov et al., 2014a). Uranium partitioning data are restricted to the work of Kitano and Oomori (1971) where the calcite growth rate was not determined and K^U was found to vary between 0.0n to 0.2 (no definition for n was observed in their paper).

This work is concerned with the dependence of K^U on the crystal extension rate as evaluated in individual calcite crystals. The choice of $K^U=(U/Ca)_{calcite}/(U/Ca)_{fluid}$ was based on the wide use of U/Ca in studying of natural calcium carbonates. Growth rate values for this study were determined *in-situ* as; the width of the layers of calcite divided by growth time of each calcite zone (e.g. Gabitov et al., 2012). Moreover, the growth rate range of the synthetic calcite is 0.01-0.14 nm/s (0.86-12.10 μm/day). These values overlap with values reported for naturally occurring $CaCO_3$ ($3.13\cdot10^{-6}$ – 3.30 nm/s or $2.7\cdot10^{-4}$ – 285.12 μm/day) in benthic foraminifera (e.g. Ter Kuile and Erez, 1984), coccolithophorids (e.g. Stoll et al., 2002), scallops (e.g. Krantz et al., 1984; Owen et al., 2002), and speleothems (e.g. Baker et al., 1998; Genty et al., 2001; Winograd et al.,

2006). Therefore, this work is relevant to U/Ca based proxies in natural calcites, and is useful for reconstructing paleoenvironments.

In order to explain the obtained experimental data, we conducted quantitative simulations using growth entrapment (GEM) and unified uptake kinetics (UUKM) models after Watson (2004) and Thien (2014), respectively. Elemental partitioning between mineral and fluid is not a constant value; when K is predicted by thermodynamics (i.e. K at equilibrium) it corresponds to K measured at very low growth rate. In contrast disequilibrium K values are being measured in rapidly grown calcite. Several models have been developed to account for this non-equilibrium uptake of trace elements in growing minerals. The UUKM (Thien et al., 2014) is based on the two models developed by Watson (2004) and DePaolo (2011), but is implemented in the GEM-Selektor V3 geochemical modeling package (Kulik et al., 2013). The utilization of the UUKM allows the user to account for solution changes (e.g. depletion) which can influence the growth rates and therefore the value of K.

3.3 Experimental and Analytical Methods

3.3.1 Calcite precipitation

The calcite growth method used here was based on early works of Gruzensky (1967) and Paquette and Reeder (1995) but was modified by the introduction of sub-sampling and multiple REE spikes. Additional details regarding the aforementioned experiment are described in previous works of Gabitov et al. (2012), Gabitov et al. (2014a), and Gabitov et al. (2014b). The calcite growth medium was prepared by dissolving NH_4Cl in deionized (DI) H_2O to the concentration of 0.5 mol/l, along with minor amounts of reagent grade $CaCl_2 \cdot 2H_2O$ (0.01), $MgCl_2 \cdot 6H_2O$ (10^{-3}), $SrCl_2 \cdot 6H_2O$ (10^{-}

^{4}), $BaCl_2 \cdot 2H_2O$ ($2 \cdot 10^{-5}$), $LiOH \cdot H_2O$ ($5 \cdot 10^{-4}$), H_3BO_3 (0.01), and U ICP-MS standard (10^{-5}) [values in parentheses are concentrations in mol/l]. ICP-MS standard consisted of 1000 ppm of U dissolved in 2% HNO_3. The pH of the solution was initially adjusted to 5.5 by addition of reagent grade NaOH to match the pH from the study of Paquette and Reeder (1995). Calcite grew in seedless Ca-bearing fluid with an initial volume of two liters (run DC-1, Pyrex® flask, slow growth) and one liter (run DC-3, polypropylene container, fast growth) by diffusion of CO_2 (and NH_3) from slowly decomposing ammonium carbonate. This method yielded growth of large crystals (>1 mm in size) without stirring of the fluid. Mixing was applied after addition of each REE spike by repeated injection and withdrawal of fluid using a 60-ml syringe. REE spikes (Sm, La, Nd, Tb, and Pr) were sequentially introduced into the growth medium in the amount of 1 ml of diluted REE-bearing solution after 24, 36, 86, and 129 days (t_{REE}) respectively, counting time from the addition of Sm ($t_{Sm} = 0$) (Table 3.1). The entire time of calcite precipitation was 150 days. The fluids were sampled periodically for measurement of pH, and stored in a refrigerator for future use. The pH (NBS-scale) was measured immediately after collection of the fluid using an OAKTON pH 510 meter with "All-in-One" pH/Temp electrode calibrated with 7.00 and 10.00 pH buffers stored at the same temperature as the experiments. The fluid pH increased slowly during calcite precipitation from 7.96±0.06 to 8.17±0.02 (Table 3.1). Oxygen reduction potential was measured in a similar experiment and yielded oxidation conditions with an Eh of 0.127 volts. These measurements were made using a Hanna Instruments HI5521-01, SN: D0079301 equipped with a refillable combination ORP electrode HI3131B which was calibrated using HI7021 240 mV ORP solution and HI7022 470 mV ORP solution.

Table 3.1 Composition of the sampled fluids in DC-1 experiment

Sub-sample	t (days)	U/Ca (mmol/mol)	s.e.	pH	DIC (μmol/kg)	CO_3^{2-} (μmol/kg)	Ω
Initial	-43	0.919	0.065	5.5	low	low	low
Nd-spike	36	0.786	0.055	8.06	2410	170.2	1.95
Tb-spike	86	1.18	0.084	8.15	2685	229.9	2.40
Final	150	1.66	0.117	8.17	2775	247.8	1.71

Initial solution is the same for all experiments. t is the time of crystallization from the addition of Sm spike. Initial time was estimated as 43 days prior Sm addition by visual monitoring of the experimental flask with naked eye every 1-2 days. Sm, Nd, and Tb correspond to the fluid sub-sample collected just before addition of REE.
pH of the fluid at the onset of crystallization was estimated to be 7.96 ± 0.06, which is the average of pH values at t = -8 and t = 0 days. See Figure S-1 in Gabitov et al. (2012) for the whole pH record. CO_3^{2-} and Ω calculations were performed using an excel implementation of CO2SYS (Lewis and Wallace 1998), modified to use measured calcium concentrations. The constants of Millero (1995) were used for the carbonate and sulfate system, respectively. Salinity (S) of 29.4 ‰ was estimated by the amount of salts added into the initial fluid. The solubility product of calcite (K^*_{sp}) was calculated using the expression developed by Mucci (1983), yielding pK^*_{sp} of 6.46.

3.3.2 Analyses of fluids

Elemental analyses of the fluids were performed using Thermo Element XR, ICP-MS at the University of Cambridge (UK), Department of Earth Sciences, with the precision of 2-5% (1σ). Dissolved inorganic carbon (DIC) was determined using the coulometric SOMMA (Single-Operator Multi-Metabolic Analyzer) system in the Biogeochemistry Laboratory at UCLA with an accuracy of ± 2.1 μmol/kg (for details see Johnson et al., 1993).

3.3.3 In-situ analyses of calcites

XRD analyses and microscopy confirmed the precipitated phase was calcite. The crystals of the largest sizes were mounted in epoxy (EpoxiCure®, Buehler) such that the pyramid base (the crystal side adjacent to the substrate during growth) was exposed for

SIMS measurements. The mounts were polished with Buehler SiC paper of 400, 600, 800, and 1200 grit following by 1-μm size diamond paste. SIMS analyzes were conducted with CAMECA ims 1270 ion microprobe at UCLA (USA), first for Ca, REE, and U. Individual crystals were analyzed with a 3–18 nA $^{16}O^-$ primary beam at 20–30 μm lateral dimension on the sample surface. Positive secondary ions corresponding to mass/charge stations of 41.7 (background), ^{42}Ca, 87.5 (background), ^{88}Sr, ^{139}La, ^{141}Pr, ^{143}Nd, ^{149}Sm, and ^{159}Tb were measured (see Gabitov et al., 2012 for details). To reduce molecular interferences, Ca and REE were analyzed with a sample voltage offset of −60 V, and using the energy bandwidth of 50 V (total voltage was 10 keV). It was shown that energy filtering reduces molecular interferences during measurements of ^{42}Ca and ^{88}Sr from carbonate materials down to 0.3% (Herzog et al., 1973; Shimizu et al., 1978; Allison, 1996; Hart and Cohen, 1996; Denniston et al., 1997; Gaetani and Cohen, 2006; Gabitov et al., 2013). REE were analyzed for identification of spiked REE zones only.

During another analytical session at similar tuning conditions $^{238}U/^{42}Ca$ were measured. The reproducibility was first tested on NIST-612 glass where 1 s.d. of $^{238}U/^{42}Ca$ was 1.2% between 9 spot analyses during the analytical session. Chemical match between standard and unknown is required to minimize instrumental mass fractionation in SIMS analyses, therefore, reference calcite LAS-20 was used for evaluation of U/Ca in our sample. The reference values for U/Ca in LAS-20 were adopted from ICP-MS data reported in Table 1 of Sano et al. (2005). Twenty-five spot analyses yielded standard deviation (1 s.d.) of 23.5%, which was reduced to 9.0% after the removal of three outlier data, where uranium contents were lower than the average value by factors of two and ten (see appendix). No correlation between backscattered

electron intensities collected with scanning electron microscopy and U/Ca SIMS data was evaluated. Our reproducibility value (1 s.d. = 9.0%) is consistent with that found in the literature on LAS-20 data collected by ICP-MS, LA-ICP-MS, and Nano-SIMS; where 1σ = 6.2%, 9.8%, and 13.4% respectively (Sano et al., 2005). This suggests that U-depleted regions were not included into the data of Sano et al. (2005), supporting our removal of three outliers, which allowed us to reduce 1s.d. from 23.5 to 9.0%.

3.4 Geochemical Simulations

Two models GEM (Watson, 2004) and UUKM (Thien et al., 2014) were applied to explain uranium partition data, which cannot be modeled using thermodynamics only. The above mentioned models take into account deviation of trace element concentration from equilibrium. The GEM – or, as it is referred to by Thien et al. (2014), Surface (growth) Entrapment Model – accounts for the distribution of trace elements upon incorporation into the crystal lattice once it has been buried beneath the surface. The GEM assumes crystal growth from uniform and infinite reservoir. The UUKM is a unified model which incorporates both the GEM and Surface Reaction Kinetics Model (SRKM) (DePaolo, 2011). Moreover, the UUKM predicts changes in the composition of fluid and speciation throughout the course of an experiment. The SRKM model is based on the dynamics of precipitation-dissolution reactions at the crystal surface.

3.4.1 Simulation using the growth entrapment model (GEM)

Simulations were conducted using a new version of the GEM code (GEM2) running with QB64. The model presented here is based upon the work of Watson and co-workers (Watson, 1996; Watson, 2004; Watson and Liang, 1995) and the successful use

of the model (Stoll et al., 2002; Gaetani and Cohen, 2006; Tang et al., 2008a, Tang et al., 2008b; Gabitov et al., 2008; Gabitov et al., 2014b). The model can be described by the following relationship:

$$C(x) = C_{eq} \cdot F^{\exp(x/l)} \quad (3.1)$$

where $C(x)$ is the concentration of uranium in the crystal at some distance x from the surface, C_{eq} is the concentration reflecting the partition equilibrium between the growth medium and the crystal lattice, F is the surface enrichment factor, and l (0.5 nm) is the half-thickness of the enriched surface layer. The surface enrichment factor was calculated using the following equation:

$$F = (C_s / C_{eq}) = (K_s / K_{eq}) \quad (3.2)$$

where C_s is the concentration of uranium in the surface layer of calcite, K_s is the partition coefficient between surface layer and fluid, i.e. the U/Ca ratio at the surface of the crystal divided by the U/Ca ratio found in the fluid, K_{eq} is the equilibrium partition coefficient of uranium which is equal to the U/Ca ratio at equilibrium in the lattice (by considering an aqueous solid-solution between calcite and rutherfordine) divided by the U/Ca ratio of the fluid. The definition of K_{eq} we considered is:

$$K_{eq} = \frac{\left(x_{Rutherfordine} / x_{Calcite}\right)}{\left(a(U^{6+}) / a(Ca^{2+})\right)} \quad (3.3)$$

where x are solid molar fractions, and a are the aqueous activities. In the consideration of experimental conditions (i.e. fluid composition, ORP, pH, temperature), the aqueous concentration of Ca^{2+} is nearly equal to the total dissolved Ca; the aqueous concentration of all the U^{6+} species is nearly equal to the total concentration of dissolved uranium. It is therefore more convenient to use total dissolved concentrations in Ca and U.

3.4.2 Simulation using the unified uptake kinetics model (UUKM)

Additional effort was undertaken by running simulations using the UUKM. This model is combined with the GEM-Selektor v.3 geochemical modeling package (Wagner et al., 2012 and Kulik et al., 2013). The UUKM consists in the following equation:

$$K = \frac{F \cdot K_{eq}}{1 + \frac{D}{D+V} \cdot (F-1)} \tag{3.4}$$

This model reports that K varies between 2 limits, as a function of the growth rate: K_{eq}, and $F \cdot K_{eq}$ which corresponds to the composition of the surface layer, controlled by sorption mechanisms. Co-precipitation experiments carried out at larger growth rate range are necessary for robust evaluation of K_{eq} and F. The surface diffusivity parameter D can be fitted if no relevant experimental data is available. The linear growth rate (i.e. extension rate of individual crystal), V, was recalculated at each time-step by using a kinetic equation modified from Wolthers et al. (2012). More explanations about this model and its implementation in GEM-Selektor v.3 are provided in Thien et al. (2014).

The GEM-Selektor v.3 calculates the activities of the different aqueous species and complexes, and mineral phases, at each calculation step. The chemical thermodynamic system was set up for B, Ba, C, Ca, Cl, H, Li, Mg, N, Na, O, Sr, charge, assuming the overall charge neutrality. The list of components, species and phases used in the calculations and their corresponding thermodynamic data come from the Nagra-PSI data base (Hummel et al., 2002). Aqueous activity coefficients calculations were done by using the extended Debye-Hückel equation with the common ion size parameter of 0.372 nm. The solid-solution between rutherfordine and calcite was added in the database. Details about solid solutions and their implementation in GEM-Selektor v.3 are

given in Kulik et al. (2010) and Wagner et al. (2012). The interaction parameter (i.e. non-ideality) was adjusted in order to fit with experimental data.

3.5 Results

3.5.1 Uranium and calcium composition of the fluids

The following fluid U/Ca relationship with time of experiment (t) was established:

$$U/Ca\ (mmol/mol) = 3.96 \cdot 10^{-5} \cdot t^2 - 1.83 \cdot 10^{-4} \cdot t + 8.20 \cdot 10^{-1},\ R^2 = 0.97 \quad (3.5)$$

The initial fluid has low DIC and CO_3^{2-}, which increased to an unknown value before the onset of crystallization. Further, DIC and CO_3^{2-} increased by 13 and 31 % between 36 and 150 days after precipitation started (Table 3.1).

3.5.2 SIMS data

SIMS analyses identified the crystal zones marked with REE, in which the appearance corresponds to the sequence of REE addition to the fluid (see Fig. 1a in Gabitov et al., 2014b). The growth rates were determined as the width of each zone (Δx) in each SIMS profile divided by the time between REE spikes (Δt). Determined V values showed that crystals grew fast in their interior slowing down toward the edges, i.e. V decreased from 0.1 to 0.01 nm/s in the Sm-La and Tb-Pr zones, respectively (Table 3.2). Scattered U/Ca ratios increase from the edge toward the center of slow (run DC-1) and fast growing (run DC-3) calcite crystals. The variability of the U/Ca ratios in mmol/mol can be seen in Table 3.3. The SIMS analysis for the crystals was performed as profiles where the sampling distance, (L) in μm, ranges from 15 to 1729 μm as a function of the sampling distance from the edge of the crystal (Table 3.3). Topography of individual

crystals and standard grains was measured with interference microscope (PHASE SHIFT MicroXAM Surface Mapping Microscope Crystal). The results suggest that observed U/Ca trend in calcite samples is not an analytical artifact - i.e., observed U/Ca is not the result of <1 μm relief between center and edge of the crystals.

Table 3.2 Uranium partitioning data

REE	t (days)	V (nm/s)	V error	U/Ca calcite (mmol/mol)	s.e.	U/Ca fluid (mmol/mol)	s.e.	K^U	s.e.
Slow growth run DC-1, profile 1									
Tb-Pr	86-129	0.011	0.001	0.0337	0.0024	1.258	0.358	0.0268	0.0079
Nd-Tb	36-86	0.055	0.008	0.0381	0.0020	0.956	0.232	0.0398	0.0099
La-Nd	24-36	0.143	0.031	0.0466	0.0022	0.850	0.026	0.0549	0.0031
Sm-La	0-24	0.121	0.011	0.0503	0.0026	0.823	0.018	0.0611	0.0034
Slow growth run DC-1, profile 2									
Nd-Tb	36-86	0.040	0.004	0.0378	0.0193	0.956	0.232	0.0395	0.0098
La-Nd	24-36	0.089	0.006	0.0367	0.0038	0.850	0.026	0.0431	0.0047
Sm-La	0-24	0.086	0.010	0.0445	0.0055	0.823	0.018	0.0540	0.0067
Fast growth run DC-3									
Sm	0	≥1.8	n/a	0.0509	0.0053	1.024	0.209	0.0497	0.0114

Growth rate data are from Gabitov et al. (2014) (Table 2: slow growth run DC-1, Crystal-1, profile 4; slow growth run DC-1, Crystal-1, profile 5; Fast growth run DC-3, Cr1).

U/Ca in calcite is the average of a few spot analyses in particular REE spiked zones; s.e. (1σ) is the standard deviation of multiple spots divided by the square root of the number of spots (n) in each REE spiked zone. n varies from 3 to 6 in all REE-spiked zones except Tb-Pr zone, where n=1

In fast precipitation runs most of the growth occurred before the addition of 1st spike (Sm) therefore average U/Ca between initial fluid and Sm addition is considered in the run DC-3.

Error for growth rate is estimated as s.e. between two V data from the opposite sides of the crystal.

Table 3.3 SIMS analytical profiles of U/Ca

L (μm)	U/Ca (mmol/mol)	s.e.	L (μm)	U/Ca (mmol/mol)	s.e.
SIMS profile-1*			SIMS profile-2#		
65	0.0308	0.0023	15	0.0419	0.0021
94	0.0319	0.0016	55	0.0351	0.0025
130	0.0495	0.0032	95	0.0379	0.0025
174	0.0367	0.0017	155	0.0371	0.0024
219	0.0313	0.0014	215	0.0374	0.0019
264	0.036	0.0019	275	0.0389	0.0020
309	0.0371	0.0019	335	0.0416	0.0032
353	0.0432	0.0032	395	0.0369	0.0025
398	0.0399	0.0035	455	0.0551	0.0028
443	0.0408	0.0016	945	0.0518	0.0033
493	0.0599	0.0031	1005	0.0388	0.0026
537	0.0561	0.0025	1065	0.0443	0.0017
591	0.0405	0.0016	1128	0.0260	0.0018
1140	0.0495	0.0032	1189	0.0471	0.0022
1183	0.0541	0.0019	1239	0.0376	0.0015
1225	0.0467	0.0025	1284	0.0396	0.0023
1267	0.0451	0.0017			
1310	0.048	0.0021			
1352	0.0435	0.0023			
1395	0.0507	0.0031			
1437	0.0486	0.0022			
1480	0.0456	0.0026			
1522	0.0388	0.0019			
1564	0.0352	0.0019			
1607	0.0285	0.0021			
1649	0.0257	0.0017			
1689	0.0449	0.0032			
1729	0.0385	0.0016			

(*,#) – Growth rate data are from Gabitov et al. (2014) (DC-1 Crystal-1 profile-4 and profile-5 respectively). SIMS analyses were performed as profiles between the edges of the crystals. For example, distance L of 65 and 1729 μm corresponds to the opposite edges of the crystal, i.e. start and end of analytical profile. s.e. of U/Ca is the standard error at 1σ level which consists of the single spot s.e. and s.e. from multiple analyses on LAS-20 reference material. s.e. of V is the standard error calculated from the comparison of growth rates in the opposite sides of the crystal of particular REE-spiked zone.

3.5.3 Uranium partitioning data

The U/Ca calcite values show that as time increases, the incorporation of uranium into calcite, in mmol/mol, decreases conversely U/Ca in the fluid increases with time (Table 3.2). Table 3.2 shows an elevated growth rate (V) during the first 36 days of growth for both slow growth profiles. The partition coefficient of uranium between calcite and fluid was calculated as $K^U = (U/Ca)_{calcite}/(U/Ca)_{fluid}$, where $(U/Ca)_{calcite}$ is defined as the averaged SIMS data from particular REE-spiked zones within the calcite. The uncertainty in $(U/Ca)_{calcite}$ was calculated as the standard error (1 s.e.) of the data from individual REE-spiked zone (Figure 3.1). The error for growth rate is estimated as s.e. between V data from opposite sides of the crystal (Tables 3.2 and 3.3) (Figure 3.1). In the fast precipitation runs, the data for each crystal was averaged as most of the crystal growth occurred before the addition of the first spike. K^U was determined from the average U/Ca between the initial fluid and when the Sm spike was added.

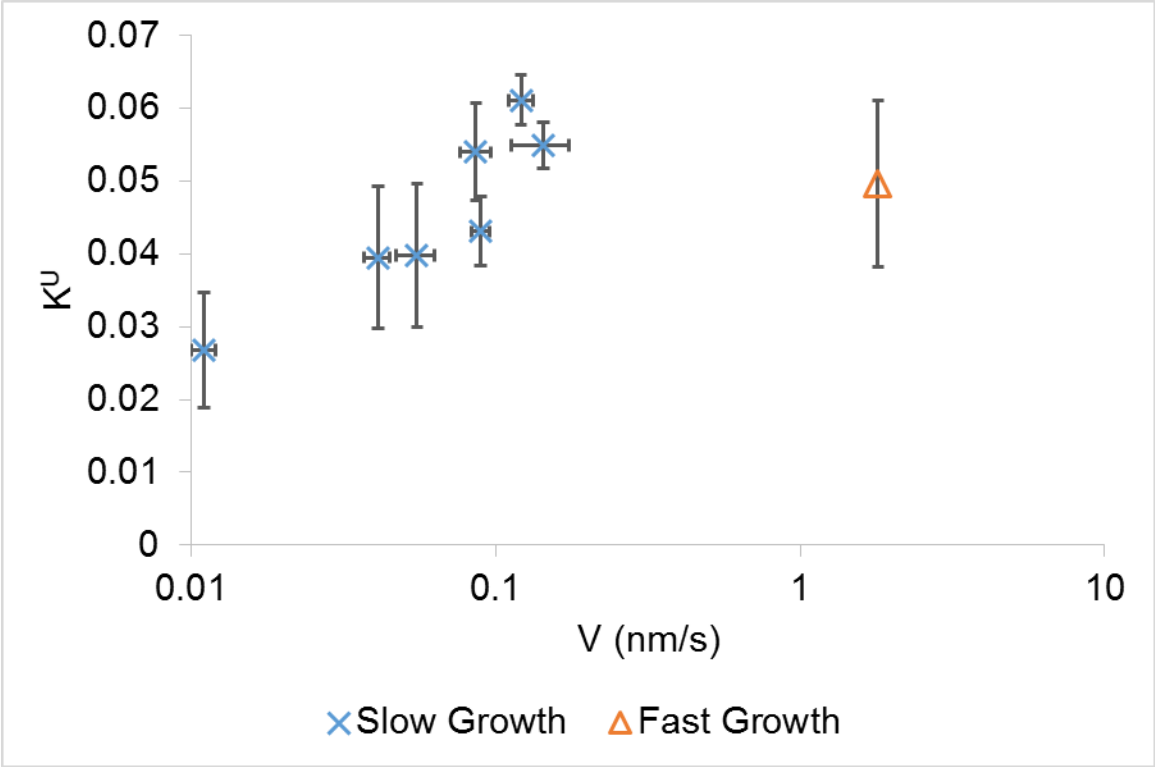

Figure 3.1 Fractionation coefficient of U in calcite as a function of growth rate, V (nm/s)

This graph is a plot of the values presented in Table 3 for Slow growth run DC-1, profile 1 and 2 and Fast growth run DC-3. The growth rate data are from Gabitov et al. (2014).

3.5.4 Modeling

By using growth entrapment modeling, the experimentally measured values of K as a function of V (Figure 3.2) implies an average value of K_{eq} of 0.02. This means that a small amount of uranium is up-taken by calcium carbonates at equilibrium. Obtaining this result with GEM Selektor code demands to use an interaction parameter of 1000 J/mol for the aqueous solid solution between calcite and rutherfordine.

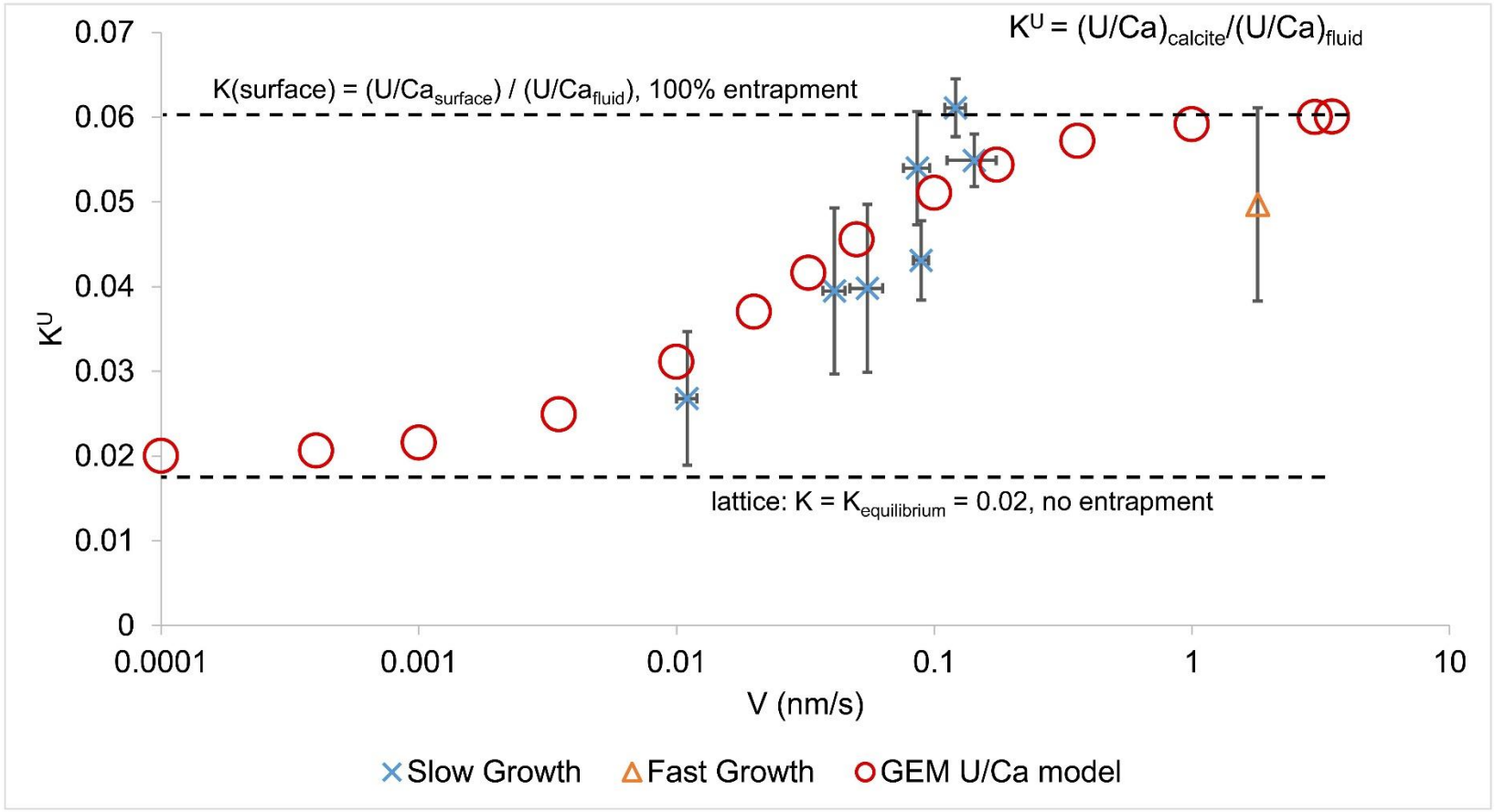

Figure 3.2 Fractionation coefficient of U in calcite as a function of growth rate, V (nm/s)

This graph presents the simulated data which was produced using the GEM software package. The growth rate data from Gabitov et al. (2014) is also plotted on the graph to show that the synthetically produced calcite grew at near 100% entrapment.

Based on the equations outlined above, *F* was found to be 3. The numerical simulation of the growth rate of calcite with incorporated uranium can be seen in Figure 2. In order to fit experimental data, the diffusivity in the near-surface (D_s) region of the crystals was adjusted to 0.01 nm^2/s. The value of obtained D_s is much higher than the diffusivity in the crystal lattice (D_l) which was assumed to be 10^{-18} nm^2/s based on the values used in previous work (i.e. Gabitov et al., 2014a) due to the lack of experimental data for U diffusion in calcite. To confirm that the value selected for D_l does not affect the simulation results as far as $D_l << D_s$, simulations were run using a D_l of 10^{-44} nm^2/s which affects the K^U values by 0.001% which is which is far below the minimum K_U error for SIMS analytical precision (5.6%, see Table 3.2).

The UUKM input parameters were nearly identical to those used in GEM: K_{eq}=0.02 and F=3. D=0.017 nm/s. This model provides the composition of the mineral as a function of the time (Figure 3.3). It is important to note that when using the UUKM combined with the GEM-Selektor v.3, the uranium speciation is nearly constant in that only two species appear (i.e. $CaUO_2(CO_3)_3^{2-}$ - 53% on average and $UO_2(CO_3)_3^{4-}$ - 45% on average).

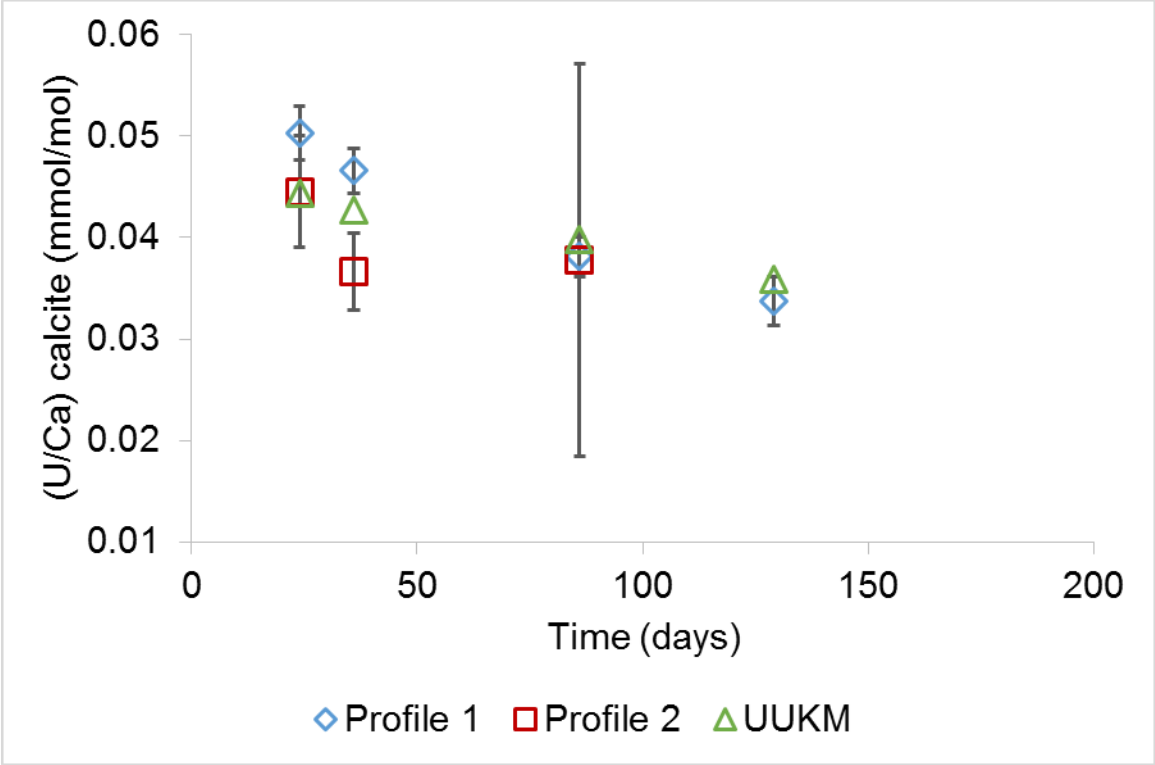

Figure 3.3 The U/Ca ratio in calcite (mmol/mol) as a function of time

This graph presents the modeling results of UUKM in addition to the values presented in Table 3 for Slow growth run DC-1, profile 1 and 2 and Fast growth run DC-3.

3.6 Discussion

The information provided by Figure 1 suggests that 100% entrapment occurs at V>0.1 nm/s at K^U of about 0.06. This is inconsistent with the data of Kitano and Omoori (1971) and Meece and Benninger (1993) who observed a maximum K^U value of 0.2 at similar pH. Kitano and Omoori (1971) used a different definition of partition coefficient ($K^{UO^{2+}}$). Only UO_2^{2+} was considered in their calculations; whereas in our study we considered the total dissolved uranium concentration. The fact that UO_2^{2+} is not the major uranium specie when pH>6 (Djogić et al., 1986), mathematically implies that $K^{UO^{2+}}$ obtained by Kitano and Omoori (1971) are higher than those obtained in this study. On

the contrary, Meece and Benninger (1993) considered that same definition as in this study and consequently could not miss any specie or complex during measurement, because they measured radioactive activity. However, the pH range of Meece and Benninger (1993) experiments lie between 8.25 and 9.00, which is different from our pH values (7.96–8.17). This could explain the lower K^U in our work due to sensitivity of the fraction of $UO_2(CO_3)_3^{4-}$ at pH values around 8 (Djogić et al., 1986).

Both models GEM and UUKM are able to reproduce quantitatively the uranium incorporation in calcite we measured (Figures 3.2 and 3.3). The GEM assumes uniform reservoir composition, which is not the case for our experiments, and therefore K^U instead of U/Ca was used for fitting with GEM. In order to achieve the desired fit while using the GEM, a multiplier parameter (m) was used. This multiplier parameter was set to infinity which implies that diffusivity is equal to D_s at the distance much greater than thickness of near-surface layer. The UUKM accounts for change of U/Ca in fluid providing the absolute composition of the calcite. U/Ca for REE-spiked zones of calcite calculated with UUKM match U/Ca determined experimentally (Figure 3.3) implying the ability of growth entrapment phenomena explains U incorporation into calcite from finite reservoir. High surface enrichment factors (F>1) in calcite is sufficient with F values proposed for Sr, Ba, and Se (Watson, 2004; Gabitov and Watson, 2006; Thien et al., 2014). However, enrichment for uranium could be underestimated, thus more experimental data at growth rates slower than in our experiments are necessary to determine K_{eq}^U and F values.

We calculated partition coefficients using K^U-CO_3^{2-} calibration for foraminifera from Table 2 in Keul et al. (2013). The values of CO_3^{2-} were calculated as averages

between three sub-samples collected during addition of Nd and Tb spikes and final fluid (200 and 239 μmol/kg for Nd-Tb and Tb-final respectively). The obtained K^U values decrease from 0.129 to 0.108 with increasing of CO_3^{2-} from 200 to 239 μmol/kg, which is consistent with our data where K^U decreases from 0.040 to 0.027 (see Table 3.2, Nd-Tb and Tb-Pr spiked zones). However, absolute values of K^U are different by a factor of three. The low K^U in our work relative to foraminifera (Keul et al., 2013) and inorganically precipitated calcite (Meece and Benninger, 1983) could be explained by different chemistry of our fluids and higher U content (10^{-5} mol/l) compared to that of seawater where U content is ~$1.5 \cdot 10^{-8}$ mol/l.

3.7 Conclusions

It was shown for the first time that uranium incorporation in calcite increases with the growth rate of individual crystals. The phenomenon can be explained with the concept of growth entrapment proposed by Watson (2004). The discrepancies with previously published studies had been investigated, but cannot be quantitatively explained. It would require more experimental effort, especially on aqueous uranium species measurements. It was also demonstrated that both models, GEM and UUKM, fit the experimental data assuming similar equilibrium partition coefficient of uranium, its diffusivity in the near-surface region of calcite, and identical surface enrichment factor. This study provided an opportunity to show that the UUKM coupled with GEM-Selektor is able to predict trace element concentration in growing minerals, when U/Ca in solution increased by the factor of two during experiment.

CHAPTER IV

Mg/Ca RATIOS IN SYNTHETIC LOW-MAGNESIUM CALCITE: AN EXPERIMENTAL INVESTIGATION

4.1 Abstract

The intent of the work presented is to determine the effect which the Mg/Ca ratio in fluid has on the Mg partition coefficient (K^{Mg}) between synthetically precipitated low-magnesium calcite and solution. In nature, planktonic foraminifera produce low-magnesium calcite with distinct Mg/Ca that is typically found to be within the range of ~1.6 to ~10.2 mmol/mol. The intent of this research is to replicate the range of Mg/Ca found in foraminifera by conducting experiments where low-magnesium calcite is grown inorganically under controlled fluid chemistry, growth rate, and temperature. Synthetic low-Mg calcite is precipitated by mixing NaCl, $NaHCO_3$, $MgCl_2 \cdot 6H_2O$, and $CaCl_2 \cdot 2H_2O$ chemicals. In order to vary the Mg/Ca ratio, the magnesium and calcium molar concentrations were varied but the sum of the concentrations was kept equal to the concentration of $NaHCO_3$. To achieve precipitation of calcium carbonate within a reasonable time frame, it was necessary to significantly elevate the concentrations of chemical additives above what is normally found in natural seawater. Initially, Na_2CO_3 was used as a titrate and high pH (up to 9.4-10.8) was achieved in the growth media; pH varied between 6 and 7 when $NaHCO_3$ was injected. Optical microscopy and powdered X-ray diffraction analysis showed that the use of Na_2CO_3 in experiments precipitated

predominately aragonite with spar-like crystals, whereas use of $NaHCO_3$ yielded calcite with rhombohedral crystals. Though for experiments where Ca concentration was similar to seawater Ca (i.e. series 10), the carbonate source ($NaHCO_3$ or Na_2CO_3) was found to have no effect on $CaCO_3$ polymorph, and calcite was the only precipitated mineral. Calcites precipitated in those experiments were analyzed using Inductively Coupled Plasma Optical Emission Spectrometry (ICP-OES) for Mg and Ca. Fluids collected during individual runs were measured with Line-Source Atomic Absorption Spectroscopy (LS-AAS) to determine Mg/Ca ratio throughout the duration of the experiments. Though a constant $Mg/Ca_{(Fluid)}$ was not achieved for all experiments, it was possible to determine Mg partition coefficient between calcite and fluid ($0.011 \leq K^{Mg} \leq 0.047$) by using averaged $Mg/Ca_{(Fluid)}$ and Mg/Ca in the precipitated calcite. Results showed that K^{Mg} increases with decreasing of fluid Mg/Ca when $Mg/Ca_{(Fluid)} > 0.4$ mol/mol; no systematic correlation of K^{Mg} with $Mg/Ca_{(Fluid)}$ was found when $0.03 < Mg/Ca_{(Fluid)} > 0.4$ mol/mol. No effect of Mg and Ca concentrations on K^{Mg} was observed.

4.2 Introduction

Understanding the factors which control Mg incorporation into calcite is of significant interest to the geoscientific community, as Mg/Ca of foraminifera shells are being used to study temperature variations in the oceans over much of the geologic past (i.e. Phanerozoic). The ability of calcite to accommodate trace and minor elements into its crystalline structure has been a topic of interest for inorganic precipitation studies. These studies demonstrate that Mg partition coefficient (K^{Mg}) is temperature dependent (Katz, 1973; Füchtbauer and Hardie, 1976; Burton and Walter, 1987; Howson et al., 1987; Mucci, 1987; Oomori et al., 1987; Huang and Fairchild, 2001). There have also

been a number of studies which propose other parameters which could influence K^{Mg} such as salinity (Mucci 1983; Zhong and Mucci 1989), pH (Oomori et al., 1987; Burton and Walter, 1991; Hartley and Mucci, 1996), calcite growth rate (Given and Wilkinson, 1985a; Given and Wilkinson, 1985b; Saulnier et al. 2012; Mavromatis et al. 2013; Gabitov et al. 2014), Mg/Ca ratio of the solution (Devery and Ehlmann, 1981; Mucci and Morse, 1983; Busenberg and Plummer, 1989; Mavromatis et al. 2013), or possibly a combination of calcite growth rate and the Mg/Ca ratio of the solution (Gabitov et al., 2014). For example, Mavromatis et al. (2013), assessed the calcite growth rate by conducting a series of experiments where pH was maintained constant by bubbling pure CO_2 gas into the precipitation medium and found that pH does not have a direct effect on K^{Mg}. It is however, known that the pH of fluids has an effect on growth rate (i.e. fluids with low pH cause carbonate dissolution) which in-turn has an effect on K^{Mg}. The findings of Mavromatis et al. (2013) and Gabitov et al. (2014) demonstrate that growth rate is responsible for controlling Mg partitioning. Though the two studies found opposite relationships between K^{Mg} and growth rate, it was explained by Gabitov et al. (2014) that this could possibly be due to differences of Mg/Ca in the fluid which in-turn would cause a change in the Mg incorporation mechanism.

It is known that the oceanic Mg/Ca ratio is not constant with respect to geologic time and has in-fact varied from ~1 to 5.2 mol/mol between present day and the Cretaceous (Sandberg, 1983; Wilkinson and Algeo, 1989; Hardie, 1996; Horita et al., 1996; Stanley and Hardie, 1999; Zimmermann et al., 2000; Lowenstein et al., 2001; Horita et al., 2002; Dickson, 2002; Lowenstein et al., 2003; Coggon et al., 2010; Hasiuk and Lohmann, 2010; Broecker and Yu, 2011). The cause or causes for fluctuation of

seawater Mg/Ca is not fully understood, but it is thought to be controlled by various parameters, including runoff (Demicco et al., 2005), the rate of oceanic crust production (Spencer and Hardie, 1990; Hardie, 1996), and the rate of dolomite formation (Holland and Zimmermann, 2000).

There have been attempts made to study variations in oceanic Mg/Ca over the geologic past using coccolithophores. Such studies investigate the Mg incorporation into individual coccolith tests as a temperature proxy are somewhat limited, this may possibly be due to the difficulty of working with such small specimens (~3-15 μm) (Schmidt et al., 2006). However, some workers have been able to analyze individual coccoliths by utilizing Secondary Ion Mass Spectrometry (SIMS) (Stoll et al., 2007; Prentice et al., 2014). By comparison, the analysis of Mg/Ca in foraminiferal calcite is far more studied than Mg/Ca in coccolith calcite. Studies have demonstrated that temperature is the primary control on Mg/Ca in the tests of foraminifera (Nürnberg et al., 1996; Lea et al., 1999; Mashiotta et al., 1999; Rosenthal et al., 2000). Recent studies suggest that salinity also influences Mg/Ca in foraminifera (Lea et al., 1999; Ferguson et al., 2008; Mathien-Blard and Bassinot, 2009; Hönisch et al., 2013), but in a lesser capacity than temperature for surface marine waters.

The Mg/Ca ratio of oceanic waters can be inferred by studying Mg/Ca preserved in fossilized marine organisms (e.g. foraminifera, coccoliths, echinoids, corals, algae) (Dickson, 2002; Ries, 2004; Stanley et al., 2005). It is known that the Mg/Ca ratio in planktonic foraminifera is much lower than what is expected based on the Mg concentration in typical seawaters (Bentov and Erez, 2006). It has been postulated that the cause for depressed Mg in foraminiferal calcite is biological/physiological factors

which selectively occlude Mg at the site of calcification (Blackmon and Todd, 1959; Bentov and Erez, 2006). The experiments conducted by Gabitov et al. (2014) yielded Mg/Ca ratios in synthetic calcite similar to those observed in planktonic foraminifera, their fluid Mg/Ca was not controlled and changed together with crystal growth rate in individual experiments. Though there are some dissimilarities in regards to experimental design between the two works (i.e. Gabitov et al., 2014 and present study), in the present study, experiments were designed to keep Mg/Ca near-constant throughout the duration of individual experiments and each experiment was conducted with a different Mg/Ca in fluid.

4.3 Materials and Methods

The method of calcite precipitation utilized in this study involved the continuous addition of $CaCl_2$, $MgCl_2$, and $NaHCO_3$ (Na_2CO_3) titrates into a NaCl solution. These methods were modified from techniques described in several previous works (e.g. Tesoriero and Pankow, 1996; Mavromatis et al., 2013). Numerous trial experiments were conducted prior to achieving the desired experimental design used to conduct the final experiments (series 8, 9, and 10). The purpose of these trial experiments were to determine a titrate chemistry which would yield the largest possible crystals, optimal flow rate, and the design, fabrication, and testing of custom cartridge links. The development of titrate chemistry used in the final experiments is not straightforward. Different proportions of $MgCl_2 \cdot 6H_2O$ and $CaCl_2 \cdot 2H_2O$ to Na_2CO_3 were attempted as well as Na_2CO_3 to NaCl, varying NaCl concentrations, and the substitution of $NaHCO_3$ for Na_2CO_3 (Table 4.1). For one experiment, high-purity CO_2 was bubbled into the reaction vessel (Table 4.1). The variation of titrate chemistry was conducted in order to

determine the necessary concentrations which would yield the largest crystal size possible while also maintaining a near-constant salinity.

Table 4.1 Concentration of salts: Trial experiment series 1 through 7

Experiment	Concentration of salts (mol/l)						Calculated Aqueous Mg/Ca (mol/mol)	Calculated Aqueous Mg/Ca* (mmol/mol)
	NaCl	$NaHCO_3$	Na_2CO_3	$NaH_2PO_4 \cdot H_2O$	$MgCl_2 \cdot 6H_2O$	$CaCl_2 \cdot 2H_2O$		
1A	0.600	—	0.300	—	9.05E-03	2.91E-01	0.031	0.778
1B	0.600	—	0.300	—	9.01E-02	2.10E-01	0.429	10.716
1C	0.600	0.300	—	—	9.01E-02	2.10E-01	0.429	10.716
2A	0.200	—	0.100	—	3.02E-03	9.70E-02	0.031	0.779
2B	0.200	—	0.100	—	3.00E-02	7.01E-02	0.428	10.709
2C	0.200	0.100	—	—	3.00E-02	7.01E-02	0.428	10.709
3A	0.600	—	0.300	—	9.01E-02	2.10E-01	0.429	10.716
3B	0.600	—	0.300	—	9.05E-03	2.91E-01	0.031	0.778
3C	0.600	0.300	—	—	9.01E-02	2.10E-01	0.429	10.716
3D	0.600	0.300	—	—	9.05E-03	2.91E-01	0.031	0.778
4A	0.600	—	0.040	—	1.00E-02	3.00E-02	0.333	8.336
4B	0.600	—	0.040	2.84E-04	1.00E-02	3.00E-02	0.333	8.336
5A	0.030	—	0.030	—	6.00E-03	2.40E-02	0.250	6.250
5B	0.003	—	0.003	—	6.00E-04	2.40E-03	0.250	6.250
5C	0.300	—	0.300	—	6.00E-02	2.40E-01	0.250	6.250
6A	0.600	—	0.040	—	1.00E-02	3.00E-02	0.333	8.336
6B	0.600	—	0.040	2.84E-04	1.00E-02	3.00E-02	0.333	8.336
7A	0.600	—	0.010	—	2.50E-03	7.50E-03	0.333	8.333
7B†	0.600	—	0.010	—	2.50E-03	7.50E-03	0.333	8.333
7C	0.600	—	0.010	2.04E-03	2.50E-03	7.50E-03	0.333	8.333

*The values presented in this column were calculated multiplying the Mg/Ca molar ratio by 0.025 then converting to mmol by multiplying by 1000.

† High-purity CO2 was bubbled into the reaction vessel throughout the duration of the experiment.

For all experiments conducted, titrate fluids were delivered to a reaction vessel at a rate of approximately 0.14 ml/min using a programmable multi-channel peristaltic pump and 1.75 mm inner-diameter (i-d) tubing (Fig. 4.1). The reason for fabricating custom cartridge links is because cartridge links are expensive and supply companies do not carry the i-d tubing size which was needed for our peristaltic pump. The cartridge links were created using two ≤ 5 mm lengths of 7 mm outer diameter tubing that were cut and affixed to a length of 1.75 mm i-d tubing, approximately 150 mm apart, using epoxy.

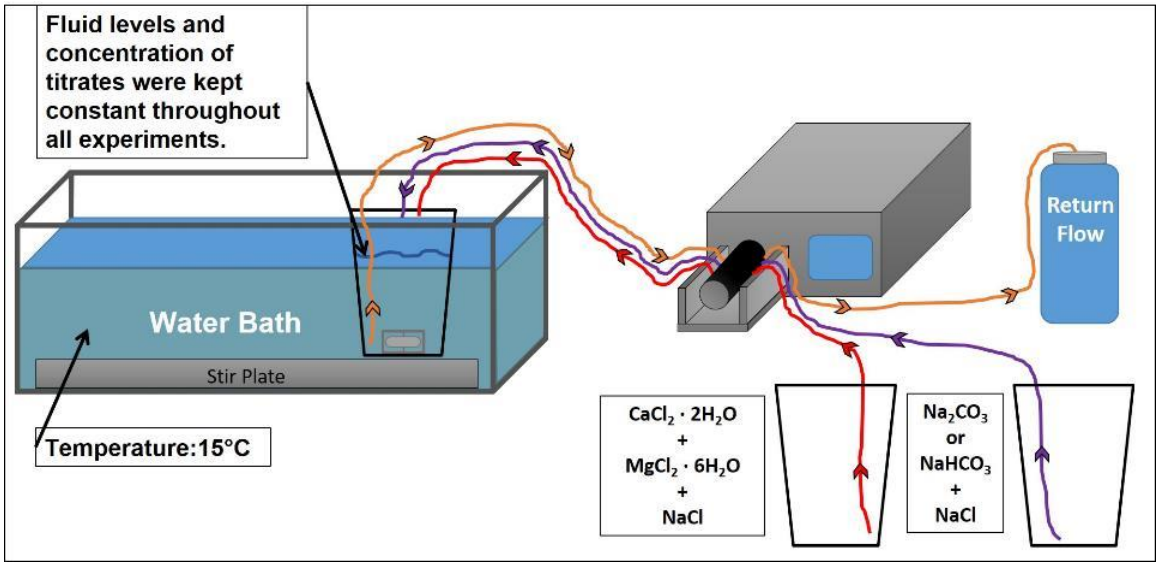

Figure 4.1 Illustration depicting the experimental set-up for experiments conducted in series 8, 9, and 10.

4.3.1 Experimental design

Results from the last three series of experiments (series 8, 9, and 10) will be discussed in greater detail later in the text. Series 8 and 9 consisted of six experiments each while series 10 consisted of two experiments. All experiments were conducted using

a continuous-pumping method by which titrates were pumped into a reaction vessel at a rate of 0.14 ml/min using a multi-channel peristaltic pump, then into a return-flow vessel also at rate of 0.14 ml/min. This was done to maintain near-constant fluid volume in the reaction vessel. The fluids in the reaction vessel were maintained at 15°C in a refrigerated water bath and continuously stirred at 150 rpm using a submersed stir plate and suspended magnetic stir bars (Fig. 4.1). The experiments were conducted at 15 °C as this is close to the average global sea surface temperature.

For series 8, three solutions were prepared for each experiment. Solution 1, in the reaction vessel (i.e. initial solution), was composed of a mixture of NaCl (99.9%), $MgCl_2 \cdot 6H_2O$ (99.8%), and $CaCl_2 \cdot 2H_2O$ (99.7%) chemical salts [values in parentheses denote chemical purity]. Solid Na_2CO_3 (99.8%) was added to solution 1 almost immediately before pumping was initiated for each of the experiments. All solutions were prepared using *Fisher Chemical* Certified ACS salts. The first step in preparing all solutions was to mix NaCl with reverse osmosis (RO) H_2O to achieve a concentration of 0.6 M. For each experiment, two titrate vessels were prepared using the NaCl solution described above. In titrate vessel 1, $MgCl_2 \cdot 6H_2O$ and $CaCl_2 \cdot 2H_2O$ salts were added to the NaCl solution. The mass of $MgCl_2 \cdot 6H_2O$ and $CaCl_2 \cdot 2H_2O$ salts added for each experiment varied depending on the desired Mg/Ca ratio of the fluid. Titrate vessel 2, was prepared by the addition of 19.0458 g of Na_2CO_3 to the NaCl solution. The mass of Na_2CO_3 added to titrate vessel 2 was the same for each of the four experiments. The molar concentration of Na_2CO_3 in titrate 1 was equal to the molar concentration of $MgCl_2 \cdot 6H_2O + CaCl_2 \cdot 2H_2O$ in titrate 2 in all experiments. The concentration of the salts present in the titrate

solutions for each experiments in series 8 are reported in Table 4.2. Fluid Mg/Ca varies from 0.51 to 20.18 (mmol/mol) between experiments in series 8.

Table 4.2 Concentration of salts: experiment series 8

Experiment	Concentration of salts in titrate solution (mol/l)				Calculated Mg/Ca Aqueous (mol/mol)	Calculated Aqueous Mg/Ca* (mmol/mol)
	NaCl	Na_2CO_3	$MgCl_2 \cdot 6H_2O$	$CaCl_2 \cdot 2H_2O$		
8A	0.600	0.300	0.134	0.166	0.807	20.181
8B	0.600	0.300	0.113	0.187	0.604	15.107
8C	0.600	0.300	0.050	0.250	0.200	5.000
8D	0.600	0.300	0.006	0.294	0.020	0.510
8E	0.600	0.300	0.023	0.277	0.083	2.076
8F	0.600	0.300	0.066	0.234	0.282	7.051

*The values presented in this column were calculated multiplying the Mg/Ca molar ratio by 0.025 then converting to mmol by multiplying by 1000.

For experiments in series 9, the chemistry of the solutions is similar to that used in series 8, though not identical. In series 9, $NaHCO_3$ (99.7%) was used instead of Na_2CO_3 in both the titrate solution and the initial solution, and 0.6 M NaCl was added only to the initial solution and to the titrate solution containing $NaHCO_3$. See Table 4.3 for information regarding the concentration of solutions. Fluid Mg/Ca varies from 0.51 to 20.18 (mmol/mol) between experiments in series 9.

Table 4.3 Concentration of salts: experiment series 9

Experiment	Concentration of salts in titrate solution (mol/l)				Calculated Mg/Ca Aqueous (mol/mol)	Calculated Aqueous Mg/Ca* (mmol/mol)
	NaCl	$NaHCO_3$	$MgCl_2 \cdot 6H_2O$	$CaCl_2 \cdot 2H_2O$		
9A	0.600	0.300	0.134	0.166	0.807	20.181
9B	0.600	0.300	0.113	0.187	0.604	15.107
9C	0.600	0.300	0.050	0.250	0.200	5.000
9D	0.600	0.300	0.006	0.294	0.020	0.510
9E	0.600	0.300	0.023	0.277	0.083	2.076
9F	0.600	0.300	0.066	0.234	0.282	7.051

*The values presented in this column were calculated multiplying the Mg/Ca molar ratio by 0.025 then converting to mmol by multiplying by 1000.

Experiments 10A and 10B were conducted using the same experimental setup used in series 8 and 9 but with different chemical concentrations and hence a lower salinity. Experiment 10A was conducted using $NaHCO_3$ as the carbonate source, while Na_2CO_3 was used as the carbonate source in experiment 10B. The concentration of the solutions used in experiments 10A and 10B are reported in Table 4.4. Fluid Mg/Ca for experiments in series 10 was 5 (mmol/mol).

Table 4.4 Concentration of salts: experiment series 10

Experiment	Concentration of salts in titrate solution (mol/l)				Calculated Mg/Ca Aqueous (mol/mol)	Calculated Aqueous Mg/Ca* (mmol/mol)
	NaCl	$NaHCO_3$ or Na_2CO_3	$MgCl_2 \cdot 6H_2O$	$CaCl_2 \cdot 2H_2O$		
10A	0.600	0.012	0.002	0.010	0.200	5.000
10B	0.600	0.012	0.002	0.010	0.200	5.000

*The values presented in this column were calculated multiplying the Mg/Ca molar ratio by 0.025 then converting to mmol by multiplying by 1000.
Sodium bicarbonate was used as the carbonate source for experiment 10A whereas sodium carbonate was used as the carbonate source for 10B.

Sub-samples were collected from the reaction vessel every 12-24 hours to measure pH, salinity, Mg, and Ca concentrations. The collection of sub-samples and all other fluids (i.e. return flow fluid and final fluid) was done using a 60 ml syringe and then filtered using a 0.45 μm Nylon Whatman syringe filter. All pH measurements were conducted using a Denver Instrument UB-10 UltraBASIC benchtop meter equipped with a Sartorius PY-P11 pH Combination Electrode. Salinity measurements were carried out using a HI 5521 bench top meter equipped with a HI 76312 4-ring platinum EC/TDS probe. After measurements were conducted all sub-samples were stored in a freezer at -20 °C to prevent spoiling of the samples. An aliquot of fluid from the return flow vessel was recovered approximately every two to three days and frozen to later determine the alkalinity of the fluids. Upon ending the experiments, an aliquot of the fluid from the reaction vessel was frozen to determine alkalinity.

4.4 Analytical Techniques

4.4.1 Atomic Absorption analysis of fluids

Fluid samples from all experiments in series 8, 9, and 10 were analyzed using a Shimadzu, AA-7000 Line-Source AAS. The LS-AAS was calibrated using 1000 ppm magnesium and calcium analytical standards (Fisher Scientific) as stock solutions. Six calibration standards were created for each element. The standards for calcium ranged from 0.5 ppm to 16 ppm, with the concentration of each successive standard being double the previous. The standards for magnesium ranged from 0.05 ppm to 1.6 ppm, with the concentration of each successive standard being double. Calibration curves showed that the actual concentrations, which were measured using LS-ASS were very close to the prepared concentration as the minimum R^2 value for the calibration curves is 0.993.

4.4.1.1 Container Preparation and Sample Dilution

All fluid samples, including calibration standards, were prepared for LS-AAS analysis in 50 ml polypropylene centrifuge tubes which were cleaned by the following means: 1) rinsing three times with 3-5 ml of 10% ACS grade HNO_3, 2) rinsing three times with 3-5 ml of 2% trace metal grade HNO_3, and 3) filling the tubes completely with Nano-pure H_2O, replacing the cap, vigorously shaking to remove any residual acid, and finally emptying the tubes and shook dry. Once cleaned, samples were prepared via dilution in the centrifuge tubes using 2% trace metal grade HNO_3.

4.4.2 Alkalinity Titrations

Alkalinity titrations were performed to determine the alkalinity at the beginning and end of each experiment in series 8, 9, and 10. Titrations were conducted using a 25 ml burette, 100 ml glass beakers, pH meter and electrode, magnetic stir plate and stir bars, disposable 10 ml volumetric pipets, phenolphthalein indicator, volumetric flasks, trace metal grade H_2SO_4, RO H_2O, and ACS grade Na_2CO_3.

2.62 g of H_2SO_4 was added to 1000 ml of RO H_2O in a volumetric flask (the procedure described herein was also conducted using 5.23 g of H_2SO_4 for those samples with a pH of 9.5 or higher). Three solutions of $7.76 \cdot 10^{-5}$ M Na_2CO_3 were prepared in 100 ml glass beakers. Four drops of phenolphthalein indicator were added to each of the solutions. One of the three beakers containing the Na_2CO_3 solution was placed on a magnetic stir plate which was positioned beneath the burette and a stir bar was placed in the beaker. Sulfuric acid was titrated into the Na_2CO_3 solution until the phenolphthalein indicator changed color from pink to clear. The volume of acid consumed to cause the color indicator to change was recorded and used to determine the molarity of the acid:

$$M_{H_2SO_4} = \frac{X}{V} \tag{4.1}$$

where M is the molarity of the H_2SO_4 acid, X is the moles of Na_2CO_3, and V is the volume in liters of H_2SO_4 consumed. The procedure described above for determining acid molarity was completed a total of three times and the average of the three values was taken to be the concentration of the H_2SO_4.

With the concentrations of the prepared volumes of H_2SO_4 known, fluid collected from the return flow vessel at the beginning of each experiment and final fluid collected at the end of each experiment in series 8, 9, and 10 underwent titration to determine the alkalinity of the fluid. Titrations were conducted by the addition of 30 ml of the desired sample to a 100 ml beaker using a disposable 10 ml volumetric pipette. A stir bar and pH electrode were also placed in the beaker prior to positioning it on the magnetic stir plate, beneath the burette. After the initial pH of the sample was recorded, the H_2SO_4 acid was titrated until the pH of the sample reached the HCO_3^- equivalence point where the change in pH per volume of titrant added is maximized, and generally will be found near pH 4.5 (Rounds, 2012). The volume of acid used to lower the pH to the desired level was recorded and used to calculate the alkalinity. The following equation was used to determine alkalinity:

$$Alk_o = \frac{B \times C_a \times 50000}{V_o} \tag{4.2}$$

where Alk_o is the alkalinity of the sample in (mg/l) of $CaCO_3$, B is the volume of the titrant needed to reach the HCO_3^- equivalence point (ml), C_a is the normality of the acid titrant (eq/l), 50,000 is a constant (mg $CaCO_3$/eq), and V_o is the initial volume of the sample (ml). The methods described above were performed in triplicate for each sample,

and the average of the three alkalinity values was taken to be the true value. The alkalinity values were converted from mg of $CaCO_3$/l to μmol/kg of H_2O so that the values would be compatible with the program CO2SYS, originally developed by Lewis and Wallace (1998) and updated by Pierrot et al. (2006).

4.4.3 ICP-OES analyses of solids and fluids

Solid samples collected from experiments which produced calcite precipitates (i.e. samples from each experiment in series 9 and 10) were sent to the University of Cambridge (UK), for elemental analysis. The samples were cleaned prior to shipment by rapid (5-10 s) rinsing the solids three times with RO H_2O, followed by three times with trace metal grade methanol, once using 10% ultra-high purity H_2O_2, then rinsed three more times using Nano-pure H_2O. The samples were shipped using 4 ml plastic vials which had been cleaned prior to the addition of the solid samples by soaking them in 10% ACS grade HNO_3 then 2% trace metal grace HNO_3 and were lastly rinsed with Nano-pure H_2O and dried at 40°C. The analyses were conducted using an Algilent 5100 ICP-OES to determine the abundance of magnesium and calcium in the solid precipitates.

4.4.4 X-ray Diffraction (XRD) analysis

Powdered X-ray diffraction (XRD) analyses were conducted for all solid samples collected from experiments in series 8, 9, and 10 to determine mineral composition. Analyses were carried out using a Rigaku Ultima III X-ray diffractometer. All data interpretations were conducted using MDI Jade 2010 software package at Mississippi State University Institute for Imaging and Analytical Technology (I^2AT). The XRD pattern for each sample was obtained using CuKα radiation with a wavelength of 1.54059

Å (at the recommendation of the I^2AT staff). Scan speed was set for 0.5 degrees per minute with a scan step of 0.02 degrees and an effective scan range of 20 – 40 degrees.

4.5 Results

4.5.1 Results of fluid pH, salinity, and saturation state

Graphical representations of the pH and salinity data collected as part of series 8, 9, and 10 can be seen in Figures 4.2 through 4.4 for pH and Figures 4.5 through 4.7 for salinity where the data has been plotted as X-Y scatter plots. Figure 4.2 shows the pH at the beginning of experiments 8A through 8F is between 7.5 and 8.5, and by 50 hours pH of all experiments had abruptly risen to between 9.5 and 10.5. The noted rise in pH followed by a "plateau of the values" cannot be explained by the onset of crystal nucleation, as precipitation of crystals for all experiments in series 8 was observed almost immediately after pumping was initiated at time zero. Between 50 and 75 hours, pH began to stabilize for most experiments demonstrating steady-state conditions. Figure 4.3 shows the pH at the beginning of experiments 9A through 9F is between 6 and 7. The onset of crystallization was observed approximately 24 hours into the experiments for series 9 and was at this time that pH began to stabilize for all experiments demonstrating steady-state conditions. Figure 4.4 shows the pH at the beginning of experiment 10A as being approximately 7.75 and 10B as being approximately 9.75. Precipitation of crystals was not observed until 75 hours into the experiments. After 100 hours, the pH of the fluids in experiments 10A and 10B began to stabilize demonstrating steady-state conditions. Additional information regarding salinity can be found in Table 4.5 where values have been reported as average values.

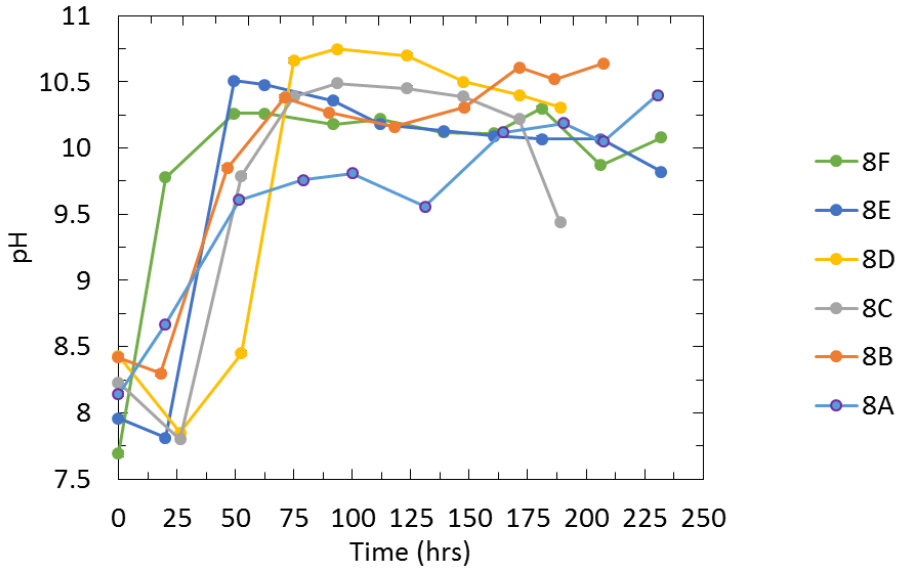

Figure 4.2 Graphical representation of pH plotted against time for experiments 8A through 8F.

Analytical uncertainty is ± 0.02 and is included in symbol size. Experiments in series 8 were carried out using Na_2CO_3 salts as the carbonate source. Precipitation of crystals for all experiments in series 8 was observed almost immediately after pumping was initiated at time zero.

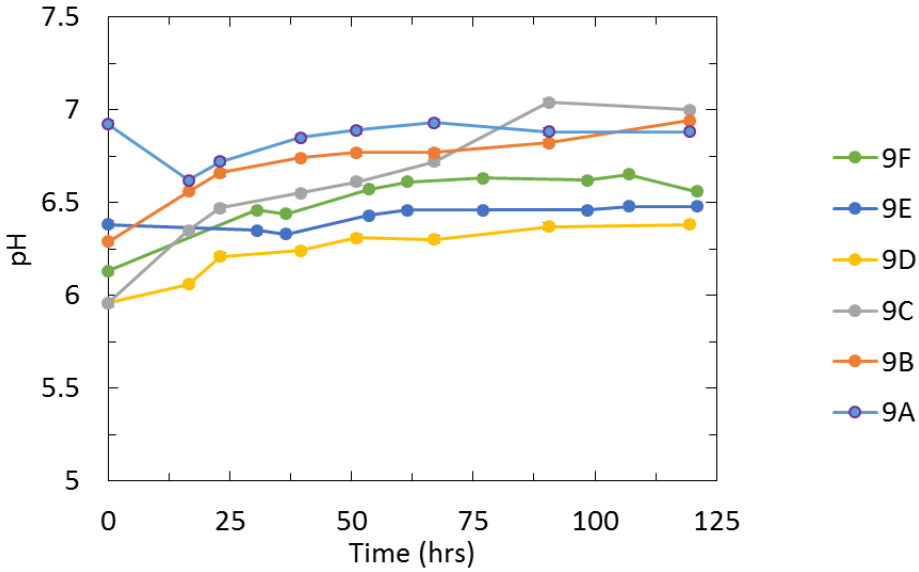

Figure 4.3 Graphical representation of pH plotted against time for experiments 9A through 9F.

Analytical uncertainty is ± 0.02 and is included in symbol size. Experiments in series 9 were carried out using $NaHCO_3$ salts as the carbonate source. The onset of crystallization was observed approximately 24 hours into the experiments for series 9.

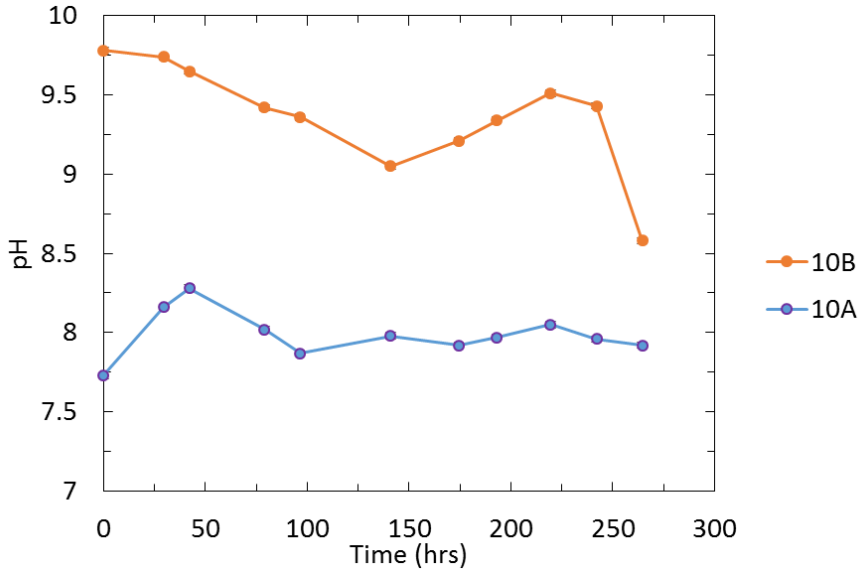

Figure 4.4 Graphical representation of pH plotted against time for experiments 10A and 10B.

Analytical uncertainty is ± 0.02 and is included in symbol size. Experiment 10A was carried out using $NaHCO_3$ as the carbonate souce whereas Na_2CO_3 was used in experiment 10B. Precipitation of crystals was not observed until 75 hours into the experiments.

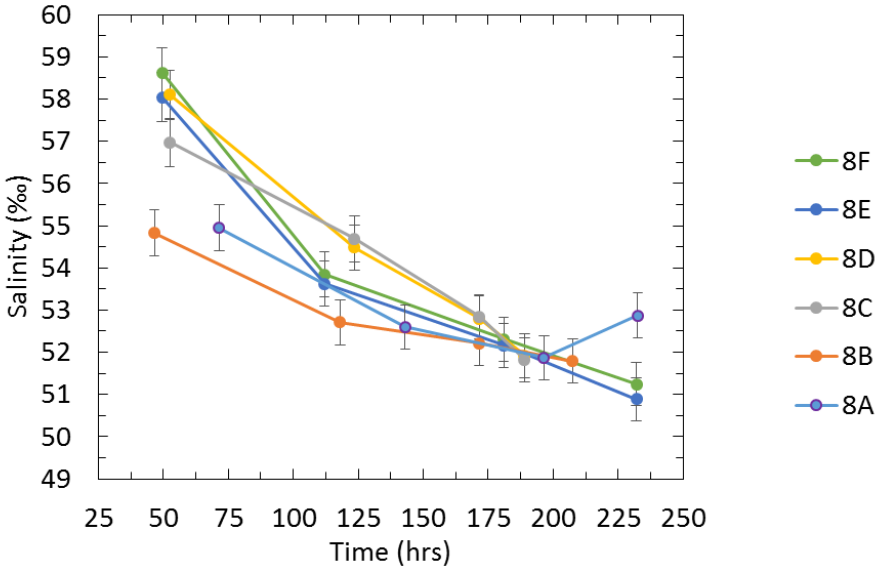

Figure 4.5 Graphical representation of salinity plotted against time for experiments 8A through 8F

(Na_2CO_3 titrate, pH during precipitation was 7.5-11). Analytical uncertainty is ± 1.0%.

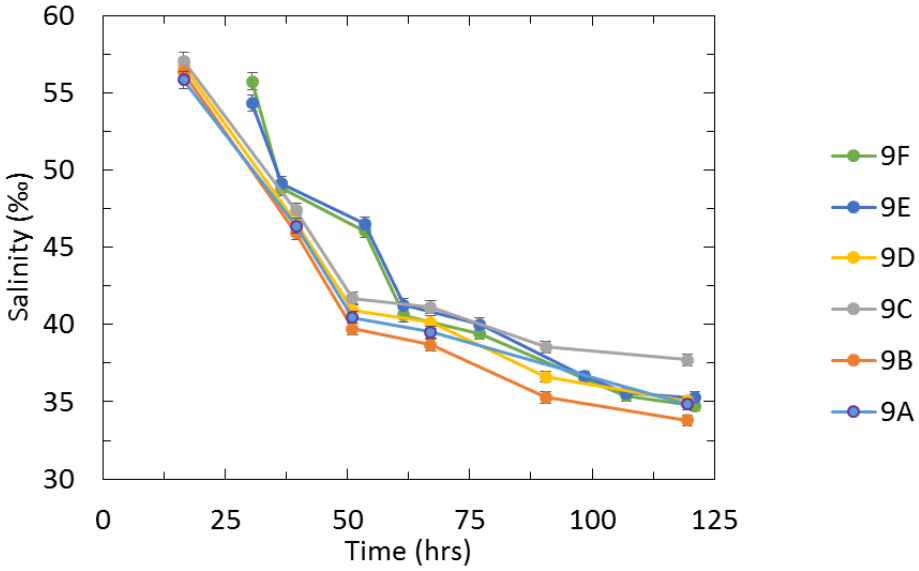

Figure 4.6 Graphical representation of salinity plotted against time for experiments 9A through 9F

($NaHCO_3$ titrate, pH during precipitation was 6-7). Analytical uncertainty is ± 1.0%.

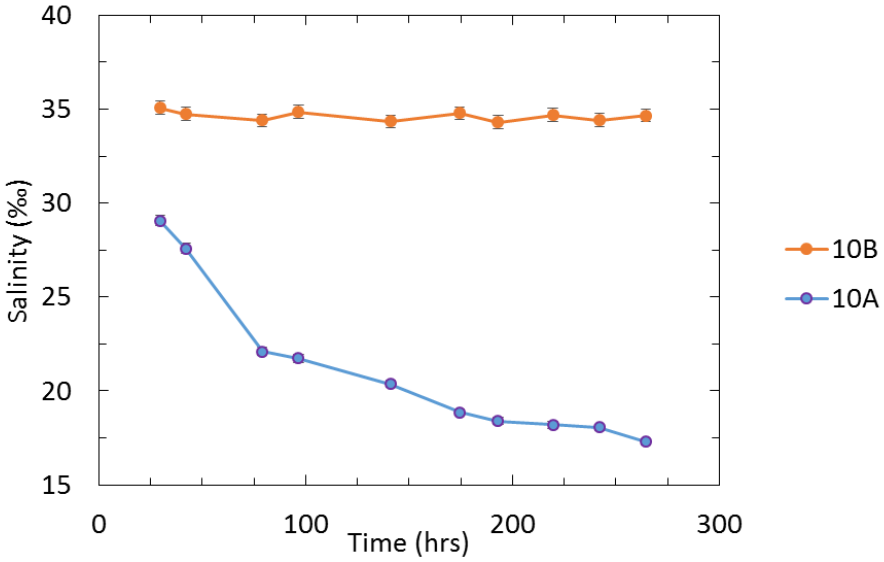

Figure 4.7 Graphical representation of salinity plotted against time for experiments 10A

($NaHCO_3$ titrate, pH during precipitation was 7.75-8.25) and 10B (Na_2CO_3 titrate, pH during precipitation was 8.5-9.5). Analytical uncertainty is ± 1.0%.

Table 4.5 Steady-state pH, average salinity, CO_3^{2-}, Ca^{2+}, and Mg^{2+} aqueous concentrations, initial and final saturation state, mass of precipitated calcium carbonate, mass percent of calcium carbonate polymorph precipitated, and duration of experimental runs

Run	pH_{ss}	Average Salinity (‰)	Initial CO_3^{2-}	Final CO_3^{2-}	Initial Ca^{2+}	Final Ca^{2+}	$Mg^{2+}{}_{ss}$	Initial Ω_C	Final Ω_C	$CaCO_3$ (g)	$CaCO_3$ polymorph* (mass %)	Experiment duration (hours)
8A	9.95	53.91	0.74	235.71	—	—	2.64	—	—	67.71	A(80), C(20)	207.5
8B	10.41	53.31	7.95	215.89	—	—	2.83	—	—	44.08	A(76), C(24)	207.5
8C†	10.39	54.40	0.06	52.91	—	—	5.83	—	—	60.41	A(78), C(12), MHC(10)	189
8D	10.55	55.01	0.01	35.19	—	—	0.18	—	—	64.15	A(39), C(26), V(35)	189
8E	10.20	54.47	0.07	15.54	—	—	5.10	—	—	63.8	A(59), C(41)	232
8F	10.21	54.94	20.28	43.95	—	—	8.42	—	—	55.25	A(79), C(21)	232
9A	6.86	45.34	0.15	0.07	14.28	8.09	43.24	3.45	1.01	17.74	C(100)	119.5
9B	6.78	45.08	0.08	0.11	22.28	8.30	28.26	3.06	1.57	18.68	C(100)	119.5
9C	6.54	47.38	0.04	0.51	29.47	16.71	15.57	1.80	13.21	19.79	C(100)	119.5
9D	6.30	45.89	0.02	0.05	61.92	43.59	1.64	1.67	3.18	20.59	C(100)	119.5
9E	6.43	44.81	0.02	0.04	58.51	36.11	7.15	1.85	2.27	22.68	C(100)	121
9F	6.61	45.25	0.04	0.06	45.01	33.20	15.79	3.21	3.23	22.04	C(100)	121
10A	7.96	22.44	0.22	0.18	2.95	1.62	0.32	2.53	1.16	1.53	C(100)	264.5
10B	9.33	34.70	2.76	0.49	0.18	0.17	0.53	1.16	0.20	3.08	C(100)	264.5

*A = aragonite, C = calcite, MHC = monohydrocalcite, V = vaterite

†XRD of powdered crystals for experiment 8C were carried out while crystals were wet.

The CO2SYS program developed by Pierrot et al. (2006) was utilized using the carbonate dissociation constants developed by Millero et al. (2006) and dissociation constant for HSO4 defined by Dickson (1990) to determine CO_3^{2-}.

All values for CO_3^{2-}, Ca^{2+}, and Mg^{2+} are reported in terms of mmol/kg.

Other values reported in Table 4.5 include: steady-state pH, average salinity, initial and final CO_3^{2-} and Ca^{2+} aqueous concentrations, steady-state Mg^{2+} aqueous concentrations, initial and final saturation state (Ω), mass of precipitated solid calcium carbonate, mass percent by polymorph of calcium carbonate precipitated which was determined using the MDI Jade 2010 software package, and experiment duration in hours. In order to determine saturation state of the fluid, with respect to calcite or aragonite, the alkalinity, pH, Ca concentration, temperature, and salinity of the fluid must first be known. Calcium carbonate saturation state (Ω) is expressed as:

$$\Omega = \frac{[Ca^{2+}][CO_3^{2-}]}{K^*_{sp}} \tag{4.3}$$

where K^*_{sp} is the stoichiometric solubility product for a certain mineral phase of $CaCO_3$ (e.g. calcite (calc), aragonite (arag), or low-magnesium calcite (lmc)); $[Ca^{2+}]$ and $[CO_3^{2-}]$ is the total molar concentration of the reacting (free + complexed) ions. The saturation state was calculated for experiments in series 9 and 10 in this manner. $[Ca^{2+}]$ was determined from the data collected from the fluid samples using LA-AAS. $[CO_3^{2-}]$ was determined by utilizing the program CO2SYS, originally developed by Lewis and Wallace (1998) and updated by Pierrot et al. (2006), using the carbonate dissociation constants developed by Millero et al. (2006) for carbonate systems and dissociation constant for HSO_4 defined by Dickson (1990) (to be included in alkalinity). The program uses two of four measurable input parameters of the aqueous carbonate system; TA, total dissolved inorganic carbon (TCO_2), pH, and the partial pressure of CO_2 (pCO_2) to calculate the other two parameters at set of input conditions (e.g. temperature and pressure) and a set of output conditions which includes CO_3^{2-} concentration (Pierrot et al.,

2006). K^*_{sp} was calculated using the expression developed by Mucci (1983) and modified in Zeebe and Wolf-Gladrow (2001).

4.5.2 X-ray diffraction results

The mass percent of each calcium carbonate polymorph precipitated from the various experiments were determined by the MDI Jade 2010 software package which analyzed XRD patterns of the scans. The XRD scans for series 8, 9, and 10 is shown in Figures 4.8 through 4.10, respectively. XRD scans for series 8 indicate the presence of calcite, aragonite, monohydrocalcite, and vaterite. The detection of monohydrocalcite in experiment 8C has been attributed to the sample being wet at the time of analysis. Scans for series 9 and 10 indicate only one polymorph of calcium carbonate being calcite.

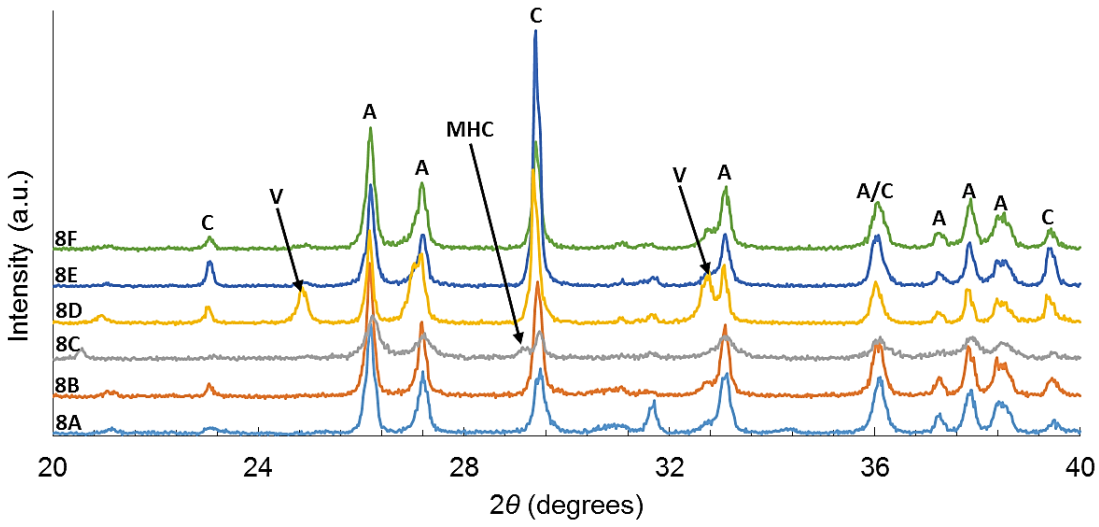

Figure 4.8 Series 8. Powdered X-ray diffraction scans with Cu-Kα radiation of different calcium carbonate polymorphs.

C = calcite, V = vaterite, A = aragonite, MHC = monohydrocalcite, A/C indicates the position of the peak that is representative of both calcite and aragonite. The experiment which corresponds with the diffraction pattern is noted along the y-axis of the plot.

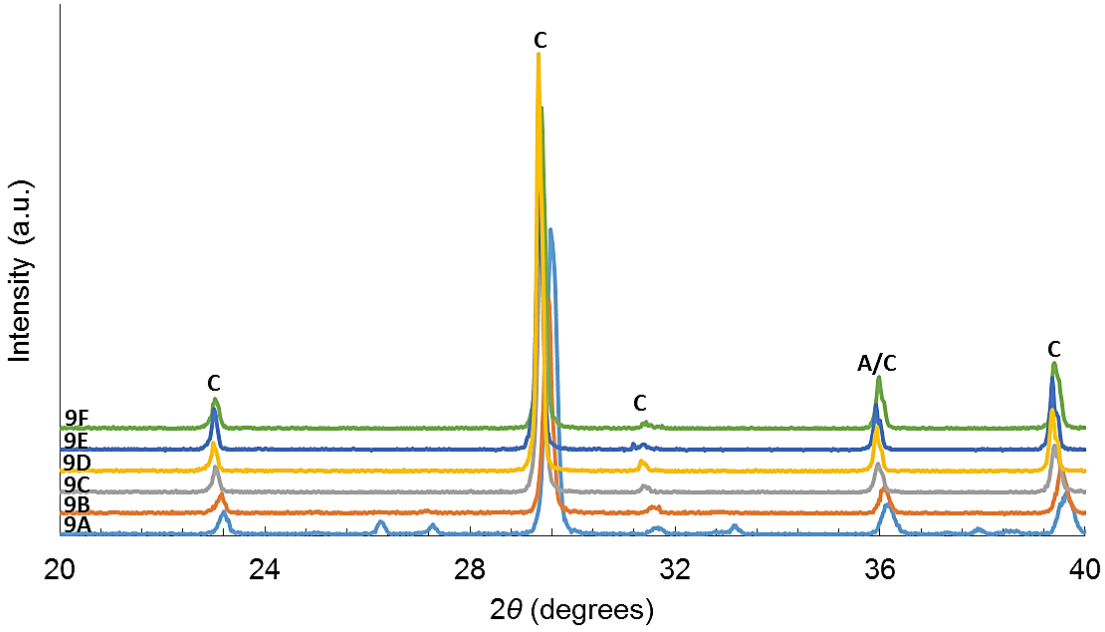

Figure 4.9 Series 9. Powdered X-ray diffraction scans with Cu-Kα radiation of different calcium carbonate polymorphs.

C = calcite and A/C indicates the position of the peak that is representative of both calcite and aragonite. The experiment which corresponds with the diffraction pattern is noted along the y-axis of the plot. The slight shift observed for the major peaks of each scan may be due to instrument drift from reoccurring use or slight variations in the Mg content.

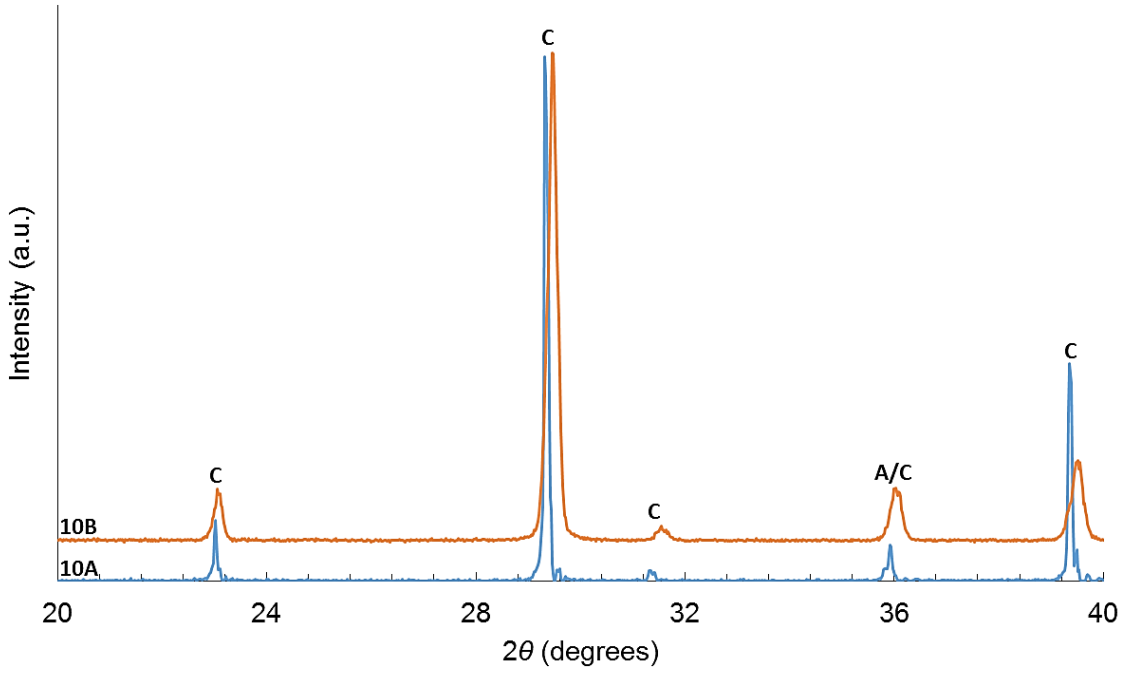

Figure 4.10 Series 10. Powdered X-ray diffraction scans with Cu-Kα radiation of different calcium carbonate polymorphs.

C = calcite and A/C indicates the position of the peak that is representative of both calcite and aragonite. The experiment which corresponds with the diffraction pattern is noted along the y-axis of the plot. The slight shift observed for the major peaks of each scan may be due to instrument drift from reoccurring use or slight variations in the Mg content. Experiment 10A was carried out using $NaHCO_3$ as the carbonate source whereas Na_2CO_3 was used in experiment 10B.

4.5.3 LS-AAS and ICP-OES Results

4.5.3.1 LS-AAS Results

The data collected from LS-AAS analysis has been compiled in a series of figures which show the aqueous Mg/Ca ratio evolution throughout the duration of the experiments conducted in series 9 and 10 (Figures 4.11 through 4.18). The $Mg/Ca_{(Fluid)}$ varies with time as a result of Mg and Ca concentrations in the fluid, the degree of variability is a matter of perspective controlled by the units of the y-axis (please note the difference in the scale for each of the figures). The Mg/Ca ratios from experiments in

series 8 are not reported as those experiments produced multiple calcium carbonate polymorphs which highly complicates the determination of the Mg/Ca ratio. Moreover, the concentration of the aqueous Ca in the majority of samples analyzed by LS-AAS were below the analytical detection limit.

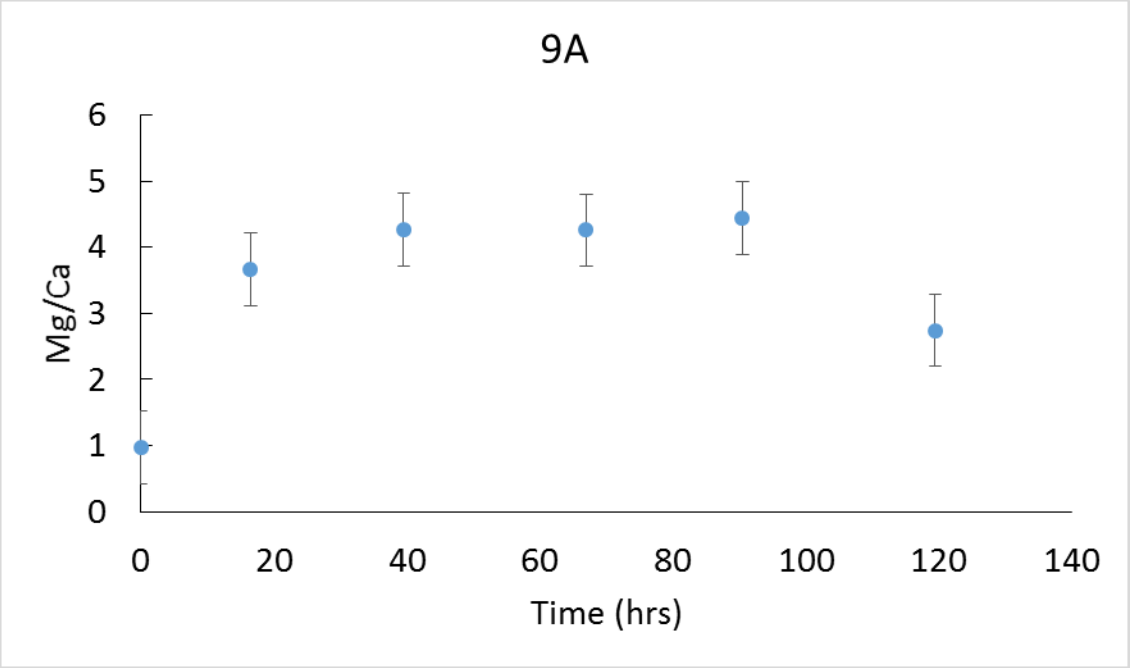

Figure 4.11 Aqueous Mg/Ca ratio plotted as a function of time for experiment 9A. Error bars represent the standard.

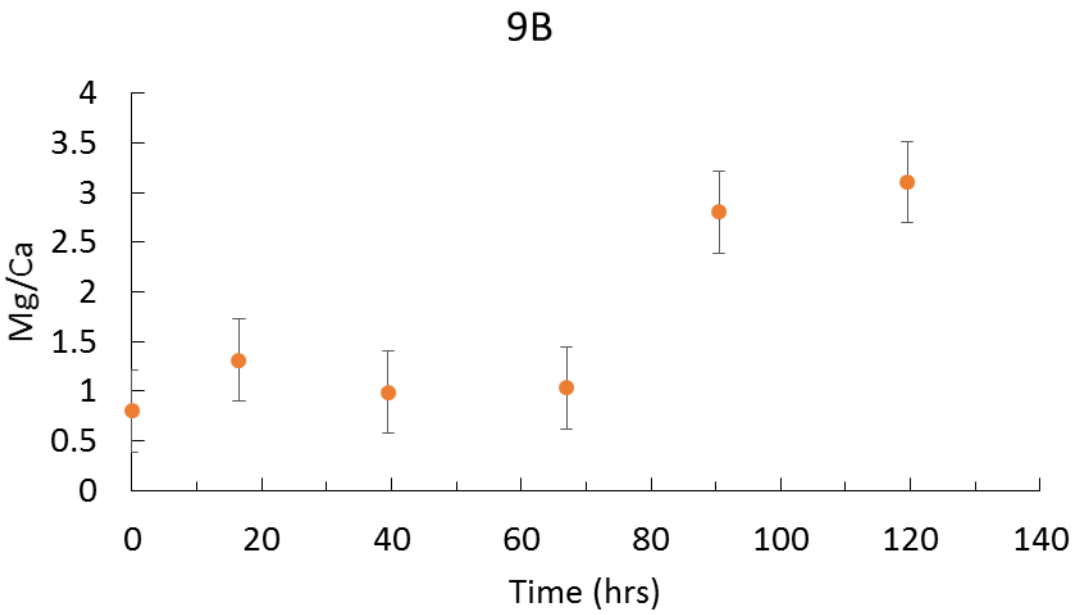

Figure 4.12 Aqueous Mg/Ca ratio plotted as a function of time for experiment 9B. Error bars represent the standard error.

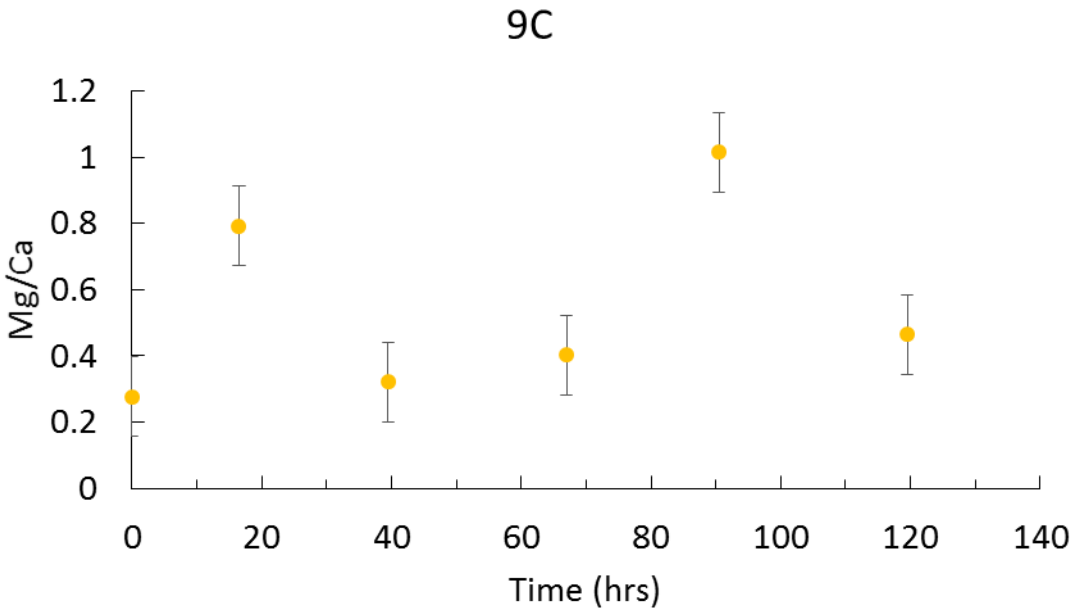

Figure 4.13 Aqueous Mg/Ca ratio plotted as a function of time for experiment 9C. Error bars represent the standard error.

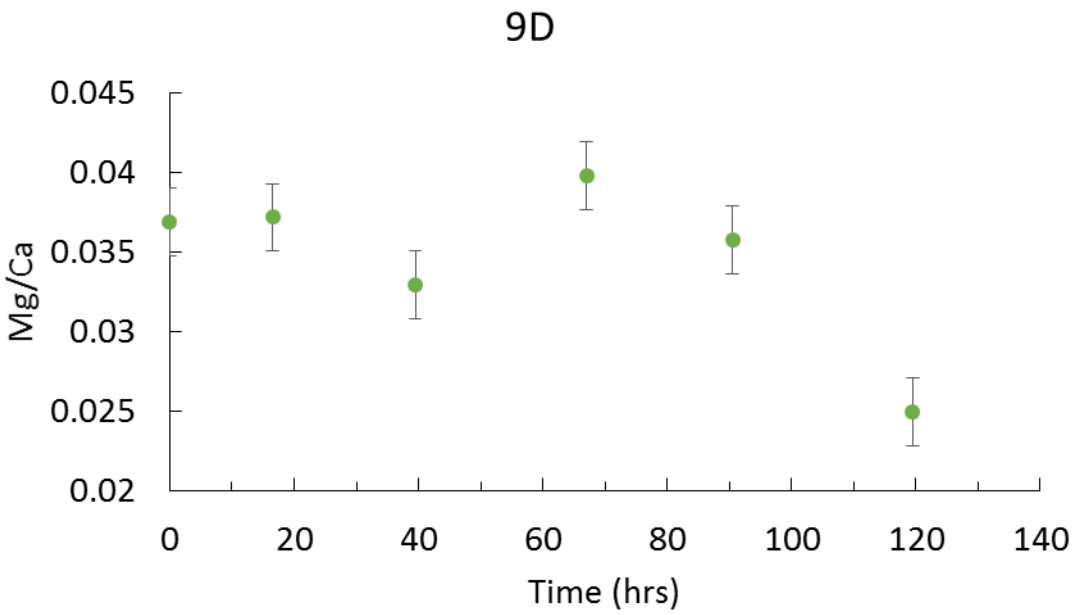

Figure 4.14 Aqueous Mg/Ca ratio plotted as a function of time for experiment 9D. Error bars represent the standard error.

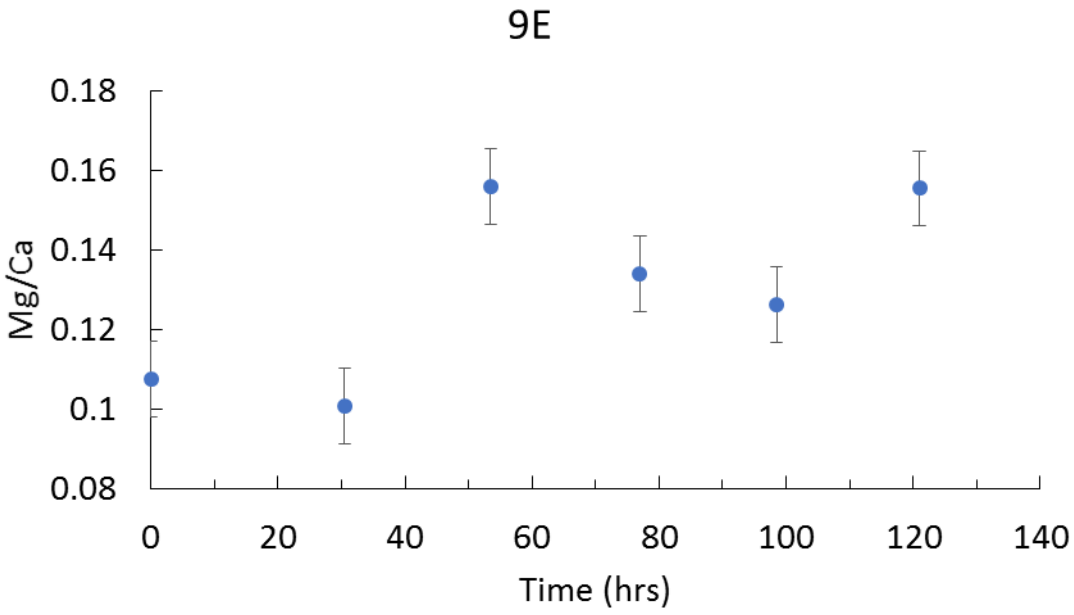

Figure 4.15 Aqueous Mg/Ca ratio plotted as a function of time for experiment 9F. Error bars represent the standard error.

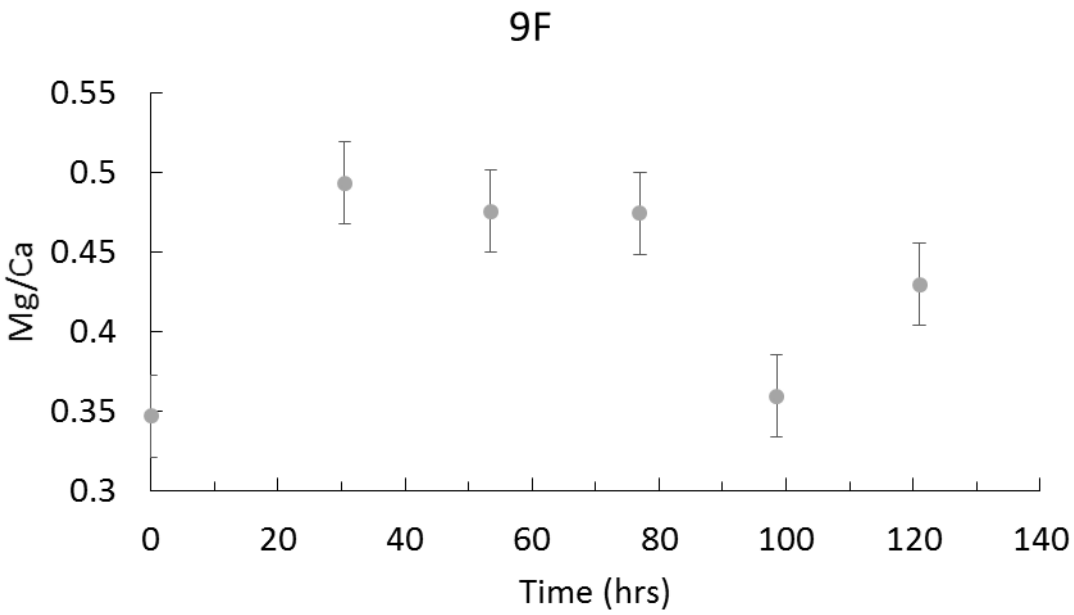

Figure 4.16 Aqueous Mg/Ca ratio plotted as a function of time for experiment 9F. Error bars represent the standard error.

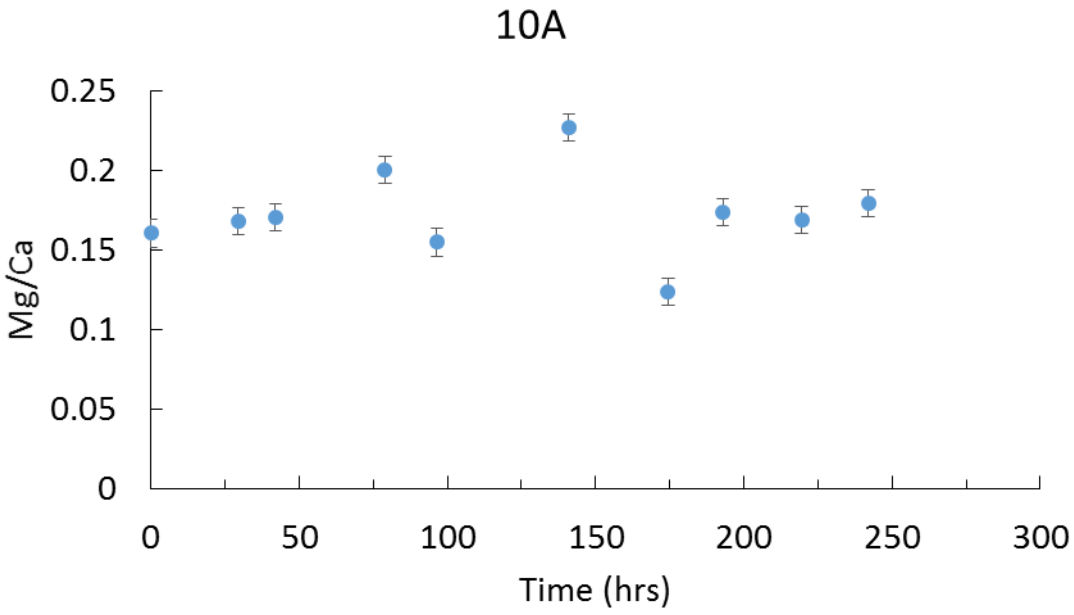

Figure 4.17 Aqueous Mg/Ca ratio plotted as a function of time for experiment 10A. Error bars represent the standard error.

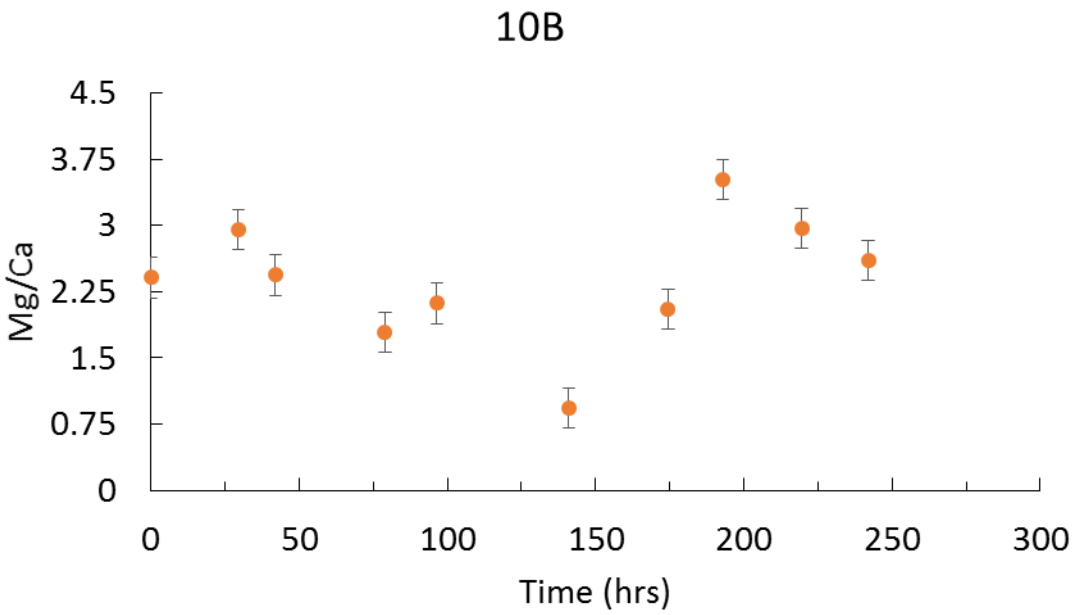

Figure 4.18 Aqueous Mg/Ca ratio plotted as a function of time for experiment 10B. Error bars represent the standard error.

4.5.3.2 ICP-OES Results

The data collected from ICP-OES and LA-AAS has been compiled into a figure which plots the aqueous Mg/Ca in mol/mol against the solid Mg/Ca in mmol/mol for experiments conducted in series 9 and 10 (Figure 4.19). Data for experiment 10B is not included on this plot as only data for aqueous Mg/Ca was collected. The Mg/Ca ratios from experiments in series 8 are not reported as those experiments produced aragonite, calcite, monohydrocalcite, and vaterite mixtures, which made analysis of Mg/Ca in solids superfluous.

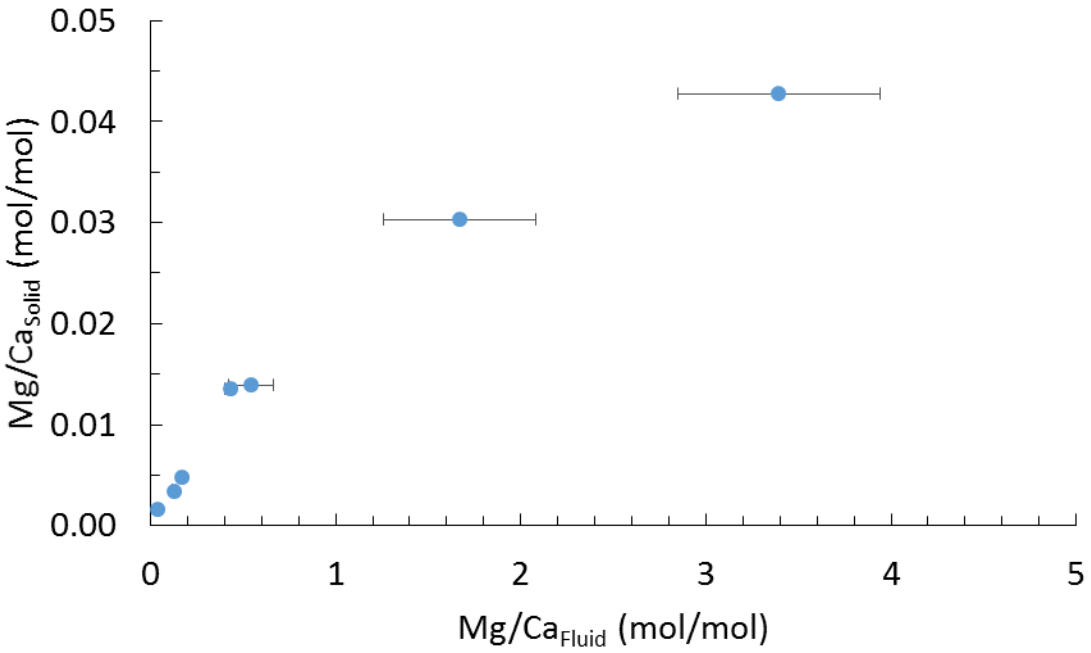

Figure 4.19 Mg/Ca concentration as a ratio in the solid precipitate plotted as a function of aqueous Mg/Ca concentration as a ratio.

Note that experiment 10B is not included in this figure as data was only collected for the aqueous Mg/Ca. The horizontal analytical uncertainty was determined in terms of standard error of the mean and the vertical analytical uncertainty in terms of the standard error of the mean was determined from the reproducibility of standard measurments using ICP-OES.

4.6 Discussion

4.6.1 Controls of Polymorph Precipitation

Results suggest that at elevated concentrations the chemical source of the carbonate anion (e.g. Na_2CO_3 or $NaHCO_3$) affects the precipitated polymorph of calcium carbonate probably by changing solution saturation state and/or pH. The term 'elevated concentrations' is meant to convey that the concentration of the major ions in the fluid are higher than what is considered to be the average for seawater. The use of Na_2CO_3 as a carbonate source instead of $NaHCO_3$ leads to higher pH values and in-turn higher Ω values. This was demonstrated by experiments in series 8 and experiment 10B which

were conducted using Na_2CO_3 as the carbonate source whereas $NaHCO_3$ was used as the carbonate source in experiments in series 9 and experiment 10A. The difference between this work and others (e.g. Mucci and Morse, 1983; Mavromatis et al., 2013; and Gabitov et al., 2014) is that pH was not maintained using buffers and was allowed to fluctuate.

It would have been ideal to determine, for series 8, if there is a dependence of the precipitated calcium carbonate polymorph on the parameters of the experiments. It is possible to speculate that pH may be responsible for the precipitation of the various polymorphs. Though, it cannot be quantitatively confirmed, as sub-samples of the solid precipitate were not collected throughout the duration of the experiments. It may also be possible that the precipitated polymorph is dependent on the degree of carbonate mineral supersaturation as suggested by Burton and Walter (1987). Though to determine this, it would be necessary to know the aqueous CO_3^{2-} ion concentration. Moreover, there may be evidence to support the growth of the different calcium carbonate polymorphs based on the pH of the fluid. Notice in Figure 4.2. that the pH values for all experiments in series 8 are relatively low then after about 50 hours, the pH has increased dramatically and begun to stabilize. This may be indicative of initial calcite precipitation at low pH followed by the precipitation of other polymorphs at elevated pH.

An interesting phenomenon that can be observed in the XRD data collected for series 8 suggests that as aqueous calcium concentration decreases concurrently with increasing magnesium concentration, the precipitated calcium carbonate polymorph begins to shift from being predominately aragonite to a mixture of aragonite, calcite, and other calcium carbonate polymorphs (see Table 4.5). It is unclear if this occurrence can be attributed to other causes such as salinity, as the final salinity values reported for series

8 are very different from those reported in series 9. It is possible that the saturation state may also influence the precipitated polymorph as those experiments with high saturation states produced more aragonite by percent mass than did those experiments in series 8 with lower saturation states (see Table 4.5).

4.6.2 Mg/Ca Ratios in Synthetic Low-Magnesium Calcite

The initial goal this study was to determine if $Mg/Ca_{(Fluid)}$ is capable of effecting K^{Mg} and can $Mg/Ca_{(Fluid)}$ explain the variability of foraminiferal Mg/Ca. For our experiments K^{Mg} was calculated using the following expression:

$$\left(K^{Mg} = \frac{(Mg/Ca)_{Solid}}{(Mg/Ca)_{Fluid}}\right) \quad (4.4)$$

To determine K^{Mg} using the previous equation it is imperative the $Mg/Ca_{(Fluid)}$ remained near-constant through the entirety of each experiment. Although Figures 4.11 through 4.18 demonstrate that $Mg/Ca_{(Fluid)}$ significantly varied in some of the experiments, it was still possible to determine K^{Mg} by using an averaged value of $Mg/Ca_{(Fluid)}$.

It has also been shown that K^{Mg} is not dependent upon the calcium or magnesium concentration in solution but on Mg/Ca only. This becomes evident when K^{Mg}, Mg/Ca, Ca and Mg concentrations from this study are compared with those of Mucci and Morse (1983) and Mavromatis et al. (2013) (see Figure 4.20). For data from Mucci and Morse (1983), Ca concentrations are in the range of 147-255 ppm, while Mg vary from 639 to 2503 ppm. For data from Mavromatis et al. (2013), Ca concentrations are higher (308-640 ppm) and Mg concentrations (194-294 ppm) are lower than fluid Mg in the experiments of Mucci and Morse (1983). In the present study, Ca and Mg concentration ranges were (65-1744 ppm) and (8-1050 ppm), respectively.

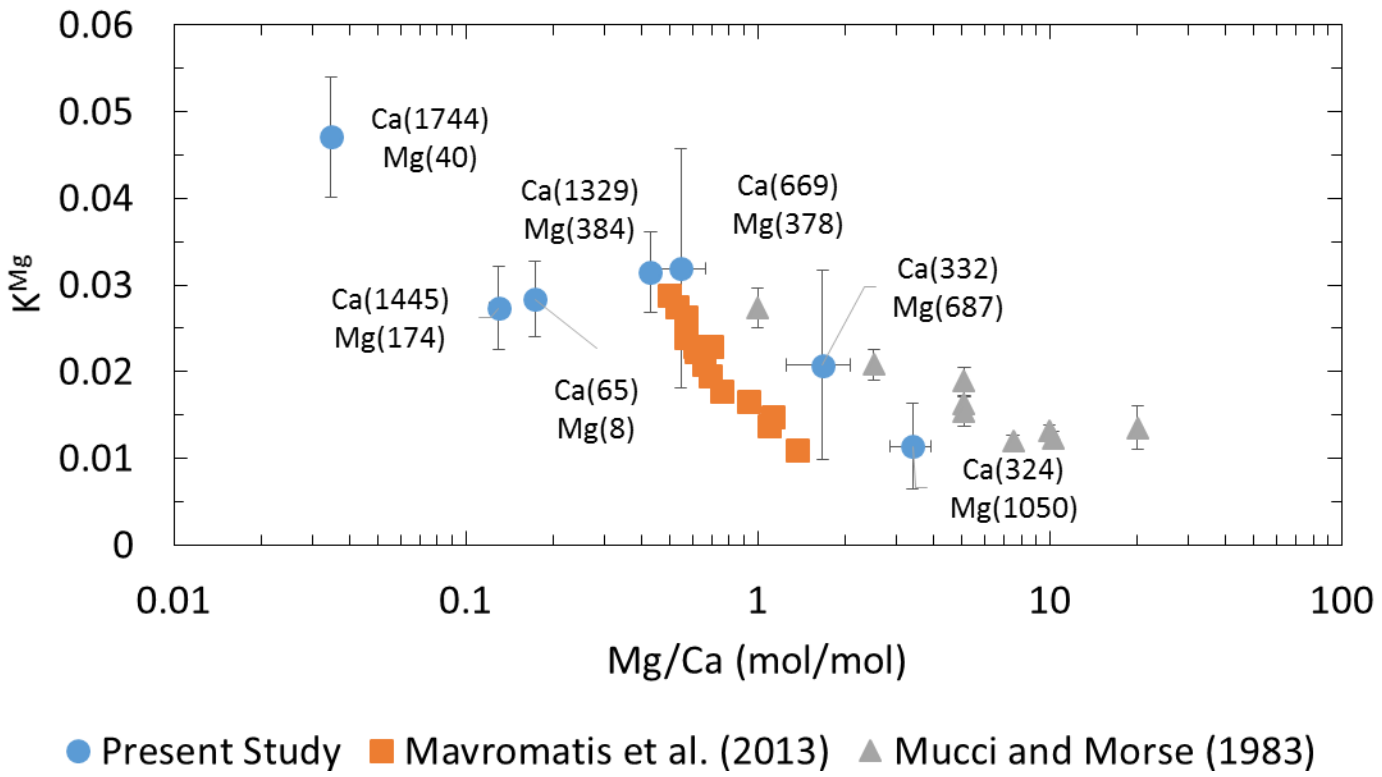

Figure 4.20 A log-linear plot demonstrating the relationship between aqueous Mg/Ca and K^{Mg}.

Blue cirlces represent data from the present study, orange squares are data from Mavromatis et al. (2013), and gray triangles are data from Mucci and Morse (1983). Horizontal analytical uncertainty for data in the present study was determined in terms of the standard error of the mean. Vertical analytical uncertainty was determined by formula: $\sqrt{((Mg/Ca_{(Solid)}\ Error)^2/(Mg/Ca_{(Fluid)})^2+(Mg/Ca_{(Fluid)}\ Std.dev)^2/(Mg/Ca_{(Fluid)})^4\cdot(Mg/Ca_{(Solid)})^2)}$. Values in parenthesis are aqueous Ca and Mg concentrations in ppm.

Using the values for $Mg/Ca_{(Solid)}$ and $Mg/Ca_{(Fluid)}$ under steady-state conditions K^{Mg} was calculated (see Table 4.6). To determine the relationship between $Mg/Ca_{(Fluid)}$ and K^{Mg} the values were plotted on a log-linear plot. By plotting the values in such a way it became apparent that K^{Mg} increases with decreasing $Mg/Ca_{(Fluid)}$ (see Figure. 4.20). These findings agree with the data collected by Mucci and Morse (1983) and Mavromatis et al. (2013). K^{Mg} could not be plotted as a function of precipitation rate/growth rate as sub-samples of the solid precipitate were not collected at regular intervals throughout the duration of the experiments. Nor was the total calcite surface determined (it was changing during experiment) so that growth rate could be calculated as a function of Ca and Mg concentration added and removed from the reaction vessel during a given amount of time.

Table 4.6 Solid and aqueous Mg/Ca, K^{Mg}

Experiment	Mg/Ca_{solid} (mol/mol)	Mg/Ca_{Fluid} (mol/mol)	1σ	SEM	$LogK_{Mg}$	K^{Mg}	error
9A	0.0428	3.3918	1.3383	0.5464	-1.9435	0.0114	0.0050
9B	0.0303	1.6718	1.0094	0.4121	-1.6827	0.0208	0.0110
9C	0.0139	0.5452	0.2943	0.1201	-1.4961	0.0319	0.0139
9D	0.0016	0.0346	0.0052	0.0021	-1.3270	0.0471	0.0073
9E	0.0035	0.1299	0.0233	0.0095	-1.5635	0.0273	0.0050
9F	0.0135	0.4298	0.0632	0.0258	-1.5014	0.0315	0.0049
10A	0.0048	0.1728	0.0273	0.0086	-1.5470	0.0284	0.0046
10B	—	2.3771	0.7179	0.2270	—	—	—

SEM is the standard error of the mean. SEM of Mg/Ca_{Solid} was calculated from the reproducibility of standard measurements using ICP-OES.
K^{Mg} error was determined using the formula: $\sqrt{((Mg/Ca_{Solid}\ Error)^2/(Mg/Ca_{Fluid})^2+(Mg/Ca_{Fluid}\ Std.dev)^2/(Mg/Ca_{Fluid})^4\cdot(Mg/Ca_{Solid})^2)}$.

4.7 Conclusions

This study confirms the previously observed inverse relationship of K^{Mg} on fluid Mg/Ca when $0.4 < Mg/Ca_{(Fluid)} < 4$ mol/mol demonstrating that K^{Mg} increases with

decreasing $Mg/Ca_{(Fluid)}$. Though for $Mg/Ca_{(Fluid)}$ concentrations lower than 0.4 and higher than 0.03 mol/mol, our results demonstrate a deviation from the established relationship. More research is needed in order to constrain the cause for the reported deviation. It has also been shown that aqueous concentration of Mg or Ca individually do not influence K^{Mg}.

The experiments preformed in this study indicate that at elevated saturation of seawater with $CaCO_3$, it is possible to precipitate multiple polymorphs of calcium carbonate when using Na_2CO_3 salts as the carbonate source ($7.7 \leq pH \leq 10.8$). In contrast, only calcite precipitated while using $NaHCO_3$ salts as the carbonate source, which produced fluids with lower pH (6.0-7.0) and saturation states. It will be necessary to conduct more experiments similar to those conducted in series 8 to determine more precisely the factor(s) which influence the precipitation of the various calcium carbonate polymorphs. In determining the control factor(s) in laboratory experiments, it may become possible to better understand the preference to precipitate a specific calcium carbonate polymorph from natural seawater when the difference in temperature is not a factor.

This study has shown $Mg/Ca_{(Solid)}$ increases with increasing $Mg/Ca_{(Fluid)}$ in a linear manner when $Mg/Ca_{(Fluid)}$ increases from 0.03 to 3.39 mol/mol. Implying that Mg uptake in low-Mg calcite is linearly proportional to the Mg concentration in solution. These findings may provide some perspective on the mechanisms proposed by Bentov and Erez (2006) to explain the Mg content of foraminiferal shells.

CHAPTER V

SUMMARY

This dissertation was carried out with three main goals in mind: 1) the investigation of the influence of pressure on element partitioning in aragonite; 2) the numerical simulation and determination of growth rate influence on the incorporation of uranium to calcite, and 3) the refinement of an experimental technique designed to promote the growth of inorganic low-Mg calcite while maintaining $Mg/Ca_{(Fluid)}$ near-constant.

In Chapter Two, two sets of experiments were conducted to evaluate the geochemical response of aragonite to pressure. One set of experiments produced crystalline calcium carbonate created by the mixture of Na_2CO_3 and artificial seawater, at two temperatures (7.8 and 22 °C), under the influence of atmospheric pressure. The second set of experiments produced crystalline calcium carbonate created using the same mixture ratio of Na_2CO_3 and artificial seawater, at 7.8 and 22 °C, under the influence of 25, 75, 100, and 345 bars of pressure produced by high-purity N_2 gas. With the available data it was concluded that oceanic floor pressure could affect the crystallization of $CaCO_3$ by altering mineralogical composition and aragonite crystal size. Partition coefficients of vanadium, manganese, and iron between synthetic aragonite and fluid were determined for the first time. Additional research is needed to assess the aforementioned relationships and further explore variability among precipitated crystals.

Chapter Three sought to study the kinetic effects of U/Ca incorporation into calcite. Synthetic calcite crystals were produced isothermally from NH_4Cl-$CaCl_2$ doped with uranium by diffusion of CO_2. The calcite-precipitating fluid was sequentially spiked with rare earth element dopants at set time intervals. The resulting crystals were then analyzed with SIMS for Ca, REE, and U to determine growth rate of the crystals. Results showed that the partitioning of uranium increases with increasing growth rate. To explain the relationship observed, numerical simulations using the growth entrapment model (GEM, sometime referred as SEMO) and unified uptake kinetics model (UUKM) were conducted.

In Chapter Four, the aim was to determine the relationship between $Mg/Ca_{(Fluid)}$ and the Mg partition coefficient for the range of Mg/Ca values reported for planktonic foraminifera. In nature, planktonic foraminifera produce low-magnesium calcite with distinct Mg/Ca that is typically found to be within the range of ~1.6 to ~10.2 mmol/mol based on data from Nürnberg et al. (1996); Lea et al. (1999); Kısakürek et al. (2008); Dueñas-Bohórquez et al. (2011); Hönisch et al. (2013). This Mg/Ca_{foram} range does not correspond to Mg/Ca_{foram} expected for crystallization from high Mg/Ca seawater (~5200 mmol/mol). To achieve this goal, inorganic low-magnesium calcite was produced mixing solutions containing $CaCl_2$, $MgCl_2$, NaCl, and either Na_2CO_3 or $NaHCO_3$ as the carbonate source in a reaction vessel housed in a refrigerated water bath. The solutions were continuously delivered and extracted from the reaction vessel using a multi-channel peristaltic pump. The resulting crystals were analyzed using ICP-OES and X-ray diffractometry, while fluids were analyzed using line source atomic adsorption spectroscopy. Mg/Ca in fluids were analyzed with Atomic Absorption Spectroscopy

(AAS). From this work it was determined that Mg partition coefficient decreases when $Mg/Ca_{(Fluid)}$ increases. The calcites produced in the present study were precipitated from fluids of low Mg/Ca (30-3400 mmol/mol) in order to cover Mg/Ca range observed in foraminifera. This Mg/Ca is different to other experimental works where fluid Mg/Ca varied from 500 to 20,000 mmol/mol (e.g. Mucci and Morse, 1983; Mavromatis et al., 2013). In the future, it will be necessary to focus research on $Mg/Ca_{(Fluid)}$ values lower than 0.4 mol/mol as our results demonstrate a deviation from the established relationship between K^{Mg} and $Mg/Ca_{(Fluid)}$.

REFERENCES

Allison, N., 1996, Comparative determinations of trace and minor elements in coral aragonite by ion microprobe analysis, with preliminary results from Phuket, southern Thailand: Geochimica et Cosmochimica Acta, v. 60, p. 3457–3470.

Allison, N., and Finch, A.A., 2007, High temporal resolution Mg/Ca and Ba/Ca records in modern *Porites lobata* corals: Geochemistry, Geophysics, Geosystems, v. 8.

Anand, P., Elderfield, H., and Conte, M.H., 2003, Calibration of Mg/Ca thermometry in planktonic foraminifera from a sediment trap time series: Paleoceanography, v. 18, p. 28–31.

Baker, A., Genty, D., Dreybrodt, W., Barnes, W.L., Mockler, N.J., and Grapes, J., 1998, Testing theoretically predicted stalagmite growth rate with recent annually laminated samples: Implications for past stalagmite deposition: Geochimica et Cosmochimica Acta, v. 62, p. 393–404.

Bates, R.G., 1973, Determination of pH, theory and practice (2d ed.): New York, John Wiley & Sons, p. 333–336.

Bath, G.E., Thorrold, S.R., Jones, C.M., Campana, S.E., McLaren, J.W., and Lam, J.W.H., 2000, Strontium and barium uptake in aragonitic otoliths of marine fish: Geochimica et Cosmochimica Acta, v. 64, p. 1705–1714.

Beck, J.W., Edwards, R.L., Ito, E., Taylor, F.W., Recy, J., Rougerie, F., Joannot, P., and Henin, C., 1992, Sea-surface temperature from coral skeletal strontium/calcium ratios: Science, v. 257, p. 644–647.

Bentov, S., and Erez, J., 2006, Impact of biomineralization processes on the Mg content of foraminiferal shells: A biological perspective: Geochemistry, Geophysics, Geosystems, v. 7.

Ben-Yaakov, S., Ruth, E., and Kaplan, I.R., 1974, Carbonate compensation depth: Relation to carbonate solubility in ocean waters: Science, v. 184, p. 982–984.

Blackmon, P.D., and Todd, R., 1959, Mineralogy of some foraminifera as related to their classification and ecology: Journal of Paleontology, p. 1–15.

Boiteau, R., Greaves, M., and Elderfield, H., 2012, Authigenic uranium in foraminiferal coatings: A proxy for ocean redox chemistry: Paleoceanography, v. 27, p. 1–8.

Brennan, S.T., Lowenstein, T.K., and Horita, J., 2004, Seawater chemistry and the advent of biocalcification: Geology, v. 32, p. 473–476.

Broecker, W., and Yu, J., 2011, What do we know about the evolution of Mg to Ca ratios in seawater?: Paleoceanography, v. 26, p. 1–8.

Brooks, R., Clark, L.M., and Thurston, E.F., 1950, Calcium carbonate and its hydrates: Philosophical Transactions of the Royal Society of London. Series A, Mathematical and Physical Sciences, v. 243, p. 145–167.

Burton, E.A., and Walter, L.M., 1987, Relative precipitation rates of aragonite and Mg calcite from seawater: temperature or carbonate ion control?: Geology, v. 15, p. 111–114.

Burton, E.A., and Walter, L.M., 1990, The role of pH in phosphate inhibition of calcite and aragonite precipitation rates in seawater: Geochimica et Cosmochimica Acta, v. 54, p. 797–808.

Busenberg, E., and Niel Plummer, L., 1989, Thermodynamics of magnesian calcite solid-solutions at 25°C and 1 atm total pressure: Geochimica et Cosmochimica Acta, v. 53, p. 1189–1208.

Coggon, R.M., Teagle, D.A.H., Smith-Duque, C.E., Alt, J.C., and Cooper, M.J., 2010, Reconstructing past seawater Mg/Ca and Sr/Ca from mid-ocean ridge flank calcium carbonate veins: Science, v. 327, p. 1114–1117.

Cole, J.M., Rasbury, E.T., Montanez, I.P., Pedone, V.A., Lanzirotti, A., and Hanson, G.N., 2004, Petrographic and trace element analysis of uranium-rich tufa calcite, middle Miocene Barstow Formation, California, USA: Sedimentology, v. 51, p. 433–453.

Dahl, K., and Buchardt, B., 2006, Monohydrocalcite in the Arctic Ikka Fjord, SW Greenland: First reported marine occurrence: Journal of Sedimentary Research, v. 76, p. 460–471.

Demicco, R.V., Lowenstein, T.K., Hardie, L.A., and Spencer, R.J., 2005, Model of seawater composition for the Phanerozoic: Geology, v. 33, p. 877–880.

Denniston, R.F., Shearer, C.K., Layne, G.D., and Vaniman, D.T., 1997, SIMS analyses of minor and trace element distributions in fracture calcite from Yucca Mountain, Nevada, USA: Geochimica et Cosmochimica Acta, v. 61, p. 1803–1818.

DePaolo, D.J., 2011, Surface kinetic model for isotopic and trace element fractionation during precipitation of calcite from aqueous solutions: Geochimica et Cosmochimica Acta, v. 75, p. 1039–1056.

Devery, D.M., and Ehlmann, A.J., 1981, Morphological changes in a series of synthetic Mg-calcites: American Mineralogist, v. 66, p. 592–595.

Dickson, A.G., 1990, Thermodynamics of the dissociation of boric acid in synthetic seawater from 273.15 to 318.15 K: Deep Sea Research Part A: Oceanographic Research Papers, v. 37, p. 755–766.

Dickson, J.A.D., 2002, Fossil echinoderms as monitor of the Mg/Ca ratio of Phanerozoic oceans: Science, v. 298, p. 1222–1224.

Dietzel, M., Gussone, N., and Eisenhauer, A., 2004, Co-precipitation of Sr^{2+} and Ba^{2+} with aragonite by membrane diffusion of CO_2 between 10 and 50 °C: Chemical Geology, v. 203, p. 139–151.

Djogić, R., Sipos, L., and Branica, M., 1986, Characterization of uranium (VI) in seawater: Liminology and Oceanography, v. 31, p. 1122–1131.

Doerner, H.A., and Hoskins, W.M., 1925, Co-Precipitation of radium and barium sulfates: Journal of the American Chemical Society, v. 47, p. 662–675.

Domingo, C., García-Carmona, J., Loste, E., Fanovich, A., Fraile, J., and Gómez-Morales, J., 2004, Control of calcium carbonate morphology by precipitation in compressed and supercritical carbon dioxide media: Journal of Crystal Growth, v. 271, p. 268–273.

Domingo, C., Loste, E., Gómez-Morales, J., García-Carmona, J., and Fraile, J., 2005, Calcite precipitation by a high-pressure CO_2 carbonation route: Journal of Supercritical Fluids, v. 36, p. 202–215.

Dong, S., Subha, A., Rollins, N., Berelson, W., Adkins, J., 2016, Kinetics of inorganic calcite dissolution in seawater under pressure: Abstract AH14A-0012 presented at 2016 Ocean Sciences Meeting, AGU, New Orleans, Louisiana, 21–26 February.

Dueñas-Bohórquez, A., da Rocha, R.E., Kuroyanagi, A., de Nooijer, L.J., Bijma, J., and Reichart, G.J., 2011, Interindividual variability and ontogenetic effects on Mg and Sr incorporation in the planktonic foraminifer *Globigerinoides sacculifer*: Geochimica et Cosmochimica Acta, v. 75, p. 520–532.

Dunk, R.M., Mills, R.A., and Jenkins, W.J., 2002, A reevaluation of the oceanic uranium budget for the Holocene: Chemical Geology, v. 190, p. 45–67.

Elderfield, H., Bertram, C.J., and Erez, J., 1996, Biomineralization model for the incorporation of trace elements into foraminiferal calcium carbonate: Earth and Planetary Science Letters, v. 142, p. 409–423.

Elderfield, H., and Ganssen, G., 2000, Past temperature and delta18O of surface ocean waters inferred from foraminiferal Mg/Ca ratios.: Nature, v. 405, p. 442–445.

Fairchild, I.J., and Treble, P.C., 2009, Trace elements in speleothems as recorders of environmental change: Quaternary Science Reviews, v. 28, p. 449–468.

Ferguson, J.E., Henderson, G.M., Kucera, M., and Rickaby, R.E.M., 2008, Systematic change of foraminiferal Mg/Ca ratios across a strong salinity gradient: Earth and Planetary Science Letters, v. 265, p. 153–166.

Füchtbauer, H., and Hardie, L.A., 1976, Experimentally determined homogeneous distribution coefficients for precipitated magnesian calcites: application to marine carbonate cements, *in* Geological Society of America Abstracts with Program, v. 8, p. 877.

Fukushi, K., Munemoto, T., Sakai, M., and Yagi, S., 2011, Monohydrocalcite: a promising remediation material for hazardous anions: Science and Technology of Advanced Materials, v. 12.

Gabitov, R.I., and Watson, E.B., 2006, Partitioning of strontium between calcite and fluid: Geochemistry, Geophysics, Geosystems, v. 7, p. 1–12.

Gabitov, R.I., Gaetani, G.A., Watson, E.B., Cohen, A.L., and Ehrlich, H.L., 2008, Experimental determination of growth rate effect on U^{6+} and Mg^{2+} partitioning between aragonite and fluid at elevated U^{6+} concentration: Geochimica et Cosmochimica Acta, v. 72, p. 4058–4068.

Gabitov, R.I., Watson, E.B., and Sadekov, A., 2012, Oxygen isotope fractionation between calcite and fluid as a function of growth rate and temperature: An in situ study: Chemical Geology, v. 306-307, p. 92–102.

Gabitov, R.I., Gagnon, A.C., Guan, Y., Eiler, J.M., and Adkins, J.F., 2013, Accurate Mg/Ca, Sr/Ca, and Ba/Ca ratio measurements in carbonates by SIMS and NanoSIMS and an assessment of heterogeneity in common calcium carbonate standards: Chemical Geology, v. 356, p. 94–108.

Gabitov, R.I., Sadekov, A., and Leinweber, A., 2014a, Crystal growth rate effect on Mg/Ca and Sr/Ca partitioning between calcite and fluid: An in situ approach: Chemical Geology, v. 367, p. 70–82.

Gabitov, R.I., Rollion-Bard, C., Tripati, A., and Sadekov, A., 2014b, In situ study of boron partitioning between calcite and fluid at different crystal growth rates: Geochimica et Cosmochimica Acta, v. 137, p. 81–92.

Gaetani, G.A., and Cohen, A.L., 2006, Element partitioning during precipitation of aragonite from seawater: A framework for understanding paleoproxies: Geochimica et Cosmochimica Acta, v. 70, p. 4617–4634.

Garrels, R.M., and Mackenzie, F.T., 1971, Evolution of sedimentary rocks. New York: W.W. Norton and Co., 397 p.

Genty, D., Baker, a., and Vokal, B., 2001, Instra- and inter-annual growth rate of modern stalagmites: Chemical Geology, v. 176, p. 191–212.

Given, R.K., and Wilkinson, B.H., 1985a, Kinetic control of morphology, composition, and mineralogy of abiotic sedimentary carbonates: Journal of Sedimentary Research, v. 55, p. 109–119.

Given, R.K., and Wilkinson, B.H., 1985b, Kinetic control of morphology, composition, and mineralogy of abiotic sedimentary carbonates: REPLY: Journal of Sedimentary Research, v. 55, p. 921–926.

Glock, N., Eisenhauer, A., Liebetrau, V., Wiedenbeck, M., Hensen, C., and Nehrke, G., 2012, EMP and SIMS studies on Mn/Ca and Fe/Ca systematics in benthic foraminifera from the Peruvian OMZ: A contribution to the identification of potential redox proxies and the impact of cleaning protocols: Biogeosciences, v. 9, p. 341–359.

Gruzensky, P.M., 1967, Growth of calcite crystals. *In* Crystal Growth, Conference Proceedings of the International Conference on Crystal Growth (1966: Boston MA) (ed. H.S. Peiser), Supplement to Journal of Physics and Chemistry of Solids S, v. 365, Suppl. 1., Pergamon.

Hanor, J.S., 2003, Porewaters in sediments in: Middleton, G.V., ed., Encyclopedia of sediments and sedimentary rocks, p. 537-542.

Hardie, L.A., 1996, Secular variation in seawater chemistry: An explanation for the coupled secular variation in the mineralogies of marine limestones and potash evaporites over the past 600 m.y.: Geology, v. 24, p. 279–283.

Hart, S.R., and Cohen, A.L., 1996, An ion probe study of annual cycles of Sr/Ca and other trace elements in corals: Geochimica et Cosmochimica Acta, v. 60, p. 3075–3084.

Hartley, G., and Mucci, A., 1996, The influence of PCO_2 on the partitioning of magnesium in calcite overgrowths precipitated from artificial seawater at 25° and 1 atm total pressure: Geochimica et Cosmochimica Acta, v. 60, p. 315–324.

Hasiuk, F.J., and Lohmann, K.C., 2010, Application of calcite Mg partitioning functions to the reconstruction of paleocean Mg/Ca: Geochimica et Cosmochimica Acta, v. 74, p. 6751–6763.

Hastings, D.W., Emerson, S.R., Erez, J., and Nelson, B.K., 1996, Vanadium in foraminiferal calcite: Evaluation of a method to determine paleo-seawater vanadium concentrations: Geochimica et Cosmochimica Acta, v. 60, p. 3701–3715.

Hathorne, E.C., Felis, T., Suzuki, A., Kawahata, H., and Cabioch, G., 2013, Lithium in the aragonite skeletons of massive *Porites* corals: A new tool to reconstruct tropical sea surface temperatures: Paleoceanography, v. 28, p. 143–152.

Herzog, G.F., Anders, E., Alexander, E.C., Davis, P.K., and Lewis, R.S., 1973, Iodine-129/xenon-129 age of magnetite from the Orgueil meteorite.: Science (New York, N.Y.), v. 180, p. 489–91.

Hill, T.M., Kennett, J.P., and Valentine, D.L., 2004, Isotopic evidence for the incorporation of methane-derived carbon into foraminifera from modern methane seeps, Hydrate Ridge, Northeast Pacific: Geochimica et Cosmochimica Acta, v. 68, p. 4619–4627.

Holland, H.D., and Zimmermann, H., 2000, The Dolomite Problem Revisited[1]: International Geology Review, v. 42, p. 481–490.

Hönisch, B., Allen, K.A., Lea, D.W., Spero, H.J., Eggins, S.M., Arbuszewski, J., DeMenocal, P., Rosenthal, Y., Russell, A.D., and Elderfield, H., 2013, The influence of salinity on Mg/Ca in planktic foraminifers – Evidence from cultures, core-top sediments and complementary $\delta^{18}O$: Geochimica et Cosmochimica Acta, v. 121, p. 196–213.

Horita, J., Weinberg, A., Das, N., and Holland, H.D., 1996, Brine inclusions in halite and the origin of the Middle Devonian Prairie evaporites of western Canada: Journal of Sedimentary Research, v. 66, p. 956–964.

Horita, J., Zimmermann, H., and Holland, H.D., 2002, Chemical evolution of seawater during the Phanerozoic: implications from the record of marine evaporites: Geochimica et Cosmochimica Acta, v. 66, p. 3733–3756.

Howson, M.R., Pethybridge, A.D., and House, W.A., 1987, Synthesis and distribution coefficient of low-magnesium calcites: Chemical Geology, v. 64, p. 79–87.

Huang, Y., and Fairchild, I.J., 2001, Partitioning of Sr^{2+} and Mg^{2+} into calcite under karst-analogue experimental conditions: Geochimica et Cosmochimica Acta, v. 65, p. 47–62.

Hummel, W., Berner, U., Curti, E., Pearson, F.J., and Thoenen, T., 2002, Nagra/PSI chemical thermodynamic data base 01/01: Radiochimica Acta, v. 90, p. 805–813.

Ibrahim, A.R., Vuningoma, J.B., Hu, X., Gong, Y., Hua, D., Hong, Y., Wang, H., and Li, J., 2012, High-pressure gas-solid carbonation route coupled with a solid ionic liquid for rapid synthesis of rhombohedral calcite: Journal of Supercritical Fluids, v. 72, p. 78–83.

Inoue, M., Suwa, R., Suzuki, A., Sakai, K., and Kawahata, H., 2011, Effects of seawater pH on growth and skeletal U/Ca ratios of *Acropora digitifera* coral polyps: Geophysical Research Letters, v. 38, p. 2–5.

Jamieson, J. C., 1953, Phase equilibrium in the system calcite-aragonite: Journal of Chemical Physics, v. 21, p. 1385–1390.

Johnson, K.M., Wills, K.D., Butler, D.B., Johnson, W.K., and Wong, C.S., 1993, Coulometric total carbon dioxide analysis for marine studies: maximizing the performance of an automated gas extraction system and coulometric detector: Marine Chemistry, v. 44, p. 167–187.

Kamiya, K., Sakka, S., and Terada, K., 1977, Aragonite formation through precipitation of calcium carbonate monohydrate: Materials Research Bulletin, v. 12, p. 1095–1102.

Katz, A., 1973, The interaction of magnesium with calcite during crystal growth at 25–90°C and one atmosphere: Geochimica et Cosmochimica Acta, v. 37, p. 1563–1586.

Keul, N., Langer, G., De Nooijer, L.J., Nehrke, G., Reichart, G.J., and Bijma, J., 2013, Incorporation of uranium in benthic foraminiferal calcite reflects seawater carbonate ion concentration: Geochemistry, Geophysics, Geosystems, v. 14, p. 102–111.

Kinsman, D.J., and Holland, H., 1969, The co-precipitation of cations with $CaCO_3$—IV. The co-precipitation of Sr^{2+} with aragonite between 16° and 96°C: Geochimica et Cosmochimica Acta, v. 33, p. 1–17.

Kısakürek, B., Eisenhauer, A., Böhm, F., Garbe-Schönberg, D., and Erez, J., 2008, Controls on shell Mg/Ca and Sr/Ca in cultured planktonic foraminiferan, *Globigerinoides ruber* (white): Earth and Planetary Science Letters, v. 273, p. 260–269.

Kitano, Y., Kanamori, N., and Oomori, T., 1971, Measurements of distribution coefficients of strontium and barium between carbonate precipitate and solution - Abnormally high values of distribution coefficients measured at early stages of carbonate formation: Geochemical Journal, v. 4, p. 183–206.

Kitano, Y., and Oomori, T., 1971, The coprecipitation of uranium with calcium carbonate: Journal of the Oceanographical Society of Japan, v. 27, p. 34–42.

Klinkhammer, G.., and Palmer, M.., 1991, Uranium in the oceans: Where it goes and why: Geochimica et Cosmochimica Acta, v. 55, p. 1799–1806.

Krantz, D.E., Jones, D.S., and Williams, D.F., 1984, Growth rates of the sea scallop, *Placopecten Magellanicus*, determined from the $^{18}O/^{16}O$ record in shell calcite: The Biological Bulletin, v. 167, p. 186–199.

Ku, T.-L., Luo, S., Lowenstein, T.K., Li, J., and Spencer, R.J., 1998, U-series chronology of lacustrine deposits in Death Valley, California: Quaternary Research, v. 50 p. 261–275.

Kulik, D.A., Wagner, T., Dmytrieva, S.V., Kosakowski, G., Hingerl, F.F., Chudnenko, K.V., and Berner, U.R., 2013, GEM-Selektor geochemical modeling package: Revised algorithm and GEMS3K numerical kernel for coupled simulation codes: Computational Geosciences, v. 17, p. 1–24.

Lakshtanov, L.Z., and Stipp, S.L.S., 2007, Experimental study of nickel(II) interaction with calcite: Adsorption and coprecipitation: Geochimica et Cosmochimica Acta, v. 71, p. 3686–3697,.

LaVigne, M., Hill, T.M., Spero, H.J., and Guilderson, T.P., 2011, Bamboo coral Ba/Ca: Calibration of a new deep ocean refractory nutrient proxy: Earth and Planetary Science Letters, v. 312, p. 506–515.

Lea, D.W., and Boyle, E.A., 1991, Barium in planktonic foraminifera: Geochimica et Cosmochimica Acta, v. 55, p. 3321–3331.

Lea, D.W., and Spero, H.J., 1992, Experimental determination of barium uptake in shells of the planktonic foraminifera *Orbulina universa* at 22 °C: Geochimica et Cosmochimica Acta, v. 56, p. 2673–2680.

Lea, D.W., and Spero, H.J., 1994, Assessing the reliability of paleochemical tracers: barium uptake in the shells of planktonic foraminifera: Paleoceanography, v. 9, p. 445–452.

Lea, D.W., Mashiotta, T.A., and Spero, H.J., 1999, Controls on magnesium and strontium uptake in planktonic foraminifera determined by live culturing: Geochimica et Cosmochimica Acta, v. 63, p. 2369–2379.

Lee, K., Kim, T.W., Byrne, R.H., Millero, F.J., Feely, R.A., and Liu, Y.M., 2010, The universal ratio of boron to chlorinity for the North Pacific and North Atlantic oceans: Geochimica et Cosmochimica Acta, v. 74, p. 1801–1811.

Lewis, E., and Wallace, D., 1998, Program developed for CO_2 system calculations: Carbon Dioxide Information Analysis Center, Oak Ridge National Laboratory, U.S. Department of Energy.

Lorens, R.B., 1981, Sr, Cd, Mn and Co distribution coefficients in calcite as a function of calcite precipitation rate: Geochimica et Cosmochimica Acta, v. 45, p. 553–561.

Lowenstein, T.K., Timofeeff, M.N., Brennan, S.T., Hardie, L.A., and Demicco, R.V., 2001, Oscillations in Phanerozoic seawater chemistry: evidence from fluid inclusions: Science (New York, N.Y.), v. 294, p. 1086–1088.

Lowenstein, T.K., Hardie, L.A., Timofeeff, M.N., and Demicco, R.V., 2003, Secular variation in seawater chemistry and the origin and significance of calcium chloride basinal brines, *in* Geological Society of America Annual Meeting, v. 35, p. 201.

Lundberg, J., and Ford, D.C., 1994, Late Pleistocene sea level change in the Bahamas from mass spectrometric U-series dating of submerged speleothem: Quaternary Science Reviews, v. 13, p. 1–14

Mackenzie, F.T., 2003, Carbonate mineralogy and geochemistry *in*: Middleton, G.V., ed., Encyclopedia of sediments and sedimentary rocks, p. 93–100.

Marchitto, T.M.Jr., Curry, W.B., and Oppo, D.W., 2000, Zinc concentrations in benthic foraminifera reflect seawater chemistry: Paleoceanography, v. 15, p. 299–306.

Marchitto, T.M.Jr., Oppo, D.W., and Curry, W.B., 2002, Paired benthic foraminiferal Cd/Ca and Zn/Ca evidence for a greatly increased presence of Southern Ocean water in the glacial North Atlantic: Paleoceanography, v. 17, p. 1–16.

Martin, G.B., Thorrold, S.R., and Jones, C.M., 2004, Temperature and salinity effects on strontium incorporation in otoliths of larval spot (*Leiostomus xanthurus*): Canadian Journal of Fisheries and Aquatic Sciences, v. 61, p. 34–42.

Marriott, C.S., Henderson, G.M., Belshaw, N.S., and Tudhope, A.W., 2004a, Temperature dependence of δ^7Li, δ^{44}Ca and Li/Ca during growth of calcium carbonate: Earth and Planetary Science Letters, v. 222, p. 615–624.

Marriott, C.S., Henderson, G.M., Crompton, R., Staubwasser, M., and Shaw, S., 2004b, Effect of mineralogy, salinity, and temperature on Li/Ca and Li isotope composition of calcium carbonate: Chemical Geology, v. 212, p. 5–15.

Mashiotta, T., Lea, D.W., and Spero, H.J., 1999, Glacial–interglacial changes in Subantarctic sea surface temperature and δ^{18}O-water using foraminiferal Mg: Earth and Planetary Science Letters, v. 170, p. 417–432.

Mathien-Blard, E., and Bassinot, F., 2009, Salinity bias on the foraminifera Mg/Ca thermometry: Correction procedure and implications for past ocean hydrographic reconstructions: Geochemistry, Geophysics, Geosystems, v. 10.

Mavromatis, V., Gautier, Q., Bosc, O., and Schott, J., 2013, Kinetics of Mg partition and Mg stable isotope fractionation during its incorporation in calcite: Geochimica et Cosmochimica Acta, v. 114, p. 188–203.

McManus, J., Berelson, W.M., Hammond, D.E., and Klinkhammer, G.P., 1999, Barium cycling in the North Pacific: Implications for the utility of Ba as a paleoproductivity and paleoalkalinity proxy: Paleoceanography, v. 14, p. 53–61.

Meece, D.E., and Benninger, L.K., 1993, The coprecipitation of Pu and other radionuclides with $CaCO_3$: Geochimica et Cosmochimica Acta, v. 57, p. 1447–1458.

Millero, F.J., 1995, Thermodynamics of the carbon dioxide system in the oceans: Geochimica et Cosmochimica Acta, v. 59, p. 661–677.

Millero, F.J., Graham, T.B., Huang, F., Bustos-Serrano, H., and Pierrot, D., 2006, Dissociation constants of carbonic acid in seawater as a function of salinity and temperature: Marine Chemistry, v. 100, p. 80–94.

Min, G.R., Edwards, R.L., Taylor, F.W., Recy, J., Gallup, C.D., Beck, J.W., 1995. Annual cycles of U/Ca in coral skeletons and U/Ca thermometry: Geochimica et Cosmochimica Acta, v. 59, p. 2025–2042

Montagna, P., McCulloch, M., Douville, E., López Correa, M., Trotter, J., Rodolfo-Metalpa, R., Dissard, D., Ferrier-Pagès, C., Frank, N., Freiwald, A., et al., 2014, Li/Mg systematics in scleractinian corals: Calibration of the thermometer: Geochimica et Cosmochimica Acta, v. 132, p. 288–310.

Montes-Hernandez, G., Renard, F., Geoffroy, N., Charlet, L., and Pironon, J., 2007, Calcite precipitation from CO_2-H_2O-$Ca(OH)_2$ slurry under high pressure of CO_2: Journal of Crystal Growth, v. 308, p. 228–236.

Morse, J.W., Wang, Q., and Tsio, M.Y., 1997, Influences of temperature and Mg:Ca ratio on CaCO3 precipitates from seawater: Geology, v. 25, p. 85–87.

Morse, J.W., Arvidson, R.S., and Lüttge, A., 2007, Calcium carbonate formation and dissolution: Chemical Reviews, v. 107, p. 342–381.

Mucci, A., 1983, The solubility of calcite and aragonite in seawater at various salinities, temperatures, and one atmosphere total pressure.: American Journal of Science, v. 283, p. 780–799.

Mucci, A., 1987, Influence of temperature on the composition of magnesian calcite overgrowths precipitated from seawater: Geochimica et Cosmochimica Acta, v. 51, p. 1977–1984.

Mucci, A., and Morse, J.W., 1983, The incorporation of Mg^{2+} and Sr^{2+} into calcite overgrowths: influences of growth rate and solution composition: Geochimica et Cosmochimica Acta, v. 47, p. 217–233.

Munemoto, T., and Fukushi, K., 2008, Transformation kinetics of monohydrocalcite to aragonite in aqueous solutions: Journal of Mineralogical and Petrological Sciences, v. 103, p. 345–349.

Nürnberg, D., Bijma, J., and Hemleben, C., 1996, Assessing the reliability of magnesium in foraminiferal calcite as a proxy for water mass temperatures: Geochimica et Cosmochimica Acta, v. 60, p. 803–814.

Oomori, T., Kaneshima, H., Maezato, Y., and Kitano, Y., 1987, Distribution coefficient of Mg^{2+} ions between calcite and solution at 10–50 °C: Marine Chemistry, v. 20, p. 327–336.

Owen, R., Kennedy, H., and Richardson, C., 2002, Isotopic partitioning between scallop calcite and seawater: Effect of shell growth rate: Geochimica et Cosmochimica Acta, v. 66, p. 1727–1737.

Paquette, J., and Reeder, R.J., 1995, Relationship between surface structure, growth mechanism, and trace element incorporation in calcite: Geochimica et Cosmochimica Acta, v. 59, p. 735–749.

Pierrot, D., Lewis E., and Wallace, D., 2006, MS Excel Program Developed for CO_2 System Calculations, Carbon Dioxide Information Analysis Center, Oak Ridge National Laboratory, U.S. Department of Energy.

Plant, L.J., and House, W.A., 2002, Precipitation of calcite in the presence of inorganic phosphate: Colloids and Surfaces A: Physicochemical and Engineering Aspects, v. 203, p. 143–153.

Poulain, C., Gillikin, D.P., Thébault, J., Munaron, J.M., Bohn, M., Robert, R., Paulet, Y.M., and Lorrain, A., 2015, An evaluation of Mg/Ca, Sr/Ca, and Ba/Ca ratios as environmental proxies in aragonite bivalve shells: Chemical Geology, v. 396, p. 42–50.

Prentice, K., Dunkley Jones, T., Lees, J. a, Young, J., Bown, P., Langer, G., Fearn, S., and EIMF, 2014, Trace metal (Mg/Ca and Sr/Ca) analyses of single coccoliths by Secondary Ion Mass Spectrometry: Geochimica et Cosmochimica Acta, v. 146, p. 90–106.

Pytkowicz, R.M., 1965, Rates of Inorganic Calcium Carbonate Nucleation: The Journal of Geology, v. 73, p. 196–199.

Raitzsch, M., Kuhnert, H., Hathorne, E.C., Groeneveld, J., and Bickert, T., 2011, U/Ca in benthic foraminifers: A proxy for the deep-sea carbonate saturation: Geochemistry, Geophysics, Geosystems, v. 12.

Reeder, R.J., Nugent, M., Tait, C.D., Morris, D.E., Heald, S.M., Beck, K.M., Hess, W.P., and Lanzirotti, A., 2001, Coprecipitation of uranium(VI) with calcite: XAFS, micro-XAS, and luminescence characterization: Geochimica et Cosmochimica Acta, v. 65, p. 3491–3503.

Ries, J.B., 2004, Effect of ambient Mg/Ca ratio on Mg fractionation in calcareous marine invertebrates: A record of the oceanic Mg/Ca ratio over the Phanerozoic: Geology, v. 32, p. 981–984.

Rodriguez-Blanco, J.D., Shaw, S., Bots, P., Roncal-Herrero, T., and Benning, L.G., 2014, The role of Mg in the crystallization of monohydrocalcite: Geochimica et Cosmochimica Acta, v. 127, p. 204–220.

Rosenthal, Y., Boyle, E. a., and Slowey, N., 1997, Temperature control on the incorporation of magnesium, strontium, fluorine, and cadmium into benthic foraminiferal shells from Little Bahama Bank: Prospects for thermocline paleoceanography: Geochimica et Cosmochimica Acta, v. 61, p. 3633–3643.

Rounds, S.A., 2012. Alkalinity and Acid Neutralizing Capacity (ver. 4.0): U.S. Geological Survey Techniques of Water-Resources Investigations (Book 9, Chapter A6, section 6.6). <http://water.usgs.gov/owq/FieldManual/Chapter6/section6.6/>

Rubin, S.I., King, S.L., Jahnke, R.A., Froelich, N., 2003, Benthic barium and alkalinity fluxes: Is Ba an oceanic paleo-alkalinity proxy for glacial atmospheric CO^2?: Geophysical Research Letters, v. 30.

Russell, A.D., Emerson, S., Nelson, B.K., Erez, J., and Lea, D.W., 1994, Uranium in foraminiferal calcite as a recorder of seawater uranium concentrations: Geochimica et Cosmochimica Acta, v. 58, p. 671–681.

Russell, A.D., Hönisch, B., Spero, H.J., and Lea, D.W., 2004, Effects of seawater carbonate ion concentration and temperature on shell U, Mg, and Sr in cultured planktonic foraminifera: Geochimica et Cosmochimica Acta, v. 68, p. 4347–4361.

Sandberg, P.A., 1983, An oscillating trend in Phanerozoic non-skeletal carbonate mineralogy: Nature, v. 305, p. 19–22.

Sano, Y., Shirai, K., Takahata, N., Hirata, T., and Sturchio, N.C., 2005, Nano-SIMS analysis of Mg, Sr, Ba and U in natural calcium carbonate: Analytical Sciences: The International Journal of the Japan Society for Analytical Chemistry, v. 21, p. 1091–1097.

Saulnier, S., Rollion-Bard, C., Vigier, N., and Chaussidon, M., 2012, Mg isotope fractionation during calcite precipitation: An experimental study: Geochimica et Cosmochimica Acta, v. 91, p. 75–91.

Schmidt, D.N., Lazarus, D., Young, J.R., and Kucera, M., 2006, Biogeography and evolution of body size in marine plankton: Earth-Science Reviews, v. 78, p. 239–266.

Shen, C.C., Hastings, D.W., Lee, T., Chiu, C.H., Lee, M.Y., Wei, K.Y., and Edwards, R.L., 2001, High precision glacial-interglacial benthic foraminiferal Sr/Ca records from the eastern equatorial Atlantic Ocean and Caribbean Sea: Earth and Planetary Science Letters, v. 190, p. 197–209.

Shen, G.T., and Dunbar, R.B., 1995, Environmental controls on uranium in reef corals: Geochimica et Cosmochimica Acta, v. 59, p. 2009–2024.

Shimizu, N., Semet, M.P., and Allègre, C.J., 1978, Geochemical applications of quantitative ion-microprobe analysis: Geochimica et Cosmochimica Acta, v. 42, p. 1321–1334.

Spencer, R.J., and Hardie, L.A., 1990, Control of seawater composition by mixing of river waters and mid-ocean ridge hydrothermal brines: Fluid-mineral interactions: A tribute to HP Eugster: Geochemical Society Special Publication, v. 19, p. 409–419.

Spötl, C., Unterwurzacher, M., Mangini, a, and Longstaffe, F.J., 2002, Carbonate speleothems in the dry, Inneralpine Vinschgau Valley, northernmost Italy: Witnesses of changes in climate and hydrology since the Late Glacial Maximum: Journal of Sedimentary Research, v. 72, p. 793–808.

Stanley, S.M., and Hardie, L. A., 1999, Hypercalcification: Paleontology links plate tectonics and geochemistry to sedimentology: GSA Today, v. 9, p. 1–7.

Stanley, S.M., Ries, J.B., and Hardie, L.A., 2005, Seawater chemistry, coccolithophore population growth, and the origin of Cretaceous chalk: Geology, v. 33, p. 593–596.

Stoll, H.M., Rosenthal, Y., and Falkowski, P., 2002, Climate proxies from Sr/Ca of coccolith calcite: Calibrations from continuous culture of *Emiliania huxleyi*: Geochimica et Cosmochimica Acta, v. 66, p. 927–936.

Stoll, H.M., Ziveri, P., Shimizu, N., Conte, M., and Theroux, S., 2007, Relationship between coccolith Sr/Ca ratios and coccolithophore production and export in the Arabian Sea and Sargasso Sea: Deep-Sea Research Part II: Topical Studies in Oceanography, v. 54, p. 581–600.

Sturchio, N.C., Antonio, M.R., Soderholm, L., Sutton, S.R., and Brannon, J.C., 1998, Tetravalent uranium in calcite: Science, v. 281, p. 971–973.

Tang, J., Köhler, S.J., and Dietzel, M., 2008a, Sr^{2+}/Ca^{2+} and $^{44}Ca/^{40}Ca$ fractionation during inorganic calcite formation: I. Sr incorporation: Geochimica et Cosmochimica Acta, v. 72, p. 3718–3732.

Tang, J., Dietzel, M., Bohm, F., Köhler, S.J., and Eisenhauer, A., 2008b, Sr^{2+}/Ca^{2+} and $^{44}Ca/^{40}Ca$ fractionation during inorganic calcite formation: II. Ca isotopes. Geochimica et Cosmochimica Acta, v. 72, p. 3733–3745.

Ter Kuile, B., and Erez, J., 1984, In situ growth-rate experiments on the symbiont bearing foraminifera *Amphistegina lobifera* and *Amphistegina hemprichii*: Journal of Foraminiferal Research, v. 14, p. 262–276.

Tesoriero, A.J., and Pankow, J.F., 1996, Solid solution partitioning of Sr^{2+}, Ba^{2+}, and Cd^{2+} to calcite: Geochimica et Cosmochimica Acta, v. 60, p. 1053–1063.

Thien, B.M.J., Kulik, D.A., and Curti, E., 2014, A unified approach to model uptake kinetics of trace elements in complex aqueous – solid solution systems: Applied Geochemistry, v. 41, p. 135–150.

Tucker, M.E., and Wright, V.P., 1990, Carbonate Sedimentology. Oxford: Blackwell Scientific Publications, 482 p.

Turley, C.M., Gooday, A.J., and Green, J.C., 1993, Maintenance of abyssal benthic foraminifera under high pressure and low temperature: some preliminary results: Deep-Sea Research, v. 40, p. 643–652.

Valle-Fuentes, F.J., Garcia-Guinea, J., Cremades, A., Correcher, V., Sanchez-Moral, S., Gonzalez-Martin, R., Sanchez-Muñoz, L., and Lopez-Arce, P., 2007, Low-magnesium uranium-calcite with high degree of crystallinity and gigantic luminescence emission: Applied Radiation and Isotopes, v. 65, p. 147–154.

Watson, E.B., and Yan Liang, 1995, A simple model for sector zoning in slowly grown crystals: implications for growth rate and lattice diffusion, with emphasis on accessory minerals in crustal rocks: American Mineralogist, v. 80, p. 1179–1187.

Watson, E.B., 1996, Surface enrichment and trace-element uptake during crystal growth: Geochimica et Cosmochimica Acta, v. 60, p. 5013–5020.

Watson, E.B., 2004, A conceptual model for near-surface kinetic controls on the trace-element and stable isotope composition of abiogenic calcite crystals: Geochimica et Cosmochimica Acta, v. 68, p. 1473–1488.

Weber, J.N., 1973, Incorporation of strontium into reef coral skeletal carbonates: Geochim. et Cosmochim. Acta, v. 37, p. 2173–2190.

Wilkinson, B.H., and Algeo, T.J., 1989, Sedimentary carbonate record of calcium-magnesium cycling: American Journal of Science, v. 289, p. 1158–1194.

Winograd, I.J., Landwehr, J.M., Coplen, T.B., Sharp, W.D., Riggs, A.C., Ludwig, K.R., and Kolesar, P.T., 2006, Devils Hole, Nevada, $\delta^{18}O$ record extended to the mid-Holocene: Quaternary Research, v. 66, p. 202–212.

Wolthers, M., Nehrke, G., Gustafsson, J.P., and Van Cappellen, P., 2012, Calcite growth kinetics: Modeling the effect of solution stoichiometry. Geochimica et Cosmochimica Acta, v. 77, p.121–134.

Zeebe, R.E., 2011, Marine carbonate chemistry. *In*: The Encyclopedia of Earth, ed. J.P. Gattuso

Zeebe, R.E., Wolf-Gladrow, D.A., 2001, CO_2 in seawater: equilibrium, kinetics, isotopes., v. 65, Elsevier, 346 p.

Zhong, S., and Mucci, A., 1989, Calcite and aragonite precipitation from seawater solutions of various salinities: Precipitation rates and overgrowth compositions: Chemical Geology, v. 78, p. 283–299.

Zimmermann, H., Holland, H.D., and Horita, J.A.B., 2000, The evolution of seawater during the Phanerozoic; record from marine evaporites and fluid inclusions in halite, *in* Geological Society of America Annual Meeting, v. 32, p. 67.